Modeling Callisto's Ionosphere, Airglow and Magnetic Field Environment

Inaugural-Dissertation

zur

Erlangung des Doktorgrades

der Mathematisch-Naturwissenschaftlichen Fakultät

der Universität zu Köln

vorgelegt von

Oliver Hartkorn

aus Dernbach

Köln 2017

Berichterstatter/in: Prof. Dr. Joachim Saur

Prof. Dr. Bülent Tezkan

Tag der mündlichen Prüfung: Montag, 26. Juni 2017

Abstract

Previous observations of the Galileo spacecraft and the Hubble Space Telescope indicate that Callisto possesses a neutral atmosphere which is mostly composed of O_2 and additionally contains H_2O and CO_2. The first aim of our study is to constrain density and structure of the atmospheric O_2. Based on existent observations and findings, we construct a phenomenological model of Callisto's atmosphere. Then, we use this atmosphere model as input information for an ionosphere model, which is based on physical principles and has been developed by us specifically for Callisto. Using this coupled description of Callisto's atmosphere-ionosphere system, we calculate the spatial distribution of ionospheric electron densities and the atmospheric ultraviolet emission, i.e., airglow. By varying the prescribed O_2 atmosphere and comparing calculated electron densities with Galileo radio occultation measurements and calculated UV emission intensities with Hubble Space Telescope observations, we are able to constrain density and structure of Callisto's O_2 atmosphere. We find an average O_2 column density of $2.1^{+1.1}_{-1.1} \times 10^{19}$ m^{-2} and a likely day-night asymmetry of the O_2 atmosphere. In the framework of our ionosphere model we calculate the electron energy distribution function at each point in the ionosphere by solving a coupled set of equations consisting of the Boltzmann equation for suprathermal electrons and the continuity and energy equation for thermal electrons. Since we can neglect electron transport for our purposes, we assume a stationary balance between local sources and sinks of electrons and electron energy. Photoionization is expected to be the major source of ionospheric electrons at Callisto. Therefore, our model includes photoionization and secondary ionization processes from collisions of photoelectrons with neutrals. Using our ionosphere model, we also investigate the formation process of Callisto's O_2 atmosphere. Atmospheric O_2 is most likely generated by surface sputtering and sublimation. Assuming that surface sputtering is the main source and causes an orbital phase dependent atmospheric O_2 density, we predict atmospheric UV emission intensities for different orbital phases of Callisto. These predictions can be used by other scientists to interpret telescope observations of Callisto regarding the question about the origin of Callisto's atmosphere. Further, we wonder whether electromagnetic induction within Callisto's ionosphere can explain observed magnetic field disturbances that have been interpreted as evidence for a subsurface ocean. The rotation of Jupiter's magnetic field causes a periodically time varying magnetic field in the rest frame of Callisto, which induces currents within Callisto's ionosphere. We derive the conductivity structure of Callisto's ionosphere from our ionosphere model and simulate this induction process. From analytic considerations, we expect a

nearly perfect Cowling channel in Callisto's ionosphere and, hence, only a weak continuation of ionospheric currents in the surrounding magnetospheric plasma. Based on these findings, we construct a detailed numerical model to calculate the induced currents and according secondary magnetic fields quantitatively. We compare our results with the magnetic field measurements from the Galileo flybys C-3 and C-9, during which magnetic field disturbances have been observed that are diagnostic for induction in a conductive spherical shell. Our model results show that induction within Callisto's ionosphere is an important and non-negligible process that is responsible for a major part of the observed magnetic field disturbances. Due to the present model-uncertainties regarding Callisto's ionosphere, we can not rule out the existence of an conductive subsurface layer like a subsurface ocean. However, if properties of such a subsurface layer are derived from future observations, for example, observations of the JUpiter ICy moon Explorer (JUICE) spacecraft, a consideration of induction in the ionosphere is mandatory.

Zusammenfassung

Beobachtungen der Galileo-Raumsonde und des Hubble-Weltraumteleskops weisen darauf hin, dass Callisto eine Neutralgas-Atmosphäre besitzt, die sich hauptsächlich aus O_2 und zu geringeren Anteilen aus H_2O und CO_2 zusammensetzt. Das erste Ziel unserer Arbeit besteht darin, die Dichte und die Struktur der O_2-Atmosphäre Callistos zu bestimmen. Auf der Basis existierenden Beobachtungen und Erkenntnisse konstruieren wir zunächst ein phänomenologisches Modell der Callisto-Atmosphäre. Dieses Atmosphärenmodell wird als Eingangsinformation für ein physikalisch motiviertes Ionosphärenmodell verwendet, welches wir speziell für Callisto entwickeln. Mithilfe dieser gekoppelten Beschreibung von Callistos Atmosphäre und Ionosphäre berechnen wir die räumliche Verteilung der ionosphärischen Elektronendichten und der atmosphärischen Emission im UV-Bereich. Durch die Variation der angenommenen O_2-Atmosphäre und den Vergleich von berechneten Elektronendichten mit Radio-Okkultations-Beobachtungen und von berechneten UV-Emissionen mit Hubble-Weltraumteleskop-Beobachtungen können wir die Dichte und Struktur von Callistos O_2-Atmosphäre bestimmen. Wir finden eine durchschnittliche O_2-Säulendichte von $2.1^{+1.1}_{-1.1} \times 10^{19}$ m^{-2} und eine wahrscheinliche Tag-Nacht-Asymmetrie der O_2-Atmosphäre. Im Rahmen unseres Ionosphärenmodells berechnen wir die Elektronen-Energie-Verteilungsfunktion an jedem Punkt der Ionosphäre, indem wir einen gekoppelten Satz von Gleichungen lösen, der aus der Boltzmann-Gleichung für suprathermale Elektronen und der Kontinuitäts- und Energiegleichung für thermische Elektronen besteht. Da wir den Elektronentransport im Rahmen unserer Fragestellungen vernachlässigen können, nehmen wir an, dass ein stationäres Gleichgewicht zwischen lokalen Quellen und Senken von Elektronen und Elektronenenergie besteht. Die Photoionisation stellt bei Callisto die Hauptquelle der ionosphärischen Elektronen dar. Unser Modell beinhaltet deshalb Photoionisation und sekundäre Ionisationsprozesse, die durch Kollisionen von Photoelektronen mit Neutralteilchen entstehen. Basierend auf unserem Ionosphärenmodell, stellen wir die Frage nach der Hauptquelle von Callistos O_2-Atmosphäre. Wahrscheinlich wird atmosphärisches O_2 hauptsächlich durch Sublimation oder durch Oberflächen-Sputtering erzeugt. Unter der Annahme dass das Oberflächen-Sputtering die dominierende Quelle darstellt und eine atmosphärische O_2-Dichte verursacht, die von der orbitalen Phase abhängt, sagen wir die Intensitäten der atmosphärischen UV Emission für unterschiedliche orbitale Phasen voraus. Des Weiteren stellt sich die Frage, ob die elektromagnetische Induktion innerhalb der Ionosphäre von Callisto beobachtete Magnetfeldmessungen erklären kann, die als Beweis für einen unterirdischen Ozean interpretiert wurden. Die Rotation des Jupiter-Magnetfeldes bewirkt ein periodisch zeitlich

variables Magnetfeld im Ruhesystem von Callisto, welches Ströme innerhalb der beobachteten Ionosphäre von Callisto induziert. Wir leiten auf der Basis unseres Ionosphärenmodells die Leitfähigkeitsstruktur der Callisto-Ionosphäre ab und simulieren diesen Induktionsprozess. Aufgrund analytischer Berechnungen erwarten wir in der Ionosphäre von Callisto einen nahezu perfekten Cowling-Kanal und damit nur eine schwache Fortsetzung der ionosphärischen Ströme im umgebenden magnetosphärischen Plasma. Auf dieser Erkenntnis beruhend konstruieren wir ein detaillierteres numerisches Modell, um die induzierten Ströme und die entsprechenden Sekundärmagnetfelder quantitativ zu berechnen. Wir vergleichen unsere Resultate mit den Magnetfeldmessungen der Galileo-Vorbeiflüge C-3 und C-9, bei denen Magnetfeldstörungen beobachtet wurden, die diagnostisch für den Induktionsprozess in einer leitfähigen sphärischen Schale sind. Unsere Ergebnisse zeigen, dass die Induktion innerhalb der Ionosphäre von Callisto einen wichtigen und nicht-vernachlässigbaren Prozess darstellt, der zu einem großen Teil für die beobachteten Magnetfeldstörungen verantwortlich ist. Aufgrund der momentanen Modellunsicherheiten bezüglich der Ionosphäre von Callisto, können wir nicht ausschließen, dass eine leitfähige Schicht im Untergrund existiert. Wenn jedoch Eigenschaften einer solchen potentiellen Schicht auf der Basis zukünftiger Messungen, wie z.B. Messungen der JUpiter ICy moon Explorer (JUICE) Raumsonde, abgeleitet werden, ist eine Berücksichtigung der Induktion in der Ionosphäre zwingend erforderlich.

Contents

1 Introduction

In the history of mankind, human beings have always tried to discover and understand new unknown worlds driven by natural curiosity. When we leave Earth and look into space, countless unknown terrains lie ahead of us. In particular a group of very fascinating extraterrestrial bodies are located about 7.5 million kilometres apart from our home planet: These worlds are the moons Io, Europa, Ganymede and Callisto, which orbit around the gas giant Jupiter. They are called 'Galilean moons' in honor of Galileo Galilei, who discovered these moons in 1610. The moons' names refer to the Roman and Greek mythology, where the god Jupiter had love affairs with the priestess Io, the princess Europa, the nymph Callisto and kidnapped the hero Ganymede to make him his cup bearer.

The Galilean moons have been within the scope of past and future space missions. Pioneer 10 and 11 visited them in 1973 and 1974 followed by Voyager 1 and 2 in 1979. Later, between 1995 and 2001, the Galileo spacecraft explored these moons more intensively. An in-depth characterization of the Galilean moons is the next logical step of investigation. For this purpose, the JUICE (JUpiter ICy moon Explorer) spacecraft is going to be launched in 2022, scheduled to arrive at the Jovian system in 2030. A major scientific objective of JUICE is the characterization of the outer Galilean moons Ganymede and Callisto. Additionally to spacecraft observations, the Hubble Space Telescope (HST) has been used to remotely investigate the Galilean moons since its start of operation in 1990 (e.g., Strobel et al., 2002; Cunningham et al., 2015; Roth et al., 2017).

Each Galilean moon possesses unique features. Io is the innermost moon orbiting Jupiter at a distance of 5.9 Jupiter radii. It experiences large tidal forces causing a strong geological and volcanic activity. Its surface is primarily composed of silicate rock and it is the most active volcanic known body of the solar system. There is an ongoing debate whether Io has a global subsurface magma ocean (e.g. Khurana et al., 2011; Roth et al., 2017). A bit farther out, Europa orbits Jupiter at a distance of 9.4 Jupiter radii. Europa belongs to Jupiter's icy moons and so do Ganymede and Callisto. The surfaces of these moons are predominately covered by water ice. In agreement with geological models, Galileo magnetic field measurements showed that there is a subsurface saline water ocean below Europa's

icy crust (Khurana et al., 1998). Also water vapor plumes seems to exist at Europa, they were discovered by Roth et al. (2014). At the moment, the search for these plumes is in the focus of observational studies and the National Aeronautics and Space Administration (NASA) is planning a dedicated Europa mission in order to investigate this phenomenon. As the next one in the row, Ganymede orbits Jupiter at a distance of 15 Jupiter radii. This moon is larger than the planet Mercury and possesses its own intrinsic magnetic dynamo field (Kivelson et al., 1997). Ultraviolet aurora is occurring at Ganymede probably as a result of interactions between electrons accelerated along open-closed magnetic field lines and a thin atmosphere. According to models of Ganymede's magnetic field environment, observations of the aurora support the hypothesis that Ganymede also possesses a subsurface water ocean (Saur et al., 2015). In contrast to the very clean surface ice of Europa, the surfaces of Ganymede and also Callisto contain larger portions of regolith. Callisto is the outermost Galilean moon and the least understood one. There are also indication for a subsurface water ocean at Callisto from Galileo magnetic field measurements (Khurana et al., 1998). However, the existence of this ocean is less certain than in case of Europa due to inconsistencies with geological models (e.g., Cassen, 1980). Further, neither the composition and density of Callisto's atmosphere nor the source of this atmosphere is well understood so far.

Since subsurface oceans are expected to exist at Europa, Ganymede and Callisto, these Galilean moons are seen as potential hosts of extraterrestrial life. An understanding of these moons, especially their interior structure and their atmospheres is, therefore, an essential contribution to the search for life outside Earth. In this respect, the overall aim of this dissertation is to better understand the weakly understood moon Callisto on the basis of models that can explain existing observations. Moreover, we discuss new questions that might be answered by future space missions or telescope observations.

The first objective of our study is to characterize Callisto's atmosphere-ionosphere system on the basis of existent Galileo and HST observations. For this purpose, we develop a fluid-kinetic model of Callisto's ionosphere which allows us to constrain density and structure of Callisto's atmosphere by comparing model predictions of electron densities and airglow with Galileo radio science measurements and HST observations. The second objective is to determine the major source of

Callisto's atmosphere. On the basis of our ionosphere model we predict HST observations for different observational geometries under the assumption of a surface sputtering dominated atmosphere generation. In this way, we generate a test of the hypothesis that surface sputtering is the dominant source of Callisto's atmosphere. The third objective is to answer the question whether a subsurface ocean at Callisto is the unique explanation for induction signatures seen in magnetic field measurements of the Galileo spacecraft. In the past, several authors have interpreted these signatures as evidence for such an ocean (e.g., Khurana et al., 1998). Since a conductive ionosphere can cause induction signatures, too, we answer the question how our findings about Callisto's ionosphere change the interpretation of Callisto's magnetic field environment.

This monograph is structured as follows: In Chapter 2 and Chapter 3, we present the current state of knowledge about Callisto and its plasma environment on the basis of previous observational and modeling studies. In Chapter 4, we present the basics of planetary ionosphere modeling before we explain our newly developed atmosphere-ionosphere model for Callisto in Chapter 5 and Chapter 6. One application of this model is the prediction of HST observations, which we present in Chapter 7. Another application is the determination of the expected induction signatures from Callisto's ionosphere, which is subject of Chapter 8. Finally, we provide a summary and the most important conclusions in Chapter 9.

Note that Chapters 5, Chapter 6 and parts of Chapter 3 have been published in Hartkorn et al. (2017). Moreover, Chapter 8 is published in Hartkorn and Saur (2017). In the course of this dissertation some paragraphs of these publications have been revised and extended. The conclusions in Chapter 9 also contains parts of Hartkorn et al. (2017) and Hartkorn and Saur (2017). Further, note that Section 8.1, especially Sections 8.1.2 and 8.1.4, are mainly based on the work of Joachim Saur, who is the co-author of Hartkorn and Saur (2017). His work is presented since it is highly relevant for the understanding of the work that is presented subsequently.

2 Callisto's environment

Callisto is the second largest Galilean moon with a radius of 2410 km. It orbits Jupiter on a nearly circular orbit with an orbital period of ∼16.7 days and a mean orbit radius of 26.3 Jupiter radii (radius of Jupiter $R_J = 71492$ km). The rotation of Callisto and the other Galilean moons is synchronized with their orbital rotation making them all face centered orbital objects. In Table 2.1, the basic orbital parameters of Callisto are compared with those of Io, Europa and Ganymede showing the outstanding orbital position of Callisto.

Callisto's orbit is located inside the Jovian magnetosphere, which forms Callisto's magnetic field environment and plasma environment. A review of the current understanding of this environment is, therefore, helpful to better understand physical processes occurring at Callisto. In the following, we discuss the general structure of the Jovian magnetosphere (Section 2.1) and the magnetospheric properties that have been observed or been expected at Callisto's orbit (Section 2.2). If no specific reference is given, the information about the Jovian magnetosphere presented in Section 2.1 are taken from Khurana et al. (2004).

	Io	Europa	Ganymede	Callisto
Radius [km]	3643	1561	2634	2410
Mean orbit radius [R_J]	5.9	9.4	15.0	26.3
Orbital period [d]	1.8	3.6	7.2	16.7

Table 2.1: Basic orbital parameters of the four Galilean moons.

2.1 The Jovian magnetosphere

The Jovian magnetosphere is created by Jupiter's dynamo magnetic field, which possesses a dominant magnetic dipole moment that is tilted by ∼10 degrees with respect to Jupiter's rotational axis and the norm vector of Callisto's orbital plane. Figure 2.1 shows a sketch of Jupiter's magnetosphere, where the tilt is visible between the vector of magnetic moment $\underline{M}$ and the pseudovector of angular velocity $\underline{\Omega}$. The equatorial surface field strength of Jupiter's magnetic field is about 428 000 nT, which is approximately 14 times larger than the corresponding

field strength of Earth's magnetic field. As the interaction with the solar wind is super-magnetosonic, the Jovian magnetosphere possesses a bow shock and a magnetopause comparable to the structures usually seen at Earth. The stand-off distance of the magnetopause is between 45 and 100 R_J, basically depending on the solar wind dynamic pressure. The cavity of the magnetosphere is filled with plasma. In contrast to Earth's convection driven magnetospheric plasma, Jupiter's magnetospheric plasma is rotationally driven meaning that the bulk of magnetsopheric energy is derived from Jupiter's rotation. Compared with the orbital period of Callisto of 16.7 days, Jupiter's magnetic field rotates relatively fast with a period of about 10 hours.

The main source of Jupiter's magnetospheric plasma is embedded within the magnetosphere: Io is orbiting Jupiter at a distance of $\sim$5.9 R_J and is emitting neutral gas, mainly sulfur dioxid (SO_2), due to its volcanism. The mass loss rate of Io's atmosphere is expected to be about one ton per second (e.g., Saur et al., 2004). Eventually, emitted gas particles are ionized mainly by electron impact ionization and charge exchange. As the relatively fast rotating magnetic field and the magnetospheric plasma overtake Io on its orbit, newly ionized particles experience an electric field created by the relatively moving magnetic
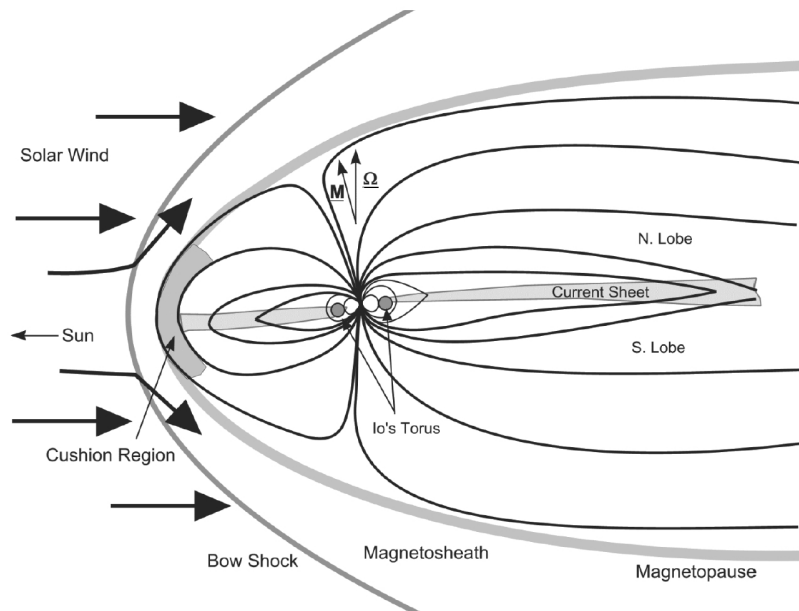

Figure 2.1: Jupiter's magnetosphere structure showing the moon-midnight meridian, taken from Khurana et al. (2004).

field, are accelerated and picked up by the magnetopsheric plasma. The main magnetospheric ion species originating from Io are various charge states of atomic sulfur (S) and atomic oxygen (O). Io's particle emission maintains the so-called Io plasma torus, which is a region of enhanced plasma density concentrated around Jupiter's magnetic dipole equator at the orbital distance of Io. Less significant plasma sources of Jupiter's magnetosphere are expected to be plasma injections from the solar wind and ions which escape from Jupiter's ionosphere (Hill et al., 1983). These sources contribute basically oxygen ions (H^+) and helium ions (He^+) to the magnetospheric plasma.

Up to a distance of 10 R_J, the magnetospheric plasma nearly co-rotates with Jupiter's magnetic field as expected from the frozen-in-field theorem. This region is called the inner magnetosphere. Due to the mass loading of the magnetospheric plasma and collisions between the plasma and the atmospheric neutrals at Io's orbit, the plasma flow is slowed down as a consequence of the conversation of angular momentum and plasma slowly diffuses outwards due to centrifugal forces. Therefore, the co-rotation gradually breaks down within the middle magnetosphere, which ranges from 10 to 40 R_J, to roughly 50% co-rotation in the outer magnetosphere beyond 40 R_J.

Since the magnetospheric frozen-in field is tied to the radial outward diffusing plasma, Jupiter's magnetic field is stretched outwards within the plane of the magnetic equator as visible in Figure 2.1. As a result of the balance between centrifugal, thermal and Lorentz forces, a current sheet (and plasma sheet) forms within a thin region where the polarity of Jupiter's magnetic field switches. This current sheet possesses a thickness of about 2 R_J and is a region of enhanced plasma density. The regions above and below the current sheet are called northern and southern lobe respectively (see Figure 2.1).

2.2 Properties of the Jovian magnetosphere at Callisto's orbit

In order to describe Callisto's magnetic field environment more precisely, we introduce the Callisto centered coordinate system, the so-called CPhiO coordinate system (x',y',z') (see Figure 2.2). The x'-axis points towards the direction of Callisto's orbital velocity, the y'-axis points towards Jupiter and the z'-axis
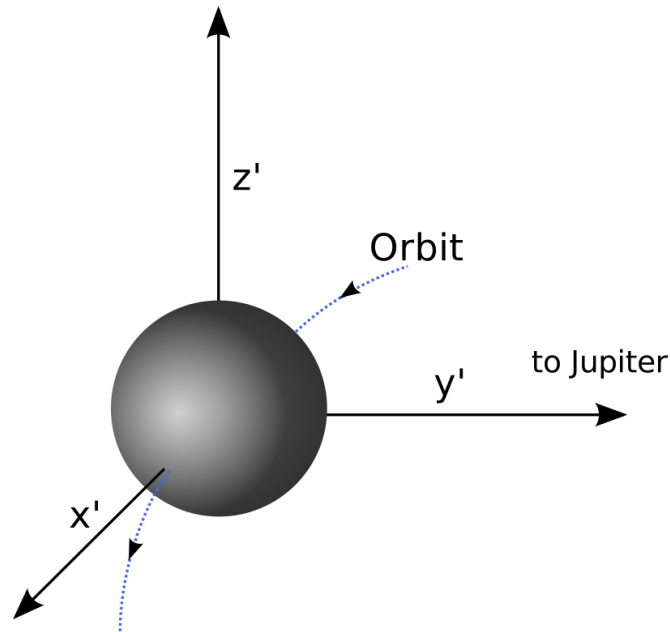
Figure 2.2: Illustration of the CPhiO coordinate system.

completes a right handed orthonormal coordinate system.

In contrast to the closer orbits of the other Galilean moons, Callisto's orbit is located inside the center of Jupiter's middle magnetosphere. Due to the radial outward directed stretching of Jupiter's magnetic field in this region (described in Section 2.1), the radial vector component, seen from a Jupiter centered coordinate system, is the dominant magnetic field component at Callisto's position. In the CPhiO system, this vector component corresponds to the y'-component. Measurements of the Galileo spacecraft have shown that at Callisto, the total magnetic field strength varies between $\sim$4 nT when Callisto is located inside the current sheet and $\sim$42 nT when Callisto is located at its maximum distance from the current sheet in the northern or southern lobe of Jupiter's magnetosphere (Kivelson et al., 2004).

Callisto is exposed to a time-variable magnetic field caused by the rotation of Jupiter's magnetic field. Due to the tilt of Jupiter's magnetic dipole moment with respect to Jupiter's rotation axis, Jupiter's magnetic equator and the current sheet periodically cross over Callisto. As a consequence, Callisto experiences a periodically varying background magnetic field with amplitudes of $\sim$40 nT in the y'-component, $\sim$6 nT in the x'-component and $\sim$3 nT in the z'-component. (e.g., Kivelson et al., 1999; Seufert et al., 2011). The constant background magnetic

field has only a z'-component on the order of -6.5 nT (Kivelson et al., 1999, figure 1b).

Additionally, Callisto is exposed to a magnetospheric plasma flow, which is also caused by the rotation of Jupiter's magnetic field. As this rotation is faster than Callisto's orbital rotation, the frozen-in magnetospheric plasma continuously overtakes Callisto. The upstream conditions might deviate from pure co-rotation with Jupiter since Callisto's orbit is located in the center of the middle magnetosphere, where the plasma does not fully co-rotate anymore. In comparison to the other Galilean moons, the upstreaming plasma is more variable at Callisto's position. In the rest frame of Callisto, the upstream plasma velocity is about 192 km s^{-1} with an observed range of 122-272 km s^{-1} and the ion number density of the magnetospheric plasma is in the range of $0.01 - 0.5 \times 10^6$ m^{-3} with an average value of about 0.1×10^6 m^{-3} (Kivelson et al., 2004).

3 Former studies on Callisto

Much knowledge about the Jupiter system and the Galilean moons has been gained due to the Galileo spacecraft, which was launched on October 18, 1989, arrived at the Jovian system on December 7, 1995 and operated on an orbit around Jupiter until September 21, 2003. In addition, the HST has been used many times to investigate the Galilean moons. It was launched into an Earth orbit in 1990 and is still operating at the time of writing. In the following, we present observational and modeling studies regarding Callisto's atmosphere-ionosphere system and magnetic field environment, which are mainly based on Galileo and HST observations.

3.1 Studies based on Galileo spacecraft observations

Between 1995 and 2003, the Galileo spacecraft performed eight Callisto flybys conducting several in-situ and remote sensing measurements. Among these measurements, magnetic field measurements by the magnetometer (MAG) and radio occultation measurements are the most relevant ones regarding our study of Callisto's atmosphere-ionosphere system. For all flybys, Table 3.1 displays which ones of these measurements have been performed and lists geometric parameters that are necessary for later data interpretations. Moreover, other Galileo instruments, namely, the Solid State Imager (SSI), the Near-Infrared Mapping Spectrograph (NIMS) and the Plasma Wave Instrument (PWS) delivered important contributions to the current understanding of Callisto.

3.1.1 Atmospheric CO_2 abundance from near-infrared mapping spectroscopy

During flyby C-10, the NIMS instrument detected limb emission from the 4.26 μm $\nu3$ fundamental stretching band of carbon dioxide (CO_2) up to $\sim$100 km above the surface and approximately at the equator and noon of Callisto. From this

Date	96/11/04	97/06/25	97/09/17	99/05/05	99/06/30	99/08/14	99/09/16	01/05/25
Flyby-No.	C3	C9	C10	C20	C21	C22	C23	C30
Magnetic	✓	✓	✓	x	✓	✓	✓	✓
Radio	x	✓	x	✓	x	✓	✓	x
Up/Down	Down	Up	Down	Down	Down	Down	Down	Down
Day/Night	Day	Night	Day	Night	Both	Night	Night	Both
C/A [km]	1136	418	535	1321	1048	2299	1052	132
h_{CS} $[R_J]$	3.24	-3.52	-2.45	2.93	-1.87	-4.31	1.08	3.50

Table 3.1: Date of flyby (Date), flyby identification number (Flyby-No.), magnetometer measurement (Magnetic), radio occultation measurement (Radio), flyby passing the upstream or/and downstream side (Up/Down), flyby passing the day or/and night side (Day/Night), closest approach altitude (C/A), distance from the magnetospheric current sheet (h_{CS}). This table has been published in similar versions by Seufert (2012) and Liuzzo et al. (2015).

observation, Carlson (1999) derived that Callisto possesses a CO_2 atmosphere with a column density of $0.80^{+0.48}_{-0.48} \times 10^{19}$ m^{-2} and a scale height of ~23 km. Therefore, CO_2 is the species within Callisto's atmosphere that has been observed at first. Up to now, it is the species that has been observed with the most certainty. According to Johnson et al. (2004), Callisto's atmospheric CO_2 could be produced by outgassing, comentary delivery, impact production or radiolysis and photolysis. However, the major source process has not been determined yet. Before 2002, at the time when magnetic field data was firstly interpreted regarding Callisto (see the following Section 3.1.2), the observed CO_2 abundance was the only assumable atmospheric contribution. This picture changed with the report on the discovery of Callisto's ionosphere in 2002.

3.1.2 Magnetic disturbance fields - evidence for a subsurface ocean?

During the flybys C-3 in 1996 and C-9 in 1997, the Galileo spacecraft detected magnetic disturbance fields close to Callisto which can be explained by induced currents within a conductive spherical shell driven by the time-periodic magnetospheric field (Khurana et al., 1998). These data has been interpreted by Khurana et al. (1998), Neubauer (1998), Kivelson et al. (1999) and Zimmer et al. (2000) as evidence for a subsurface ocean at Callisto. As explained by Khurana et al. (1998), the flybys C-3 and C-9 are well suited for identifications of induction

signals since they occurred when Callisto was close to its maximum distance from the current sheet region. Inside the current sheet, magnetic signals from the plasma interaction are expected to dominate over signals from induction due to the enhanced plasma density and the accordingly enhanced plasma interaction strength.

For Callisto and Europa, Zimmer et al. (2000) performed comprehensive modeling studies discussing possible ocean thicknesses and conductivities which could explain the observed magnetic disturbance fields. For Callisto, they found that the conductivity in the moon's interior must exceed 0.02 S m^{-1} at a depth of less than 300 km, which can be explained by a subsurface water ocean. According to the authors, an alternative conductive metallic core would need to be too large to be consistent with gravity measurements reported by Anderson et al. (1998) (see Section 3.1.4). Since an ionosphere was not known at Callisto but at Europa at that time, Zimmer et al. (2000) estimated the role of induction within an ionosphere only for Europa. They compared ionospheric Pedersen conductivities with the minimum required conductivities of an isotropic conductive shell which has the same extend as Europa's ionosphere. They stated that for Callisto, this analysis must await measurements and models of Callisto's ionosphere.

3.1.3 Detection of Callisto's ionosphere - hint of an O$_2$ dominated atmosphere

At first, Gurnett et al. (2000) found hints on Callisto's ionosphere using data of the PWS instrument. During flyby C-10, they detected plasma waves that required electron densities approximately 100 times denser than the ambient magnetospheric electron densities at an altitude of 600 km above Callisto's surface. The authors concluded that a reasonable explanation for this density enhancement would be an ionosphere-like plasma surrounding Callisto.

Roughly two years later, Kliore et al. (2002) proofed the existence of a substantial ionosphere. In their study, they analyzed Galileo radio occultation measurements of flybys C-9, C-20, C-22 and C-23 providing electron density altitude profiles for an altitude range of 0-200 km. Their derived electron density profiles are shown in Figure 3.1. Two measurements were conducted for each flyby, one when Callisto's atmosphere was between the spacecraft and the receiver station on Earth before the spacecraft vanished behind Callisto out of side of the receiver station, the
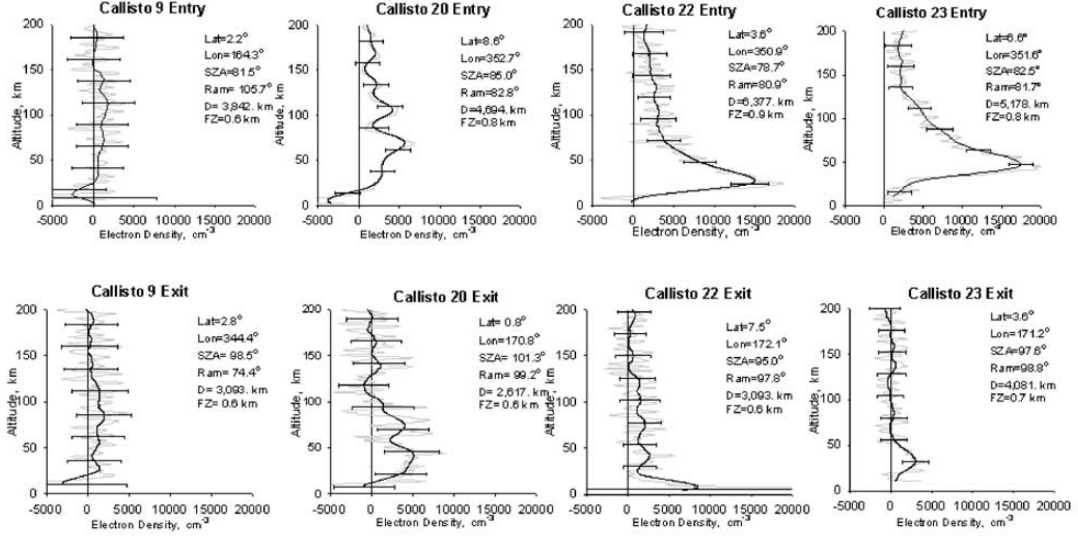
Figure 3.1: Electron density altitude profiles of Callisto's ionosphere as published in Kliore et al. (2002). For the tangential point of the radio occultation line of sight, the following parameters are given in each panel according to the west longitude planetographic coordinate system with Latitude $= 0°$ at the planetographic equator: latitude (LAT), longitude (Lon), solar zenith angle (SZA) and angle to the sub-upstream point (RAM).

'entry' measurement, and one when the spacecraft appeared on the other side of Callisto again, the 'exit' measurement. Figure 3.2 illustrates both cases and the observational principle. The radio occultation measurement delivers the electron column density along the line of sight between spacecraft and receiver station on Earth. From this quantity, Kliore et al. (2002) calculated electron density altitude profiles shown in Figure 3.1 assigned to the location on Callisto where the line of sight is tangential to the surface. Note that in order to derive these profiles, they applied an integral inversion method, which requires the assumption of a spherically symmetric ionosphere.

As visible in the upper right panels of Figure 3.1, Kliore et al. (2002) derived peak ionospheric electron densities up to $\sim 1.5 \times 10^{10}$ m^{-3} during entry observations of flyby C-22 and flyby C-23. They claimed that these ionospheric electron densities are too large to possibly originate only from the known CO_2 atmosphere and suggested that molecular oxygen (O_2) is the major species of Callisto's atmosphere in analogy to Europa, where an oxygen atmosphere had been observed by Hall et al. (1995). Kliore et al. (2002) provided also a first estimation of the density of the assumed O_2 atmosphere. They calculated an O_2 column density of 3-4 $\times 10^{20}$ m^{-2}
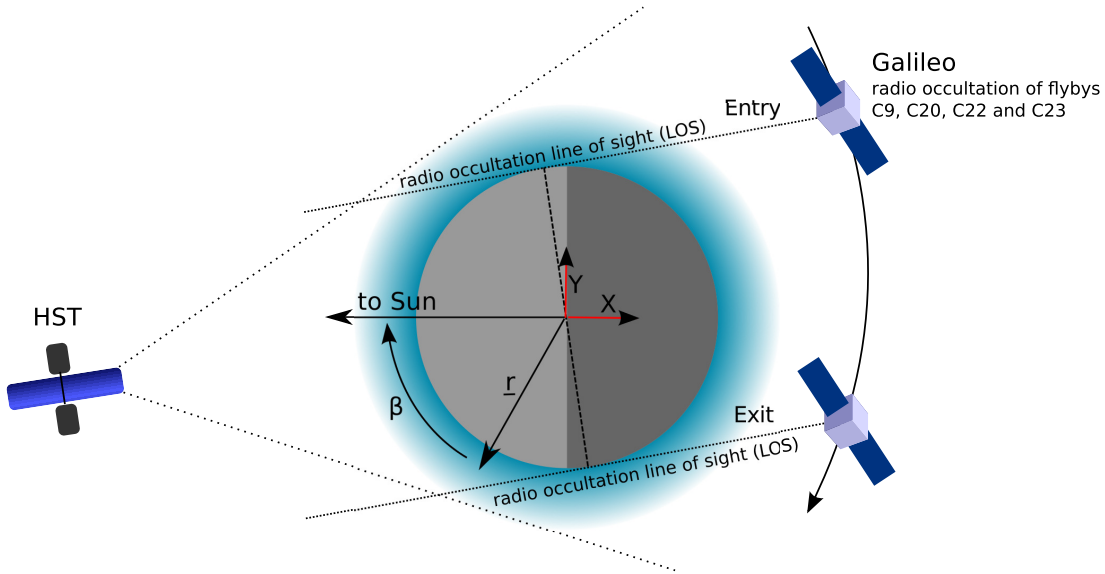
Figure 3.2: Illustration of the observational geometries in Callisto's equatorial plane with sunlit and night side hemispheres illustrated with light and dark shades of gray; The blue shining area illustrates Callisto's atmosphere (here, spherically symmetric); Illustration of the observational geometry of Galileo spacecraft radio occultation and HST/COS observations (not true to scale); Definition of the sun-orientated XY coordinate system within the equatorial plane of Callisto by red arrows; Definition of the subsolar angle, i.e., solar zenith angle, β for an arbitrary position vector $\underline{r}$.

based on the altitudes of the electron density peaks from the flybys C-22 and C-23 and an electron energy-independent chemical equilibrium model of the ionosphere. Since the Galileo spacecraft did not observe substantial ionosphere signals while the leading side was sunlit during C-9, the authors suggested that a substantial ionosphere could only be observed if the orbitally trailing side is sunlit as was the case during C-20, C-22 and C-23. They speculated that surface sputtering at the trailing side accompanied by photoionization might be a necessary precondition for the formation of a substantial atmosphere-ionosphere system.

3.1.4 Surface features and interior

The scientific questions regarding a subsurface ocean and an atmosphere potentially created by surface processes also relate to the physics of the interior and the surface of Callisto. The SSI instrument on-board the Galileo spacecraft took several pictures of Callisto's surface. Exemplary, Figure 3.3 illustrates a full view on Callisto's anti-Jovian hemisphere showing that Callisto's surface is heavily cratered.

Greeley et al. (2000) discussed the Galileo spacecraft observations of Callisto's surface features in detail. Based on different cratering chronological models, they provide estimated ages of many observed structures. These ages reach maximum values on the order of 4 billion years and, therefore, Callisto's surface might date back to the accretion of the Jovian system as already expected from surface observations of the Voyager spacecraft (e.g., Cassen, 1980). Although Greeley et al. (2000) stated that the ages of some structures have model-dependent uncertainties on the order of 75%, we still consider Callisto's surface to be geologically very old on the order of ~1 billion year.

On scales of a few kilometers, Callisto's surface shows a variety of landform structures like, for example, high albedo pinnacles, knobs and ridges. Moore et al. (1999) interpreted such structures as signs for several resurfacing processes such as sputtering ablation, impact erosion and sublimation driven landform modifications. According to the authors, sublimation of ice seems to play a major role regarding resurfacing at Callisto. Also model calculations show that observed pinnacle

Figure 3.3: Callisto's anti-Jovian hemisphere in the visible spectrum as seen by the SSI on-board the Galileo spacecraft. Credit: NASA/JPL/DLR.

structures likely evolve on Callisto's surface due to sublimation weathering, i.e., sublimation and re-sublimation of water molecules (H_2O) (e.g., White et al., 2011).

Regarding Callisto's interior, Anderson et al. (1998) and Anderson et al. (2001) reported on Galileo gravity measurements showing that Callisto's interior is only partially differentiated with ice, rock and metal incompletely separated. Anderson et al. (2001) explained that the rock-metal fraction increases with depth. The mixing of ice and rock-metal reaches down to a depth of at least 1000 km. But the authors noticed that, within the measurement uncertainties, the whole interior might consist of a mixture of ice and rock-metal. Based on their findings, Anderson et al. (2001) preferred either a two layer interior model with a rock-ice-metal core that is surrounded by a 350 km thick layer of relatively clean ice or a comparable three layer interior model that additionally possesses a rock-iron core. Further the authors pointed out that a pure metal core unlikely exists since its formation would also imply a separation of ice and rock due to the high required temperatures. However, a pure rock core might be existent according to the gravity measurements, if its radius is smaller than 25% of Callisto's radius.

According to Khurana et al. (1998), the discovery of a subsurface ocean on the basis of magnetic field measurements was surprising from a geological point of view since the old and heavily cratered surface of Callisto and its partially differentiated interior structure were seen as signs of an inactive interior. But an active interior was supposed to be a necessary precondition for a subsurface ocean as, e.g., the tidal heating driven interior of Europa. For instance, a heat transfer model of Callisto's interior by Cassen (1980) showed that liquid water would freeze out within Callisto's interior since no sufficient heat source was known that could prevent the water from freezing. Also Greeley et al. (2000) did not detect any evidence for current geological activity on Callisto according to the geomorphology while they could not rule out past geological activity completely in a few localized areas. On the other hand, Greeley et al. (2000) also stated that observed multi-ring structures on the surface are consistent with impacts into a thin brittle icy layer overlying a liquid or viscous layer. However, we can not interpret this observation with respect to the present state of Callisto's interior since the associated impact likely happened more than one billion years ago.

Several suggestions have been made to explain the present existence of a subsurface ocean at Callisto in agreement with geological models. Khurana et al.

(1998) suggested that elements like ammonia might be abundant in the subsurface ocean decreasing the melting temperature of water ice and preventing the ocean from freezing. Later Ruiz (2001) and Kuskov and Kronrod (2005) explained that the stress-dependency of water ice viscosities could explain the persistence of a subsurface ocean at Callisto. Moreover, Kuskov and Kronrod (2005) developed a model of Callisto's interior finding that the minimum ocean depth is around 135 km in agreement with all existent geological and geophysical observations. From these studies, we learn that the geology of Callisto could be in agreement with a present subsurface water ocean, but it does not actively support the hypothesis of its existence.

3.2 Studies based on Hubble Space Telescope observations

Subsequently to the discovery of Callisto's ionosphere via Galileo observations, the HST was used to search for signs of Callisto's atmosphere. The observational geometry is schematically illustrated in Figure 3.2. Particularly, oxygen emission was expected to be observed by the HST based on the suggestion by Kliore et al. (2002) saying that Callisto's atmosphere is O_2 dominated. Strobel et al. (2002) reported on a search for the atmospheric components O_2, CO_2 and carbon monoxide (CO) using the Space Telescope Imaging Spectrograph (STIS). STIS was used to measure the emission of the atmosphere in the UV regime. Atmospheric UV emission is caused by electron impact excitation of atmospheric neutral particles. However, Strobel et al. (2002) found that the conducted HST/STIS observations from December 2001 did not show any signature from Callisto's atmosphere within the error bounds. According to this non-detection, the authors derived upper limits for column densities of atmospheric constituents, namely, $\sim 10^{21}$ m^{-2} for pure atmospheres of O_2, CO_2 and CO, 10^{19} m^{-2} for an atmosphere consisting of atomic carbon (C) and 2.5×10^{19} m^{-2} for an atmosphere consisting of O.

In order to estimate the importance of atmospheric UV emission due to electron impact excitation caused by magnetospheric electrons, Strobel et al. (2002) also discussed the interaction between Callisto and the upstream magnetospheric plasma. They found that due to the low strength of the Jovian magnetic field at

Callisto's orbit of about 4-42 nT (Kivelson et al., 2004), the Pedersen conductance of Callisto's ionosphere is much larger than the Alfvén conductance such that the magnetospheric plasma is strongly diverted around the satellite. Since the penetration of magnetospheric electrons into Callisto's atmosphere is inhibited in this case, Strobel et al. (2002) suggested that magnetospheric electron impact ionization is not the driving process of Callisto's ionosphere formation.

In detail, Strobel et al. (2002) derived a peak Pedersen conductance of 0.02 S and a peak Hall conductance of 0.01 S for Callisto's ionosphere. For the underlying calculations of these conductivities, they used atmospheric CO_2 densities according to Carlson (1999) and the electron density altitude profiles of flyby C-22-entry and C-23-entry derived by Kliore et al. (2002). The authors indicated that due to these large ionospheric conductivities, induction within the ionosphere driven by the time-variable magnetic background field could possibly explain the observed magnetic disturbance fields measured during the flybys C-3 and C-9.

Signs of an O_2 atmosphere were finally detected by the HST on November 17, 2011 as reported by Cunningham et al. (2015). The authors found UV emission from Callisto's atmosphere at OI λ130.4 nm and OI λ135.6 nm using the Cosmic Origins Spectrograph (COS) of HST. Note that these multiplets are the first direct observation of O-emission from Callisto's predicted O_2 atmosphere. Cunningham et al. (2015) benefited from the high sensitivity of the COS camera, which was installed on HST in May 2009. Confined to Callisto's disk, the brightness of the observed OI λ135.6 nm emission line is 3.17 ± 1.57 Rayleigh (R) and the brightness of the OI λ130.4 nm emission line is 3.32 ± 2.84 R. From the ratio of both multiplets, Cunningham et al. (2015) derived that Callisto's atmosphere is very likely O_2 dominated. In agreement with Strobel et al. (2002), they showed that photoionization is most likely the dominant driver of the ionosphere formation on Callisto's day side and photoelectrons predominately excite O_2 molecules and generate the observed atmospheric UV emission. This emission can also be called airglow.

From the observed OI λ135.6 nm emission, Cunningham et al. (2015) calculated an atmospheric O_2 column density of $3.4^{+2.0}_{-1.8} \times 10^{19}$ m^{-2}. Their calculation is based on an approximation of the photoelectron impact ionization rate using the study of Wedlund et al. (2011). Further, they used results of an early version of the Atmospheric Ultraviolet Radiance Integrated Code (AURIC) from Strickland et al.

(1999). For a study of Europa's atmosphere of Hall et al. (1995), this algorithm predicted that on average one photon at OI $\lambda 135.6$ nm is emitted per every 40 ion pairs which are produced by direct excitation of magnetospheric electrons and by secondary electrons ejected following ionization within a pure O_2 atmosphere.

As a consequence of the studies of Strobel et al. (2002) and Cunningham et al. (2015), Callisto is expected to be the only Galilean moon where photoelectrons are the dominant driver of the observed atmospheric UV emission. In contrast to Callisto, the atmospheric UV emission at Io, Europa and Ganymede is predominantly caused by upstreaming magnetospheric electrons of the Jovian magnetosphere or electron acceleration processes in the vicinity of the moon (in case of Ganymede) (Saur et al., 1998, 2000; Retherford et al., 2000; Roth et al., 2014; Saur et al., 2015).

3.3 The atmosphere model of Liang et al. (2005)

On the basis of the findings of the Galileo spacecraft and the HST observations from Strobel et al. (2002), Liang et al. (2005) developed an one dimensional photochemical model of Callisto's atmosphere. The authors calculated a vertical neutral density profile for a solar zenith angle of 80°. This angle is roughly the average solar zenith angle of the locations for which electron density altitude profiles have been derived by Kliore et al. (2002) according to the radio occultation measurements 'C-22 entry' and 'C-23 entry' (see Figure 3.1). Liang et al. (2005) considered vertical transport together with the major chemical and photochemical reactions of O_2, CO_2, H_2O, O, CO and associated ions as well as electrons and solar photons. Their model results show that O_2, CO_2 and also H_2O are the most abundant species within Callisto's atmosphere below an altitude of $\sim$130 km and O_2^+ is the major ionospheric ion species. Further, the authors found that the inclusion of H_2O into their model atmosphere reduces the abundance of O which, otherwise, would be larger than the upper limit found by Strobel et al. (2002). Therefore, the model results of Liang et al. (2005) indicate that H_2O molecules are indeed an important component of Callisto's atmosphere.

As the starting point of their model, Liang et al. (2005) set boundary values for the neutral densities at Callisto's surface. In the following, their specific choices are discussed in detail as we will later refer to these considerations, when we

introduce our phenomenological atmosphere model in Chapter 5. As substantial parts of Callisto's surface are covered by water ice, sublimation can produce gaseous H_2O. Liang et al. (2005) assumed that the H_2O density at the surface is given by the equilibrium water vapor pressure above water ice $P(T)$, which depends on the surface temperature T. This relation has been initially derived by Goff and Gratch (1946):

$$log_{10}\left[P(T)\right] = -9.09718\,(273.16/T - 1) - 3.56654\,log_{10}(273.16/T)$$
$$+ 0.876793\,(1 - T/273.16) + log_{10}(6.1071)\;. \tag{3.1}$$

Since then, alternative, slightly different relations have been developed, which are discussed by Murphy and Koop (2005). Liang et al. (2005) used the relation by Goff and Gratch (1946) to set their boundary condition for H_2O according to a surface ice temperature of $\sim$150 K. Further, the authors set the surface O_2 density to 7×10^{15} m^{-3}, so that their model yields similar electron density altitude profiles as derived by Kliore et al. (2002). The surface CO_2 density was set to 4×10^{14} m^{-3} according to the results of Carlson (1999). For all species, Liang et al. (2005) assumed a constant scale height of 30 km, which is a rough average of neutral scale heights that were discussed by Carlson (1999) and Kliore et al. (2002).

3.4 Numerical models of Callisto's plasma interaction

The interaction of the plasma of Jupiter's magnetosphere with Callisto's atmosphere-ionospheres system is relevant for both the interpretation of magnetic field data as well as the transport processes in atmosphere and ionosphere. The interaction of Callisto with the upstreaming magnetospheric plasma is sub-Alfvénic when Callisto is located above or below the plasma sheet of the Jovian magnetosphere. The expected ranges of upstream velocities, magnetic fields and magnetospheric plasma densities indicate that Callisto's interaction might be super-Alfvénic inside the plasma sheet (Kivelson et al., 2004). However, all Galileo flybys occurred when Callisto was located in the magnetospheric lobes where the interaction was sub-Alfvénic.

Beside the estimate of Callisto's plasma interaction strength by Strobel et al. (2002), Callisto's sub-Alfvénic plasma interaction has been investigated by Seufert (2012), Lindkvist et al. (2015), Liuzzo et al. (2015) and Liuzzo et al. (2016) using numerical models. Since the electron gyroradii within the environmental magnetospheric plasma can reach values larger than Callisto's radius, there is an ongoing debate about the proper modeling approach. Seufert (2012) used a MHD approach, where ions and electrons are treated as single fluid, while Lindkvist et al. (2015), Liuzzo et al. (2015) and Liuzzo et al. (2016) used a hybrid approach, where electrons are treated as a fluid and ions are treated semi-kinetically using macro particles.

Seufert (2012) investigated the magnetic fields which were measured during seven Callisto flybys of the Galileo spacecraft. Due to computational reasons he radially stretched his models of Callisto's atmosphere and ionosphere by a factor of ten conserving expected column densities of neutrals and electrons. Further, his model includes magnetic fields created by induction within a subsurface ocean. His simulations yield perturbation amplitudes of the plasma interaction in agreement with the observations during flyby C-10, C-21, C-22 and C-30. For flyby C-3, C-9 and C-23, his modeled perturbation amplitudes exceed the measured values indicating that plasma interaction was weaker as expected during these flybys.

Seufert (2012) also compared modeled electron densities with radio occultation results. In detail, he compared modeled electron densities integrated along the radio occultation line of sight with associated reconstructed line of sight electron column densities of the actual observations. However, the author noted that model and observations are only comparable to a limited degree due to the artificial stretching of the ionosphere. The observations show electron density peaks above the surface (see Figure 3.1) in the case of entry observations during flyby C-22 and flyby C-23. Kliore et al. (2002) interpreted these peaks as evidence for an optical thick atmosphere at the terminator. However, the modeling study of Seufert (2012) indicates that the atmosphere might be optically thin and the observed electron density peaks above the surface at the terminator might be caused by the plasma advection.

Lindkvist et al. (2015) used hybrid simulations to account for the large gyroradii of the upstream magnetospheric ions. By considering an induced magnetic dipole from a subsurface ocean they were able to explain magnetometer data of flyby

C-3 and C-9 confirming the results of Khurana et al. (1998) and Zimmer et al. (2000). However, Lindkvist et al. (2015) did not consider Callisto's ionosphere.

Liuzzo et al. (2015) used hybrid simulations, too, but included an ionosphere in their model setup. Similar to Seufert (2012), they also used a stretched ionosphere due to computational constraints. They found that the strength of the plasma interaction seems to be independent of Callisto's local time. Further, their model results show that the plasma interaction dominates the magnetic perturbation fields in the current sheet and also significantly contributes to perturbation in the magnetospheric lobes with perturbation field strengths that are ~ 0.2 times the magnetic background field. Due to the hybrid approach, the model of Liuzzo et al. (2015) also resolved asymmetric structures in the wake region which are expected to result from the large gyroradii of pick-up ions. In a subsequent study, Liuzzo et al. (2016) analyzed the magnetic field measurements of flyby C-10 in detail. In this case, the authors also demonstrated how they use the hybrid approach to disentangle the magnetic field signature of Callisto's subsurface ocean from the one of the plasma interaction.

3.5 Open scientific questions regarding Callisto and objectives of this study

The Galileo mission and HST observations revealed a lot of interesting information about Callisto, but also gave rise to many questions that still awaits answers. Without claiming to give a complete list, we present some selected outstanding open questions regarding Callisto on the basis of the state of knowledge discussed in this chapter:

- How dense is Callisto's atmosphere and what are the atmospheric constituents?

- Does Callisto's atmosphere possess asymmetries?

- Does Callisto's atmosphere-ionosphere system vary in time?

- What is the main source of Callisto's atmosphere?

- How important is induction in Callisto's conductive ionosphere?

- Does Callisto possess a subsurface ocean?

In this study we aim to find answers to this questions. On the basis of the presented state of knowledge regarding Callisto, we now specify our three main objectives of this study, which we have introduced in the Introduction. The detailed objectives of our study are

1. to constrain density and structure of Callisto's atmosphere based on available observations, in particular the electron density observations from the Galileo flybys C-9, C-20, C-22 and C-23 reported by Kliore et al. (2002) and the HST/COS observations from November 17, 2011 reported by Cunningham et al. (2015) (see Section 3.1.3 and Section 3.2),

2. to determine the impact of possible atmospheric sources on the time-variability of Callisto's atmosphere-ionosphere system and potential observations,

3. to determine the importance of electromagnetic induction in Callisto's ionosphere with respect to the magnetic field measurements from the Galileo flybys C-3 and C-9, which have been interpreted, e.g., by Khurana et al. (1998) as evidence for induction within a subsurface ocean.

In order to achieve these objectives, we develop a model of Callisto's atmosphere-ionosphere system (Chapter 5 and Chapter 6), use this model to constrain Callisto's atmosphere (also Chapter 6) and investigate the sources of Callisto's atmosphere (Chapter 7) and, subsequently, we develop a model of ionospheric induction (Chapter 8).

4 Basics of planetary ionosphere modeling

Before we dive into the development of our model of Callisto's atmosphere-ionosphere system, we present the general idea of planetary ionosphere models in this chapter. On this basis, we explain the development of our physical ionosphere model in Chapter 6. The theory of planetary ionospheres aims to describe the distribution of charged particles within planetary atmosphere as a function of location and energy. Ionospheres are regions of atmospheres where significant numbers of free thermal (<1 eV) electrons and ions are present (Schunk and Nagy, 2009). According to Rees (1989), they are bounded at the bottom by the altitude level at which most of the ionizing radiation or ionizing particles have been absorbed and at the top by the altitude level where the loss of neutral particles becomes important. Historically, the theory of ionospheres has been developed for Earth at first and has been embedded within the field of aeronomy. The term 'aeronomy' has initially described the theory of the chemistry and the physics of Earth's upper atmosphere at altitudes larger than ∼100 km (e.g., Banks and Kockarts, 1973). However, it has become common to use the term 'aeronomy' also with respect to other planetary atmosphere-ionosphere systems.

In planetary atmospheres, a charged particle can be produced by the ionization of a neutral particle due to ionizing electromagnetic radiation (photoionization) or electron impact collisions. The Sun emits ionizing electromagnetic radiation, namely, the solar extreme ultra violet (EUV) and soft X-ray radiation. Electrons causing electron impact ionization can be of solar wind origin like, for example, at Mars, of magnetospheric origin like, for example, at the Galilean moons or secondary electrons that have been generated by photoionization or electron impact ionization. Locally, charged particles can be destroyed by recombination processes, i.e., the formation of a single neutral or multiple neutrals due to a collision of an electron and a single charged ion.

However, not only local processes but also transport processes of the ionospheric charged particles can play a significant role. The ionospheric plasma transport is strongly influenced by the ambient magnetic field configuration, which differs

heavily between different planetary bodies of the solar system. Among others, Earth and Jupiter possess internal dynamo mechanisms creating a first-order dipole magnetic field in their near environment. An other example is Mars, which possesses localized remanent magnetic fields plus a solar wind induced magnetosphere. In a first order approximation, Callisto's magnetic field configuration can be described as the background field of Jupiter's magnetosphere plus secondary contributions from currents induced within Callisto's ionosphere and subsurface. For this reason, we do not adopt existing ionosphere model algorithms from other planetary bodies to describe Callisto's ionosphere in Chapter 6. Instead, we develop our model of Callisto's ionosphere from first principles, at which we estimate the importance of each ionospheric process specifically for the case of Callisto.

Boltzmann's approach is often the starting point for describing local processes and transport processes in planetary ionospheres. According to this approach, every individual particle species can be described by a distribution function in phase space. In the following, we discuss this approach using the example of electrons since the electron distribution function is most relevant for our ionosphere model in Chapter 6. In this regard, electrons can be described by the velocity distribution function $f(\underline{r}, \underline{v}, t)$ in units of m^{-6} s^3 with the location $\underline{r}$, the electron velocity $\underline{v}$ and the time t (e.g., Ashihara and Takayanagi, 1974). Alternatively, electrons can be described by the energy distribution functions $F(\underline{r}, E, t)$ in units of m^{-3} eV^{-1} with the electron energy E if specific velocity directions are investigated or if an isotropic motion can be assumed (e.g., Jasperse, 1976). Often, the electron velocity distribution function is also described by electron intensities $I(\underline{r}, E, \underline{e}_v, t) = (v^2/m_e) f(\underline{r}, \underline{v}, t)$ in m^{-2} s^{-1} eV^{-1}, where $\underline{e}_v$ is the unit vector in the direction of the electron velocity and m_e is the electron mass (e.g., Rees, 1989).

The basis of ionosphere models is the Boltzmann equation, which describes the dynamics of the distribution function of a specific particle species. In terms of the here discussed electron velocity distribution function the Boltzmann equation reads (e.g., Schunk and Nagy, 2009)

$$\left(\partial_t + \underline{v} \nabla_{\underline{r}} + \frac{1}{m_e} \underline{K} \cdot \nabla_{\underline{v}} \right) f(\underline{r}, \underline{v}, t) = \left(\frac{\delta f}{\delta t} \right)_{local} , \qquad (4.1)$$

with the external force $\underline{K}$ and the local change of the distribution function

$(\delta f/\delta t)_{local}$, which is often referred to as the collision term. The left hand side of Equation (4.1) describes the transport of electrons and the right hand side describes the instantaneous changes of particles in space and velocity space due to collisions. The transport is basically driven by the acting force $\underline{K}$, which is in case of planetary ionospheres often given by the Lorentz force and the gravity force.

For the purpose of ionosphere modeling, there exist several approximative solutions of the electron Boltzmann equation. For example, Ashihara and Takayanagi (1974), Jasperse (1976) and Jasperse (1977) focus on the local energy degradation of electrons, i.e., the right hand side of Equation 4.1, while electron transport is neglected or treated approximately. This approach is also called the 'local approximation'. Particularly, the studies of Ashihara and Takayanagi (1974), Jasperse (1976) and Jasperse (1977) provide collision terms for inelastic processes such as photoelectron production, loss and degradation due to collisions of electrons with neutrals. Other authors also discuss solutions of the electron Boltzmann equation including the transport term. Banks and Kockarts (1973) described the so-called two-stream method, which assumes that electrons move only up and down along magnetic field lines. For example, Banks and Kockarts (1973) use this method to describe photoelectron transport in Earth's ionosphere. Other methods to describe ionospheric electron transport are the multi-stream method (e.g., Strickland et al., 1976) or the Monte Carlo method (e.g., Berger et al., 1970). In this case, the given references refer to studies of auroral electrons in Earth's atmosphere.

At Callisto, photoelectrons are expected to drive the ionosphere formation process and the generation of airglow according to Strobel et al. (2002) and Cunningham et al. (2015). Further, we show in Section 6.5.1 that transport does not play a major role in Callisto's lower ionosphere. Therefore, our ionosphere model presented in Chapter 6 is based on the local approximation similar to the studies of Ashihara and Takayanagi (1974), Jasperse (1976) and Jasperse (1977).

5 Phenomenological model of Callisto's atmosphere

Here, we develop an atmosphere model for Callisto which is based on the assumption of three major atmospheric species, namely, O_2, CO_2 and H_2O. The resulting model is a parametrized and phenomenological model, which is applied in combination with our physical ionosphere model as we describe in Chapter 6 to find constraints on Callisto's atmospheric density and structure. Similar to Liang et al. (2005), we assume exponentially decreasing density altitude profiles of all atmospheric species with an universal and constant scale height H of 30 km. Note that this Chapter 5 has been published in a similar version as section 3 in Hartkorn et al. (2017).

5.1 Molecular oxygen - O_2

The atmospheric O_2 density distribution shall be a free parameter in subsequent calculations of ionospheric electron densities and airglow intensities. Therefore, the O_2 part of Callisto's atmosphere is kept variable, but this variability is implemented within a physical framework. At Callisto, atmospheric O_2 is believed to be created by surface sputtering induced by precipitating magnetospheric ions and a series of photochemical reactions of sublimated H_2O molecules (Yung and McElroy, 1977; Johnson, 1990). The sputtering yield of O_2 molecules and the sublimation rate decrease with decreasing surface temperature (Famá et al., 2008), which introduces a day-night asymmetry of the O_2 production rate and probably also a day-night asymmetry of the O_2 density distribution.

To allow for the incorporation of such density asymmetries, we parametrize the atmospheric O_2 column density N_{O2} in the following way,

$$N_{O2}(\beta) = \begin{cases} \frac{1}{2}(N_{O2}^{max} + N_{O2}^{min}) + \frac{1}{2}(N_{O2}^{max} - N_{O2}^{min})\cos(2\beta) & \text{if } \beta \leq \pi/2 \\ N_{O2}^{min} & \text{if } \beta > \pi/2 \, , \end{cases} \tag{5.1}$$

with the maximum O_2 column density N_{O2}^{max}, the minimum O_2 column density
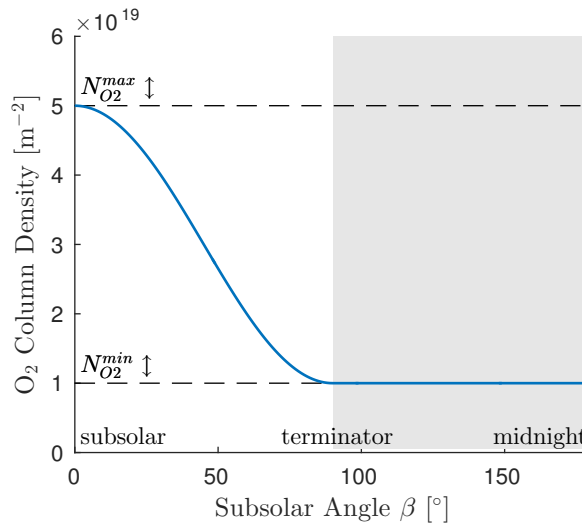
Figure 5.1: O_2 column density distribution as a function of the subsolar angle β. N_{O2}^{max} and N_{O2}^{min} are variable model parameters, here they are exemplary set to $N_{O2}^{max} = 5 \times 10^{19}$ m^{-2} and $N_{O2}^{min} = 1 \times 10^{19}$ m^{-2}. The gray shaded area separates the night side from the day side.

N_{O2}^{min} and β being the angle to the subsolar point at Callisto, i.e., the solar zenith angle (see Figure 3.2). Figure 5.1 shows an exemplary O_2 column density distribution according to Expression (5.1). For multiple variations of the two parameters N_{O2}^{max} and N_{O2}^{min} we apply our ionosphere model to find the best O_2 atmosphere with respect to the available data of ionospheric electron densities and airglow intensities from Galileo and HST observations (see Section 3.1.3 and Section 3.2). Note that these observations probed the day side and the terminator region of Callisto's atmosphere due to the geometrical constraints of the position of observing instruments and the position of Earth as shown in Figure 3.2. As a consequence, we are not able to constrain properties of the atmosphere-ionosphere system at the night side. Therefore, we assume a constant O_2 column density for the night side atmosphere, expressly for $\beta > \pi/2$. Thus, the minimum O_2 column density N_{O2}^{min} represents also the column density at the terminator and the maximum O_2 column density N_{O2}^{max} represents the column density at the subsolar point. In this regard, we refer to

$$F_{as} = N_{O2}^{max}/N_{O2}^{min} \tag{5.2}$$

as asymmetry factor of assumed O_2 atmospheres.

5.2 Carbon dioxide - CO$_2$

The CO$_2$ part of Callisto's atmosphere is assumed to be spherically symmetric with a column density of $N_{CO2} = 0.8^{+0.48}_{-0.48} \times 10^{19}$ m^{-2} based on the observations of Carlson (1999) (see Section 3.1.1). Since the nature of the CO$_2$ atmosphere is not sufficiently understood, we do not consider a spatial asymmetry. However, note that the Galileo spacecraft detected the signals of the CO$_2$ atmosphere when the spacecraft was close to the subsolar region during flyby C-10 (Carlson, 1999; Gurnett et al., 2000). Therefore, the terminator CO$_2$ column density might differ from the derived value. For example, Johnson et al. (2004) mentioned that the CO$_2$ atmosphere might possess an upstream-downstream asymmetry due to an upstream-downstream asymmetry of surficial CO$_2$, which is possibly the source of atmospheric CO$_2$.

5.3 Water vapor - H$_2$O

H$_2$O is expected to play a significant role within Callisto's atmosphere, too (Liang et al., 2005), although it has not been directly observed yet. In analogy to the approach of Liang et al. (2005), we assume that the H$_2$O part of Callisto's atmosphere follows the equilibrium water vapor pressure relation above water ice with respect to the following constructed surface ice temperature distribution,

$$T(\beta) = \frac{1}{2}(T_{max} + T_{min}) + \frac{1}{2}(T_{max} - T_{min})\cos(\beta) \ , \qquad (5.3)$$

with the maximum surface ice temperature T_{max}, the minimum surface ice temperature T_{min} and β the angle to the subsolar point as described above. Thus, we neglect thermal inertia.

The maximum and minimum surface ice temperatures are set according to the surface temperature measurements of Voyager 2 reported by Hanel et al. (1979) with $T_{max} = 155$ K at the subsolar point and $T_{min} = 80$ K at midnight. The H$_2$O column density is then calculated using the expression for the equilibrium water vapor pressure above water ice $P(T)$ (see Equation 3.1) according to the above defined temperature profile. Further, we assume the atmosphere to be in thermal equilibrium with the surface ice temperature (isothermal with respect to
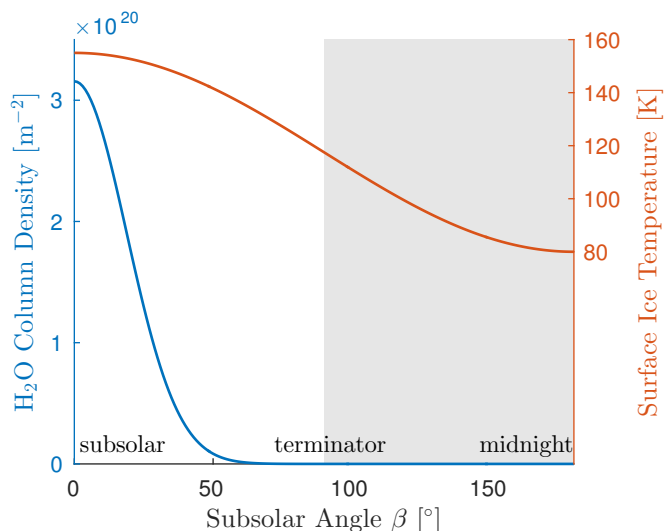
Figure 5.2: Assumed surface ice temperature distribution (red line) and H_2O column density distribution (blue line) as a function of the subsolar angle β with $T_{max} = 155$ K and $T_{min} = 80$ K.

altitudinal variations). Hence, the H_2O column density distribution is given by

$$N_{H2O}(\beta) = \frac{P(T(\beta))\, H}{k_B T(\beta)} \ , \tag{5.4}$$

where k_B is the Boltzmann constant. Figure 5.2 shows the H_2O column density distribution together with the surface ice temperature distribution. The assumed H_2O density distribution is highly asymmetric with a maximum around the subsolar point and an effectively frozen-out H_2O atmosphere on the night side. Note that we neglect atmospheric transport, in particular neutral winds resulting from pressure gradients. Further, the detailed amount of surface water ice which is not tied up as a hydrate is unknown (Johnson et al., 2004). Hence, our phenomenological H_2O atmosphere model represents an upper limit case, especially in the subsolar region.

6 Modeling Callisto's ionosphere

The here presented ionosphere model focuses on a detailed description of Callisto's ionospheric electron population since we aim to calculate electron densities and atmospheric UV emission induced by electron impact collisions. In this regard, we use a kinetic electron energy degradation scheme for suprathermal electrons coupled with a fluid description of the thermal electrons and ions as described, for example, by Stamnes et al. (1983). This scheme is applied to prescribed atmosphere configurations according to the atmosphere model from Chapter 5. We begin with a discussion of the underlying assumptions and simplifications of our ionosphere model in Section 6.1 followed by an in-depth discussion of the model equations in Section 6.2. Our model yields electron energy distribution functions, electron densities and electron temperatures at every location within a prescribed static atmosphere. In Section 6.3, we explain how we derive from our model the two observables, the radio occultation line of sight electron column density and the atmospheric UV emission intensity. In Section 6.4, we present our model results and compare the modeled observables with the according electron density observations from Galileo flybys C-9, C-20, C-22 and C-23 (Kliore et al., 2002) and the HST/COS observation from November 17, 2011 (Cunningham et al., 2015). Subsequently, we discuss possible implications of our model results and the validity of model simplifications in Section 6.5. Note that this Chapter 6 has been published in a similar version as sections 2, 4 and 5 in Hartkorn et al. (2017).

6.1 Underlying assumptions of the ionosphere model

Our model of Callisto's ionosphere is based on three major assumptions:

1. At low altitudes, local collisions between electrons, ions and neutrals dominate over transport processes of electrons since collision time scales are shorter than transport time scales at altitudes below ∼45 km (see Section 6.5.1). Hence, we apply the local approximation.

2. Photoionization is the main source of Callisto's ionosphere at the day side and also in the terminator region (e.g., Cunningham et al., 2015).

3. O_2, CO_2 and H_2O are the major constituents of Callisto's neutral atmosphere (Carlson, 1999; Kliore et al., 2002; Liang et al., 2005; Cunningham et al., 2015).

According to assumption 3, our model includes three neutral species ($N_n = 3$) with the following nomenclature for the index $s \in [1, N_n]$: $s = 1 \rightarrow O_2$, $s = 2 \rightarrow CO_2$ and $s = 3 \rightarrow H_2O$. O_2^+ ions are the dominant ion population within Callisto's atmosphere as shown by Liang et al. (2005) since it has the lowest ionization energy threshold. Ion chemistry evolves on sufficiently short time scales that the original CO_2^+ and H_2O^+ react with neutrals to form O_2^+ and, thus, we can assume that all ions interact with electrons as O_2^+ ions (Liang et al., 2005). A comparison of chemical, diffusion and recombination time scales for CO_2^+ and H_2O^+ is given in Appendix A validating this assumption for the major part of the atmosphere.

As an exception, H_3O^+ might be the dominant ion species close to the subsolar point due to the expected large H_2O abundance at this location. For low values of the investigated O_2 density parameter range, H_2O densities are significantly larger than O_2 densities in the subsolar region. As a consequence, the dominant ion species of the subsolar region will be H_3O^+ if we prescribe O_2 densities from the lower part of the explored parameter space. Initially created H_2O^+ ions would mainly react with H_2O yielding production of H_3O^+ as the associated reaction rate given by Huntress et al. (1973) exceeds the reaction rate for H_2O^+ and O_2 forming O_2^+ given by Rakshit and Warneck (1980). The electron recombination rate for H_3O^+ is by a factor of ~ 1.5 larger than for O_2^+. The consideration of H_3O^+ is, thus, important for electron densities at locations close to the subsolar point. As we neglect the role of H_3O^+ ions, derived electron densities will be overestimated by at most 25% around the subsolar point if the prescribed subsolar O_2 density is relatively minor. However, neglecting the role of H_3O^+ is only locally relevant close to the subsolar point. Therefore, this simplification will not affect later derived O_2 densities when we compare model results with observations since electron density observations, i.e., radio occultation measurements, have probed the terminator regions where O_2^+ is expected to be the dominant ion species.

With our model, we aim to calculate electron distribution functions. Since we apply the local approximation according to assumption 1, the angular electron

distribution is not required and the electron distribution function can be taken as isotropic similar to previous descriptions (e.g., Ashihara and Takayanagi, 1974). Therefore, we describe Callisto's ionospheric electrons using the electron energy distribution function F, which is a function of the position vector $\underline{r}$ and the electron energy E: $F = F(\underline{r}, E)$ in units of $\text{m}^{-3} \text{ eV}^{-1}$.

Coulomb collisions between electrons dominate over other electron collision processes in the low electron energy regime driving the electron distribution function towards a Maxwellian distribution function at electron energies below a few eV (e.g., Ashihara and Takayanagi, 1974). Therefore, we subdivide the total photoelectron population into thermal and suprathermal electrons as it has been done by several authors for other photoionization driven planetary ionospheres (e.g., Chen and Nagy, 1978; Stamnes et al., 1983). Thermal electrons are treated as a fluid while suprathermal electrons are described kinetically. The transition energy E_t between thermal and suprathermal electrons is defined as the energy value where the thermal (Maxwellian) distribution function and the suprathermal (non-Maxwellian) distribution function have equal intensity (e.g., Stamnes et al., 1983).

6.2 Ionosphere model equations

The model equation for suprathermal electrons is given by the transport-free Boltzmann equation for the electron energy distribution function F:

$$
\begin{aligned}
0 &= \left(\frac{\delta F}{\delta t}\right)_{\text{local}} \\
&= \left(\frac{\delta F}{\delta t}\right)_{in}^{en} + \left(\frac{\delta F}{\delta t}\right)_{in}^{ei} + \left(\frac{\delta F}{\delta t}\right)_{el}^{ee} + \left(\frac{\delta F}{\delta t}\right)_{prod}^{e} + \left(\frac{\delta F}{\delta t}\right)_{sec}^{en},
\end{aligned}
\tag{6.1}
$$

which contains only local source and loss terms describing collisions or initial production. Note that Equation (6.1) is derived from Equation (4.1) by applying the local approximation and assuming isotropic distribution functions. On the right hand side of Equation (6.1) (second row), the local changes of the electron energy distribution function are subdivided into collision terms for inelastic electron-neutral collisions $(\delta F/\delta t)_{in}^{en}$, inelastic electron-ion collisions $(\delta F/\delta t)_{in}^{ei}$ and elastic electron-electron collisions $(\delta F/\delta t)_{el}^{ee}$. Additionally, we consider the primary

electron production term $(\delta F/\delta t)^e_{prod}$ and the secondary electron production term $(\delta F/\delta t)^{en}_{sec}$. Due to the large mass difference of electrons in comparison to ions and neutrals, electrons lose only a negligible amount of energy during elastic collisions with neutrals and ions (Rees, 1989). These collisions play an important role regarding the angular distribution of electrons when electron transport is taken into account. Since we neglect electron transport, we also neglect elastic electron-neutral collisions and elastic electron-ion collisions when balancing the electron energy budget.

Thermal electrons are characterized by the macroscopic variables electron density n_e and electron temperature T_e, which are described by the continuity equation

$$0 = P^{th}_{pri} + P^{th}_{sec} + P^{th}_{deg} - \alpha(T_e)n_e n_{i,1} \tag{6.2}$$

and the energy equation

$$
\begin{aligned}
0 = {} & Q^{th}_{pri}(T_e) + Q^{th}_{sec}(T_e) + Q^{th}_{deg}(T_e) + Q_{ee}(n_e, T_e) \\
& - \sum_s \mathbb{L}^{rot}_s(n_e, T_e) - \sum_s \mathbb{L}^{vib}_s(n_e, T_e) - \alpha(T_e)n_e n_{i,1}\frac{3}{2}k_b T_e \ ,
\end{aligned}
\tag{6.3}
$$

where P^{th}_{pri} is the initial production rate of photoelectrons with energies below the transition energy E_t, P^{th}_{sec} the production rate of secondary electrons with energies below E_t, P^{th}_{deg} the degradation rate which is the thermalization rate of suprathermal electrons due to electron-neutral collisions and electron-electron collisions, α the recombination rate coefficient, $n_{i,1}$ the O_2^+ ion density, Q^{th}_{pri} the heating rate due to initial photoelectron production below E_t, Q^{th}_{sec} the heating rate due to secondary electron production below E_t, Q^{th}_{deg} the heating rate due to degradation of electrons from energies above E_t to energies below E_t due to inelastic electron-neutral collisions, Q_{ee} the heating rate due to energy transfer from suprathermal electrons to thermal electrons via Coulomb collisions and $\mathbb{L}^{rot}_s$ and $\mathbb{L}^{vib}_s$ the cooling rates due to rotational and vibrational state excitation of neutrals. Heat conduction is neglected as the associated electron energy transport is expected to play a minor role at low altitudes ($\lesssim 45$ km) similar to our estimates of electron transport at these low altitudes.

The ion density is constrained by mass conservation through

$$0 = P^{ion}_{pri} + P^{ion}_{sec} - \alpha(T_e)n_e n_{i,1} \ , \tag{6.4}$$

where P_{pri}^{ion} is the photoionization rate and P_{sec}^{ion} is the ion production rate due to secondary ionization. For our purpose, we do not need to consider the conservation of ion energy and calculate the ion temperature since this temperature has only a weak influence on the observables, the electron density and the atmospheric UV emission.

Finally, we consider quasi neutrality of the ionospheric plasma

$$n_e \approx n_{i,1} \left(= n_{O_2^+} \right) \ , \tag{6.5}$$

where we also use the assumption that O_2^+ is the dominant ion species.

The full set of model equations is given by the coupled Equations (6.1) - (6.5). In the following, we discuss the appearing terms in more detail. Solutions of the above model equations are found numerically as described in Appendix B yielding calculated suprathermal electron energy distribution functions, thermal electron densities and electron temperatures, i.e., $(F(E), n_e, T_e)$.

6.2.1 Collision terms of suprathermal electrons

According to assumption 2, the primary production term of electrons is given by the energy-dependent photoelectron production rate: $(\delta F/\delta t)_{prod}^e = \sum_s P_{e,s}$. For a given neutral species s, Rees (1989) gives the following expression of this production rate in $m^{-3}\ s^{-1}\ eV^{-1}$:

$$P_{e,s}(\underline{r}, E) = n_{n,s}(\underline{r}) \sum_l \int d\lambda \ I^\infty(\lambda) \ e^{-\tau(\underline{r},\lambda)} \ \sigma_s^i(\lambda) \ p_{sl}(\lambda) \ \delta\left(E - E'_{sl}(\lambda)\right) \ , \tag{6.6}$$

where $n_{n,s}(\underline{r})$ is the neutral particle's number density in m^{-3} at the location $\underline{r}$, l the index denoting possible ion states, λ the wavelength of the incoming photon in nm, I^∞ the solar photon flux as a function of wavelength at the top of Callisto's atmosphere in $m^{-2}\ s^{-1}\ nm^{-1}$, τ the optical depth, σ_s^i the photoionization cross section in m^2, p_{sl} the branching ratio of the final ion state l. E'_{sl} represents the initial photon energy minus the ionization threshold energy (e.g., Rees, 1989):

$$E'_{sl}(\lambda) = hc \left(\frac{1}{\lambda} - \frac{1}{\lambda_{sl}^0} \right) \ , \tag{6.7}$$

where λ_{sl}^0 is the threshold ionization wavelength of the ion state l in nm, h is the Planck constant in eV s and c the speed of light in nm s^{-1}. In Equation (6.6), the delta function $\delta\left(E - E_{sl}'(\lambda)\right)$ with the unit eV^{-1} ensures that the energy of a produced photoelectron is equal to E_{sl}'. The optical depth $\tau(\underline{r}, \lambda)$ is given by (e.g., Rees, 1989)

$$\tau(\underline{r}, \lambda) = \sum_s \sigma_s^a(\lambda) \int_{\underline{\Gamma_r}} n_{n,s}(\underline{r}') \, \mathrm{d}\underline{r}' \, , \qquad (6.8)$$

where σ_s^a is the photon absorption cross section of the neutral species s in m^2 and $\underline{\Gamma_r}$ represents the ray path along the direction to the Sun between location $\underline{r}$ and the top of Callisto's atmosphere. For Equation (6.8), the integration is conducted numerically delivering optical depths for all subsolar angles β (i.e., solar zenith angles).

Photoionization and photon absorption cross sections σ_s^i and σ_s^a of all species are taken from Schunk and Nagy (2009). Branching ratios p_{1l} and threshold wavelengths λ_{1l}^0 of O_2 are taken from Rees (1989), branching ratios p_{2l} and threshold wavelengths λ_{2l}^0 of CO_2 are taken from Schunk and Nagy (2009) and Itikawa (2002) and branching ratios p_{3l} and threshold wavelengths λ_{3l}^0 of H_2O are taken from Schunk and Nagy (2009) and Itikawa (2005). In summary, the set of Expressions (6.6), (6.7) and (6.8) determines the photoelectron production term $(\delta F/\delta t)_{prod}^e$.

The solar photon flux I^∞ is the only external time variable parameter of the photoelectron production term. This time variable flux is implemented through the EUVAC model of Richards et al. (1994) covering a photon wavelength range of 5-105 nm. Since 2003, the Solar EUV Experiment (SEE) on-board the Thermosphere Ionosphere Mesosphere Energetics and Dynamics (TIMED) mission spacecraft measures the solar photon flux at $\sim$1 AU providing a better resolution than the EUVAC model and a smaller cutoff wavelength of 0.5 nm. However, as we simulate configurations of Galileo flybys from before 2003 (C-9, C-20, C-22, C-23), we use EUVAC fluxes for our model.

Figure 6.1 shows a comparison of EUVAC fluxes (gray bars) with TIMED/SEE fluxes (green line) at Callisto's solar distance on November 17, 2011, the date of the HST/COS observation of Callisto's atmospheric UV emission reported in Cunningham et al. (2015). This comparison shows that the EUVAC fluxes and the TIMED/SEE fluxes do not significantly differ at this specific day except that
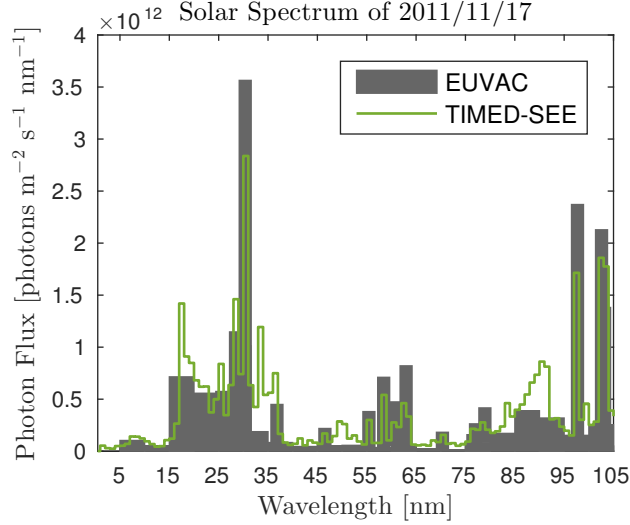
Figure 6.1: Solar photon fluxes at Callisto's solar distance on November 17, 2011. The green line marks the solar photon fluxes obtained by using the TIMED/SEE data and the gray bars mark the solar photon fluxes obtained from the EUVAC model.

the TIMED/SEE flux distribution exhibits higher resolved fine structures and also covers the wavelength range of 0.5-5 nm.

Due to the lower cutoff wavelength of 0.5 nm, the TIMED/SEE photon flux includes also most of the soft x-ray radiation, which ranges from 0.1 nm to 7 nm. At Callisto, soft x-ray radiation plays only a minor role in the ionosphere formation. According to the observations of Carlson (1999) and Cunningham et al. (2015), we expect Callisto's atmosphere to be optically thin and to be composed of O_2, CO_2 and H_2O as discussed in Chapter 5. For such an atmosphere, we calculate electron production rates using the TIMED/SEE fluxes showing that less than 1% of the total photoelectron production and less than 3% of the total photoelectron energy production is caused by photons with wavelengths smaller than 5 nm, which are not included in the EUVAC model. As our model works with TIMED/SEE fluxes and EUVAC fluxes as well, we find that with respect to the date of November 17, 2011, our model results are not significantly affected by the choice of the flux type and the lower cutoff wavelength. Hence, we conclude that the EUVAC model sufficiently describes the ionizing solar radiation for the purpose of our aeronomic calculations regarding Callisto.

Figure 6.2 shows EUVAC solar photon fluxes according to the times of flybys C-9, C-20, C-22 and C-23 and the HST/COS observation from November 17, 2011. EUVAC solar fluxes during C-20, C-22, C-23 and the HST/COS observation are
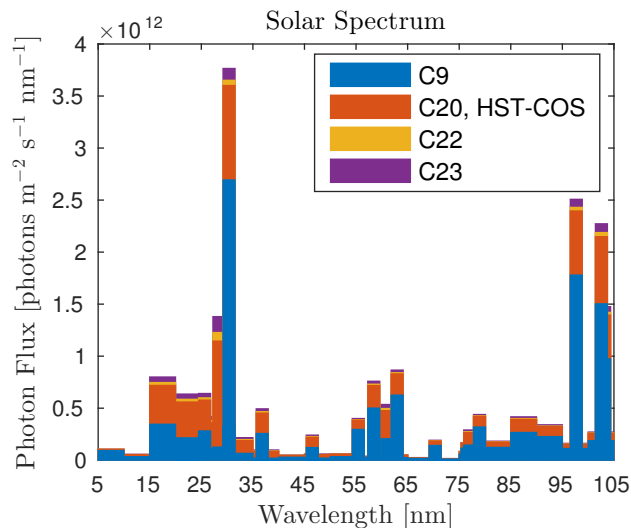
Figure 6.2: EUVAC solar photon fluxes at Callisto's solar distance for C-9, C-20, C-22, C-23 and the HST/COS observation. The fluxes are plotted overlapping. The largest fluxes occurred during C-23 while the smallest fluxes occurred during C-9. The according dates are: C-9: 1997/06/25, C-20: 1999/05/05, C-22: 1999/08/14, C-23: 1999/09/16, HST/COS: 2011/11/17.

quite similar, in fact, EUVAC fluxes during C-20 and the HST/COS observation are nearly indistinguishable. During C-9 the EUVAC model predicts solar fluxes that are on average $\sim$35% lower than during the other observations.

Based on the EUVAC fluxes from November 17, 2011, Figure 6.3 shows the calculated discretized photoelectron spectrum of an exemplary atmospheric volume element. Photoelectrons are produced non-uniformly in energy space between 0.3 eV and $\sim$100 eV. Only a negligible amount of electrons ($< 1\%$) and electron energy ($< 3\%$) is produced above 100 eV. There is a strong peak at 0.6 eV, which results from the 97.702 nm CIII resonance peak of the solar photon flux spectrum (see also Figure 6.1). This photoelectron production peak is very distinct since only the lowest ion states of O_2^+ and H_2O^+ with threshold energies of 12.1 eV and 12.64 eV can get excited by photons with a wavelength of 97.702 nm, which corresponds to an energy of 12.7 eV. A second more diffuse peak is located around 25 eV, which is caused by the prominent 30.331 nm HeII resonance peak of the solar spectrum. The associated photons with energies of 40.8 eV can excite several different ion states causing the diffuse peak characteristic. Note that photoelectrons with energies larger than $\sim$14 eV cause dissociative excitation of O_2, which is the underlying process of the atmospheric UV emission at the oxygen
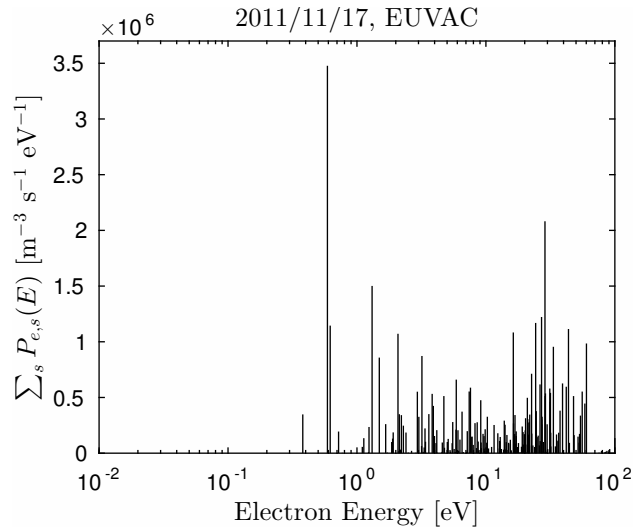
Figure 6.3: Photoelectron production rate $\sum_s P_{e,s}$ as a function of photoelectron energy (photoelectron spectrum) of an exemplary volume element at Callisto's solar distance with O_2 density $n_{n,1} = 1.0 \times 10^{15}$ m^{-3}, CO_2 density $n_{n,2} = 0.25 \times 10^{15}$ m^{-3} and H_2O density $n_{n,3} = 1.0 \times 10^{15}$ m^{-3}. These rates are calculated by using the EUVAC solar photon fluxes from November 17, 2011, shown in Figure 6.1.

lines OI λ135.6 nm and OI λ130.4 nm that has been discovered by Cunningham et al. (2015) using HST/COS observations (see Section 3.2).

After the description of the primary electron production term, we focus now on the remaining collision terms in Equation (6.1). Our model contains the energetically important inelastic collisions of electrons with O_2, CO_2, H_2O including secondary ionization, dissociative recombination with O_2^+ ions as well as electron-electron collisions. For a given neutral species s, an electron-neutral collision process of type t_s is characterized by its species-specific energy-dependent cross section $\sigma_{st_s}(E)$ and the associated discrete electron energy loss ϵ_{st_s}, where t_s counts all possible collision processes up to the total amount of processes T_s. The set of electron collisions with O_2 includes electron impact ionization, electron impact dissociation, excitation of the electronic states a$^1\Delta$, b$^1\Sigma$, 3Π, ACc, Schumann-Runge continuum (SR) and unidentified states (uid), excitation of the rotational state J 1-3 and excitation of the vibrational states $\nu = 1, 2, 3, 4$ excited from the ground state $\nu = 0$. The set of electron collisions with CO_2 includes electron impact ionization, excitation of the electronic states $^1\Sigma_u^+$ and $^1\Pi_u$, excitation of the rotational state J 0-2 and excitation of the vibrational states $(100), (010)$, and (001), excited from the ground state (000). The set of

41

Physical Process	Energy Loss	Cross Section Reference
O_2	ϵ_{1,t_1}	
rotational excitation J 1-3	*0.01 eV	Itikawa (2009)
vibrational excitation $\nu = 0 - 1$	0.29 eV	Allan (1995)
vibrational excitation $\nu = 0 - 2$	0.49 eV	Allan (1995)
vibrational excitation $\nu = 0 - 3$	0.68 eV	Allan (1995)
vibrational excitation $\nu = 0 - 4$	0.87 eV	Allan (1995)
electronic excitation $a^1\Delta$	0.98 eV	Itikawa (2009)
electronic excitation $b^1\Sigma$	1.63 eV	Itikawa (2009)
electronic excitation ACc	4.20 eV	Itikawa (2009)
dissociation	5.12 eV	Anzai et al. (2012)
electronic excitation SR	7.10 eV	Itikawa (2009)
electronic excitation 3Π	8.10 eV	Itikawa (2009)
electronic excitation uid	8.90 eV	Itikawa (2009)
ionization	12.10 eV	Hwang (1996)
dissociative excitation 135.6 nm	14.26 eV	Kanik et al. (2003)
dissociative excitation 130.4 nm	14.62 eV	Kanik et al. (2003)
CO_2	ϵ_{2,t_2}	
rotational excitation J 0-2	*0.01 eV	Takayanagi et al. (1970)
vibrational excitation (010)	0.06 eV	Itikawa (2002)
vibrational excitation (100)	0.16 eV	Itikawa (2002)
vibrational excitation (001)	0.18 eV	Itikawa (2002)
electronic excitation Σ_u^+	11.00 eV	Itikawa (2002)
electronic excitation $^1\Pi_u$	11.39 eV	Itikawa (2002)
ionization	13.80 eV	Itikawa (2002)
H_2O	ϵ_{3,t_3}	
rotational excitation J 0-1	*0.01 eV	Itikawa (2005)
vibrational excitation (010)	0.20 eV	Itikawa (2005)
vibrational excitation (100)+(001)	0.46 eV	Itikawa (2005)
electronic excitation 3B_1	10.40 eV	Anzai et al. (2012)
ionization	12.62 eV	Itikawa (2005)

Table 6.1: List of inelastic electron-neutral collisions and associated discrete energy losses. *Energy loss of rotational excitation of O_2, CO_2 and H_2O is implemented in the model according to the method of Swartz (1985) with cross sections rescaled by a factor of 0.2, 0.02 and 0.4, respectively, the real energy loss is 2.0×10^{-3} eV for O_2, 2.0×10^{-4} eV for CO_2 and 4.0×10^{-3} eV for H_2O.

electron collisions with H_2O includes electron impact ionization, excitation of the electronic state 3B_1, excitation of the rotational state J 0-1 and excitation of the vibrational states (100), (010) and (001), excited from the ground state (000). Table 6.1 shows all considered electron-neutral collision processes together with the used discrete energy loss values and references for the associated cross section data.

In order to incorporate electron production due to secondary electron impact ionization, we use the expression for the normalized electron impact ionization

double cross section $\sigma_{I,s}(E_p, E'_{new})$ of Opal et al. (1971), scaled with recent total ionization cross section data of O_2, CO_2 and H_2O presented by Anzai et al. (2012). In the context of secondary electron impact ionization, E_p is the energy of the primary electron before the collision, E'_{new} is the energy of the newly produced secondary electron (after the collision) and I_s is the electron impact ionization threshold energy. Since the amount of kinetic energy transferred to the newly created ion can be neglected, these energies are related to each other by $E'_{new} = E_p - I_s$ (Opal et al., 1971).

We approximate the discrete energy loss of electron impact ionization by the energy of the newly created electron plus the ionization threshold energy needed to produce the ion ground state, which is the most probable final ion state for O_2, CO_2 and H_2O within the investigated electron energy range. However, we use total ionization cross sections which include also ionizations of higher order ion states. Since, therefore, we neglect the additional energy loss from excitations of higher order ion states, the energy loss by electron impact ionization is underestimated by approximately 15%. This error has been estimated by comparing the applied energy loss to an average energy loss, which is calculated by averaging the threshold energies of all ion excitation states weighted by the associated excitation probabilities.

Summing up all mentioned electron-neutral collision processes, the inelastic electron-neutral collision term is then given by (e.g., Ashihara and Takayanagi, 1974)

$$\left(\frac{\delta F}{\delta t}\right)_{in}^{en} = \sqrt{\frac{2}{m_e}} \sum_s^{N_n} n_{n,s} \int_{I_s}^{\hat{E}} \mathrm{d}\tilde{E} \sqrt{E+\tilde{E}} \; \sigma_{I,s}(E+\tilde{E}, \tilde{E}-I_s) F(E+\tilde{E})$$

$$+ \sqrt{\frac{2}{m_e}} \sum_s^{N_n} n_{n,s} \sum_{t_s=1}^{T_s-1} \sqrt{E+\epsilon_{st_s}} \; \sigma_{st_s}(E+\epsilon_{st_s}) F(E+\epsilon_{st_s}) \qquad (6.9)$$

$$- \sqrt{\frac{2}{m_e}} \sum_s^{N_n} n_{n,s} \sum_{t_s=1}^{T_s} \sqrt{E} \; \sigma_{st_s}(E) F(E) \;,$$

where the first term on the right hand side (first row) represents the source of electrons of energy E due to degradation of electrons after ionizing collisions. The second term (second row) represents the electron source due to degradation of electrons after non-ionizing collisions and the third term (third row) represents

the loss due to degradation of electrons of energy E. The electron-neutral collision marked by the index $t_s = T_s$ is the electron impact ionization process and $\hat{E}$ denotes the maximum energy above which no photoelectron is produced. The production of secondary electrons from ionizing electron-neutral collisions is implemented through (e.g., Ashihara and Takayanagi, 1974)

$$\left(\frac{\delta F}{\delta t}\right)^{en}_{sec} = \sqrt{\frac{2}{m_e}} \sum_s^{N_n} n_{n,s} \int_{I_s}^{\hat{E}} \mathrm{d}\tilde{E} \ \sqrt{E + \tilde{E}} \ \sigma_{I,s}(E + \tilde{E}, E) \ F(E + \tilde{E}) \ . \quad (6.10)$$

The most important inelastic electron-ion collision is dissociative recombination of electrons with O_2^+ as it dominates over other electron-ion processes below collision energies of 15 eV (Sheehan and St Maurice, 2004). Dissociative recombination cross sections $\sigma_{rec,1}$ of O_2^+ are given by Peverall et al. (2001) up to collision energies of 3 eV. For our purpose, recombination can be neglected above this data limit of 3 eV since collision rates of inelastic electron-neutral collisions and elastic electron-electron collisions dominate over recombination rates for energies larger than 3 eV. For a given O_2^+ ion density $n_{i,1}$, the associated recombination collision term is given by (e.g., Ashihara and Takayanagi, 1974)

$$\left(\frac{\delta F}{\delta t}\right)^{ei}_{in} = -\sqrt{\frac{2}{m_e}} \ n_{i,1} \ \sqrt{E} \ \sigma_{rec,1}(E) \ F(E) \ . \quad (6.11)$$

Energy is exchanged between electrons via Coulomb collisions. In contrast to the discrete energy loss from collisions with neutrals, suprathermal electrons lose energy continuously by Coulomb collisions with thermal electrons. In order to describe this process for suprathermal electrons, we use the effective electron-electron collision cross section $\sigma_{ee}(E, n_e, T_e)$ introduced by Nagy et al. (1970), which is a function of suprathermal electron energy, thermal electron density and temperature. This cross section is given by

$$\sigma_{ee}(E, n_e, T_e) = \frac{1}{\Delta E} \frac{1}{n_e} \left(\frac{\mathrm{d}E}{\mathrm{d}x}\right) \ , \quad (6.12)$$

where ΔE is the discretized energy loss that is set to the numerical energy bin width, $(1/n_e)(\mathrm{d}E/\mathrm{d}x)$ is the suprathermal electron energy loss rate per unit length in m^2 eV. Swartz and Nisbet (1971) give the following approximative analytic expression for this loss rate based on fitting the results of Butler and Buckingham

(1962):

$$\frac{1}{n_e}\left(\frac{\mathrm{d}E}{\mathrm{d}x}\right) \approx \frac{5.10 \times 10^{-12}}{E^{0.94} n_e^{0.03}} \left(\frac{E - E_0}{E - 0.53\, E_0}\right)^{2.36} , \qquad (6.13)$$

with $E_0 = 8.617 \times 10^{-5} T_e$, temperatures in K, densities in m^{-3} and energies in eV. Thus, the applicable electron-electron collision term is given by

$$\begin{aligned}
\left(\frac{\delta F}{\delta t}\right)^{el}_{ee} = {} & \sqrt{\frac{2}{m_e}}\; n_e\; \sqrt{E + \Delta E}\; \sigma_{ee}(E + \Delta E, n_e, T_e)\; F(E + \Delta E) \\
& - \sqrt{\frac{2}{m_e}}\; n_e\; \sqrt{E}\; \sigma_{ee}(E, n_e, T_e)\; F(E) .
\end{aligned} \qquad (6.14)$$

6.2.2 Sources and sinks of thermal electrons, ions and thermal electron energy

Thermal electrons are produced by (a) initial photoionization and (b) secondary ionization producing electrons with energies smaller than the transition energy and (c) degradation of suprathermal electrons down below the transition energy. The corresponding production terms listed in Equation (6.2) are given by:

$$\text{(a) } P^{th}_{pri} = \sum_s \int_0^{E_t} P_{e,s}(E)\, \mathrm{d}E , \qquad (6.15)$$

$$\text{(b) } P^{th}_{sec} = \int_0^{E_t} \left(\frac{\delta F}{\delta t}\right)^{sec}_{en} \mathrm{d}E , \qquad (6.16)$$

$$\text{(c) } P^{th}_{deg} = -\int_{E_t}^{\hat{E}} \left[\left(\frac{\delta F}{\delta t}\right)^{in}_{en} + \left(\frac{\delta F}{\delta t}\right)^{ee}_{el}\right] \mathrm{d}E . \qquad (6.17)$$

The associated heating rates listed in Equation (6.3) are given by:

$$\text{(a) } Q^{th}_{pri}(T_e) = \sum_s \int_0^{E_t} P_{e,s}(E) \left(E - \frac{3}{2} k_B T_e\right) \mathrm{d}E , \qquad (6.18)$$

$$\text{(b) } Q^{th}_{sec}(T_e) = \int_0^{E_t} \left(\frac{\delta F}{\delta t}\right)^{sec}_{en} \left(E - \frac{3}{2} k_B T_e\right) \mathrm{d}E , \qquad (6.19)$$

$$\begin{aligned}
\text{(c) } Q^{th}_{deg}(T_e) = {} & \sqrt{\frac{2}{m_e}} \sum_s^{N_n} n_{n,s} \sum_{t_s}^{T_s} \int_{E_t}^{E_t + \epsilon_{s,t_s}} \sqrt{E} \\
& \times\; \sigma_{s,t_s}(E)\; F(E) \left(E - \epsilon_{s,t_s} - \frac{3}{2} k_B T_e\right) \mathrm{d}E .
\end{aligned} \qquad (6.20)$$

The heating rate Q_{deg}^{th} includes only the heating due to discrete degradation through electron-neutral collisions, electron-electron collisions are treated separately. Heating rates (a) - (c) are minor in comparison to the heating rate Q_{ee} that is generated by electron-electron collisions (Schunk and Nagy, 1978). Since electron-electron collisions only redistribute energy within the electron population, the heating rate of thermal electron is given by the negative integrated cooling rate of suprathermal electrons (Hoegy, 1984), i.e.,

$$
\begin{aligned}
Q_{ee}(n_e, T_e) = & -\int_{E_t}^{\hat{E}} \left(\frac{\mathrm{d}F}{\mathrm{d}t}\right)_{ee}^{el} \left(E - \frac{3}{2}k_B T_e\right) \, \mathrm{d}E \\
= & \sqrt{\frac{2}{m_e}} \sqrt{E_t} \, F(E_t) \left(\frac{\mathrm{d}E}{\mathrm{d}x}\right) \left(E_t - \frac{3}{2}k_B T_e\right) \\
& + \sqrt{\frac{2}{m_e}} \int_{E_t + \Delta E}^{\hat{E}} \sqrt{E} \, F(E) \left(\frac{\mathrm{d}E}{\mathrm{d}x}\right) \mathrm{d}E \, .
\end{aligned} \tag{6.21}
$$

Within our model, the only loss process of thermal electrons is dissociative recombination with the major ion O_2^+. The corresponding reaction coefficient α is given by Sheehan and St Maurice (2004) as a function of electron temperature:

$$
\alpha(T_e) = 1.95 \times 10^{-13} \ \mathrm{m^3 s^{-1}} \left(\frac{T_e}{300 \ \mathrm{K}}\right)^h , \tag{6.22}
$$

$$
\text{with } h = \begin{cases} -0.70, & \text{if } T_e \leq 1200 \ \mathrm{K} \\ -0.56, & \text{if } T_e > 1200 \ \mathrm{K} \, . \end{cases} \tag{6.23}
$$

The corresponding loss of energy is implemented through $\alpha(T_e) \, n_e \, n_{i,1} \, (3/2 \, k_b T_e)$ (see also Equation (6.2)).

Inelastic electron-neutral collisions leading to excitation of rotational and vibrational states play an important role regarding energy loss of thermal electrons. Analytic expressions for cooling rates generated by rotational state excitation of O_2, CO_2 (Dalgarno, 1969) and H_2O (Cravens et al., 1986) are given in units of eV m^{-3} s^{-1}:

$$
O_2 : \quad \mathbb{L}_1^{rot}(n_e, T_e) = 6.9 \times 10^{-20} \, n_e \, n_{n,1} \, \frac{T_e - T_n}{T_e^{1/2}} , \tag{6.24}
$$

$$
CO_2 : \quad \mathbb{L}_2^{rot}(n_e, T_e) = 5.8 \times 10^{-20} \, n_e \, n_{n,2} \, \frac{T_e - T_n}{T_e^{1/2}} , \tag{6.25}
$$

$$\text{H}_2\text{O}: \quad \mathbb{L}_3^{rot}(n_e, T_e) = n_e \, n_{n,3} \, \left(a + b \ln \left(\frac{T_e}{T_n} \right) \right) \left(\frac{T_e - T_n}{T_e^{5/4}} \right) , \tag{6.26}$$

$$\text{with } a = 1.052 \times 10^{-14} + 6.043 \times 10^{-16} \ln(T_n) \tag{6.27}$$

$$\text{and } b = 4.180 \times 10^{-15} + 2.026 \times 10^{-16} \ln(T_n) , \tag{6.28}$$

where all densities are in m^{-3}, temperatures are in K and T_n is the temperature of the neutrals which is approximated by 120 K corresponding to the average surface temperature of Callisto's day side hemisphere (Hanel et al., 1979). For rotational state excitation of neutrals, the neutral temperature needs to be taken into account since electrons with energies comparable to the energies of the neutral particles can still excite rotational states.

Vibrational state excitation thresholds are at least one order of magnitude larger than rotational state excitation thresholds. Therefore, we neglect the neutral temperature dependency of vibrational cooling. For each neutral species s, these cooling rates are then given by

$$\mathbb{L}_s^{vib}(n_e, T_e) = n_e \, n_{n,s} \, \sqrt{\frac{1}{\pi m_e}} \left(\frac{2}{k_B T_e} \right)^{3/2} \sum_m E_{s,m}^{vib}$$
$$\times \int_0^{\hat{E}} E \, \sigma_{s,m}^{vib}(E) \, e^{-\frac{E}{k_B T_e}} \, dE , \tag{6.29}$$

where the sum is taken over different vibrational excitation states m which are the same as for suprathermal electrons (see Table 6.1). Vibrational state excitation cross sections $\sigma_{s,m}^{vib}$ (in m^2) and vibrational state excitation energies $E_{s,m}^{vib}$ (in eV) are taken from Allan (1995) and Itikawa (2009) for O_2, from Itikawa (2002) for CO_2 and from Itikawa (2005) for H_2O. These cross sections are also listed in Table 6.1 with respect to suprathermal electrons.

Primary and secondary ion production rates are given by

$$P_{pri}^{ion} = \sum_s^{N_n} \int_0^{\hat{E}} P_{e,s}(E) \, dE , \tag{6.30}$$

$$P_{sec}^{ion} = \sqrt{\frac{2}{m_e}} \sum_s^{N_n} n_{n,s} \int_{E_t}^{\hat{E}} \sqrt{E} \, \sigma_{sT_s}(E) F(E) \, dE , \tag{6.31}$$

with the electron impact ionization cross section $\sigma_{sT_s}(E) = \int_0^\infty \sigma_{I,s}(E, E') \, dE'$.

Ions get lost in the same way as electrons due to dissociative recombination as described by Equation (6.4).

6.3 Extracting electron densities and ultraviolet emission intensities

In the following section, we describe how we extract the observables, the radio occultation line of sight electron column density and the atmospheric UV emission intensity, from the solution $(F(E), n_e, T_e)$ of our model equations (6.1)-(6.5) for comparison with the observations of Kliore et al. (2002) and Cunningham et al. (2015).

6.3.1 Line of sight electron column densities

Kliore et al. (2002) published electron density altitude profiles of radio occultation entry and exit observations of Galileo flybys C-9, C-20, C-22 and C-23 (see Figure 3.1). As mentioned in Section 3.1.3, these profiles were calculated under the assumption of a spherically symmetric ionosphere. We cannot directly compare electron density altitude profiles of Kliore et al. (2002) with our model results since our photoionization driven model yields strong day-night asymmetries of the ionosphere. Therefore, we use a similar approach as described by Seufert (2012), i.e., we calculate the electron column densities N_{LOS}^e of the radio occultation line of sight (LOS) using both, the spatial electron density distribution $n_e(\underline{r})$ from our model and from results of Kliore et al. (2002):

$$N_{\mathrm{LOS}}^e(\underline{r}_t, z_{int}) = \int_{\underline{\Gamma}^{\mathrm{LOS}}(\underline{r}_t, z_{int})} n_e(\underline{r}') \, \mathrm{d}\underline{r}' \, , \qquad (6.32)$$

with $\underline{\Gamma}^{\mathrm{LOS}}(\underline{r}_t, z_{int})$ representing the path of the LOS as a function of latitude and longitude $(\underline{r}_t)$ where the LOS is tangential and, thus, closest to Callisto's surface. Further, z_{int} represents the altitude of the closest approach of the LOS. The LOS electron column density N_{LOS}^e allows a direct comparison between observation and model.

Figure 6.4 illustrates how we determine the quantity N_{LOS}^e for both model and observation. In Figure 6.4, we use the sun-oriented XY coordinate system, which
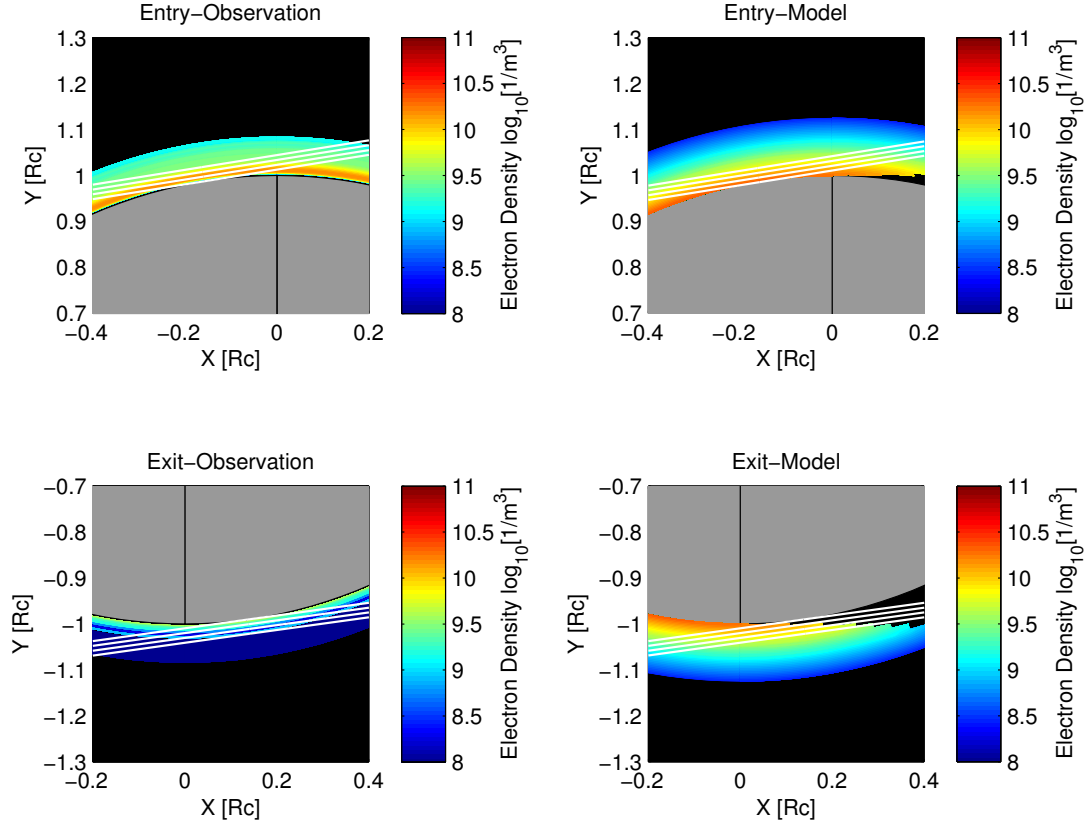
Figure 6.4: Electron densities of the terminator regions in the equatorial plane according to the C-22 entry and exit electron density altitude profiles of Kliore et al. (2002) (left panels) and according to an exemplary model ionosphere with configurations of flyby C-22 (right panels). For the model results (right panels), the prescribed atmosphere for the C-22 observation is spherically symmetric with an O_2 column density of 3.0×10^{19} m^{-2}. The geometry with respect to the sunlight yields an asymmetric ionosphere. White lines correspond to radio occultation LOS during entry (upper row) and exit (lower row) of flyby C-22. In this Cartesian coordinate system, the Sun is in the -X direction and the Y-axis is in the equatorial plane. Length scales are given in units of Callisto's radius $R_C = 2410$ km.

we have introduced in Figure 3.2. The X-axis corresponds to the Sun-Callisto axis, the Sun is shining from the -X direction and the Y-axis is in the equatorial plane. This coordinate system is well suited to describe the photoionization driven day side ionosphere of Callisto. All panels of Figure 6.4 show electron densities in the equatorial plane with focus on the terminator regions. Both left panels show a spherically symmetric ionosphere that is extracted from the radio occultation data (Kliore et al., 2002, their figure 2) of C-22 entry (upper left panel) and exit (lower left panel). The right panels of Figure 6.4 show a day-night asymmetric ionosphere

	C-9	C-20	C-22	C-23
entry ϕ_T	164.3°	352.7°	350.9°	351.6°
entry θ_T	88.8°	81.4°	86.4°	83.4°
exit ϕ_T	344.4°	170.8°	172.1°	171.2°
exit θ_T	87.2°	89.2°	82.5°	86.4°

Table 6.2: Spherical coordinates (ϕ_T,θ_T) of electron altitude profile foot points (tangential points $\underline{r}_t$) in degree according to the west longitude planetographic coordinate system taken from Kliore et al. (2002) (see Figure 3.1). In this case, the point where $\theta_T = 0$ is located at the northern planetographic pole.

which is a result of our model. All panels also show white lines representing the radio occultation LOSs of four different closest approach altitudes z_{int} (0 km, 25 km, 50 km and 75 km) for C-22 entry (upper panels) and exit (lower panels). For both the results of Kliore et al. (2002) and the results of our model, we derive the LOS electron column densities by integrating the electron densities along the LOSs that are represented by these white lines. In case of $z_{int} = 0$, the LOS is assumed to be tangential to the surface crossing the tangential point $\underline{r}_t$. The LOS of integration altitudes larger than zero are assumed to be shifted parallel to the tangential LOS radially outward. The choice of the integration altitudes is based on the altitude profiles from Kliore et al. (2002). Table 6.2 lists the spherical coordinates of the tangential points $\underline{r}_t$ of entries and exits of all four flybys according to the west longitude planetographic coordinate system. This geometric information was taken from figure 2 of Kliore et al. (2002), which is shown in Figure 3.1.

For our model, electron density distributions along radio occultation LOSs are derived from solving the model equations (6.1)-(6.5) for each volume element along the LOSs. Therefore, we directly calculate the electron energy distribution functions and associated electron densities along equally spaced 1-D grids of radio occultation LOSs, for which we use 600 grid points with a spatial resolution of $\sim$8 km. We find that higher resolutions do not significantly change the model results.

6.3.2 Ultraviolet emission intensities

From the electron energy distribution functions of all atmospheric volume elements, we calculate the brightness of the disk averaged atmospheric UV emission I_λ in R

for the OI $\lambda 135.6$ nm and OI $\lambda 130.4$ nm multiplets and the HI $\lambda 121.6$ nm line similar to Saur et al. (1998):

$$
\begin{aligned}
I_{130.4} = {} & \frac{10^{-10}}{R_C^2 \pi} \sqrt{\frac{2}{m_e}} \int_{\text{Atm.}} \int_0^{\hat{E}} \sqrt{E} \; F(\underline{r}, E) \; e^{-\tau(\underline{r}, 130.4\text{nm})} \\
& \times [n_{n,1}(\underline{r}) \; \sigma_{130.4,1}(E) + n_{n,3}(\underline{r}) \; \sigma_{130.4,3}(E)] \; \mathrm{d}E \; \mathrm{d}V \; ,
\end{aligned}
\tag{6.33}
$$

$$
\begin{aligned}
I_{135.6} = {} & \frac{10^{-10}}{R_C^2 \pi} \sqrt{\frac{2}{m_e}} \int_{\text{Atm.}} \int_0^{\hat{E}} \sqrt{E} \; F(\underline{r}, E) \; e^{-\tau(\underline{r}, 135.6\text{nm})} \\
& \times \; n_{n,1}(\underline{r}) \; \sigma_{135.6,1}(E) \; \mathrm{d}E \; \mathrm{d}V \; ,
\end{aligned}
\tag{6.34}
$$

$$
\begin{aligned}
I_{121.6} = {} & \frac{10^{-10}}{R_C^2 \pi} \sqrt{\frac{2}{m_e}} \int_{\text{Atm.}} \int_0^{\hat{E}} \sqrt{E} \; F(\underline{r}, E) \; e^{-\tau(\underline{r}, 121.6\text{nm})} \\
& \times \; n_{n,3}(\underline{r}) \; \sigma_{121.6,3}(E) \; \mathrm{d}E \; \mathrm{d}V \; .
\end{aligned}
\tag{6.35}
$$

In these expressions, $R_C = 2410$ km is Callisto's radius, $\sigma_{130.4,1}$ and $\sigma_{135.6,1}$ are the cross sections of electron impact dissociative excitation of O_2 associated with the photon emission at 130.4 nm and 135.6 nm taken from Kanik et al. (2003) and $\sigma_{121.6,3}$ and $\sigma_{130.4,3}$ are the cross sections of electron impact dissociative excitation of H_2O associated with the photon emission at 121.6 nm (Lyman-α) and 130.4 nm taken from Makarov et al. (2004). We neglect the contribution of H_2O to the OI $\lambda 135.6$ nm emission line since associated cross sections are comparably small (Makarov et al., 2004). We account for atmospheric re-absorption of the UV emission by the term $exp\{-\tau(\underline{r}, \lambda)\}$ where we have approximated the Callisto-HST line by the Callisto-Sun line (only for the purpose of calculating re-absorption). Re-absorption is expected to weaken Callisto's atmospheric UV emission intensities by $\sim$5% (Cunningham et al., 2015). Note that OI emission line cross sections are non-zero for electron energies larger than approximately 14 eV. This threshold shows that the UV emission intensity can only be generated by the high-energy part of the electron energy distribution function ($\sim$14 eV - 100 eV).

6.4 Results of the ionosphere model

In this section, we present calculated electron energy distribution functions $F(E)$, related electron densities n_e and temperatures T_e as well as atmospheric UV emission intensities, e.g, $I_{135.6}$. Further, we compare calculated radio occultation LOS

electron column densities and disk averaged UV emissions with the observations of Kliore et al. (2002) and Cunningham et al. (2015).

6.4.1 Structure of Callisto's day-side ionosphere

We start with a discussion of calculated electron energy distribution functions including the Maxwellian part and show the spatial distribution of calculated electron densities and electron temperatures.

6.4.1.1 Electron energy distribution function

We find that the electron energy distribution function and the associated electron density and temperature significantly depend on the relative amount of H_2O in a given volume element of the atmosphere. Therefore, we present two exemplary electron energy distribution functions, one of a volume element without H_2O and one of a volume element with H_2O.

Electron energy distribution function without H_2O: Figure 6.5 shows an exemplary electron energy distribution function of a volume element without any H_2O molecules. We find that distribution function characteristics will be fairly similar as in this presented case, if the relative amount of H_2O is smaller than 4%. The blue line shows the Maxwellian distribution of thermal electrons and the red line shows the distribution of suprathermal electrons. The dashed black line marks the transition energy E_t where the thermal and the suprathermal electron energy distribution functions have equal intensities. In this case, the transition energy is 0.38 eV, the electron density of the thermal electrons is 2.1×10^{10} m^{-3} and the electron temperature is 361 K. Note that regarding later presented modeling results the transition energy has been set to 1 eV since a variation of E_t within the range of 0.1 eV to 5 eV does not cause a significant change of the resulting electron density, electron temperature or UV emission intensity (see Appendix B and Hoegy (1984)).

Figure 6.5 also shows that the suprathermal electron energy distribution exhibits spikes with variations up to three orders of magnitude between several adjacent energy bins. These spikes result from the fact that the applied electron degradation scheme contains discrete production and loss processes. The effective electron production is dominated by the initial production from photoionization (see
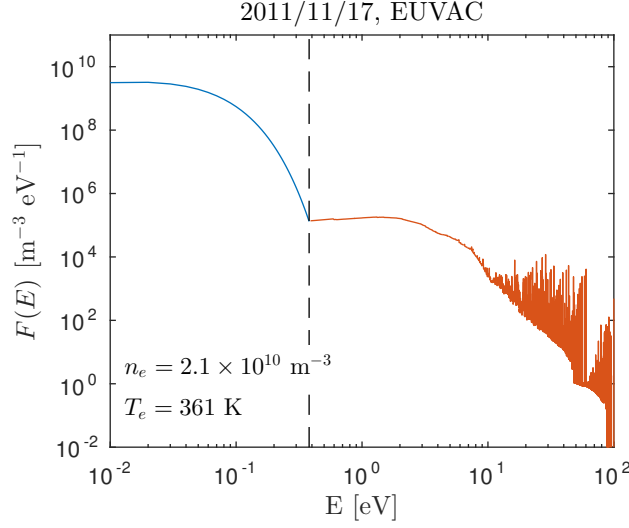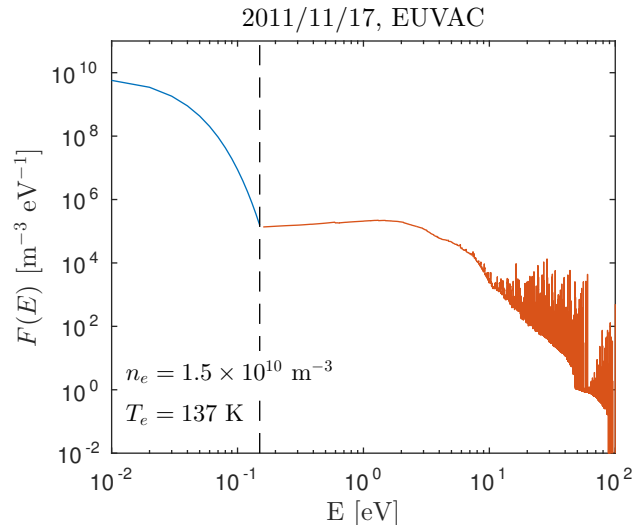
Figure 6.5: Calculated electron energy distribution function of a volume element **without** H_2O resulting from solving Equations (6.1)-(6.5). The prescribed neutral densities are: O_2 density $n_{n,1} = 1.0 \times 10^{15}$ m^{-3}, CO_2 density $n_{n,2} = 0.33 \times 10^{15}$ m^{-3}. Resulting electron density and temperature are $n_e = 2.1 \times 10^{10}$ m^{-3} and $T_e = 361$ K. The dashed black line marks the transition energy E_t, here: $E_t = 0.38$ eV.

also Figure 6.3). Therefore, the spikes of the calculated discrete photoelectron spectrum directly cause spike structures of the suprathermal electron energy distribution function. For energies smaller than 10 eV, the continuous energy loss due to electron-electron collisions becomes dominant causing a smoothing of the suprathermal distribution function.

Electron energy distribution function with H_2O: Figure 6.6 shows an exemplary distribution function for a relative H_2O abundance of 5%. In comparison to the volume element without H_2O presented above, the electron temperature is decreased by a factor of ~0.4 to 137 K, the transition energy is decreased to 0.15 eV and the electron density is decreased by a factor of ~0.7 to 1.5×10^{10} m^{-3}. Note again that increasing the transition energy artificially in this case to 1 eV would not significantly change the resulting electron density and electron temperature.

The difference between electron temperatures for volume elements with and without H_2O is caused by the cooling mechanism of thermal electrons due to rotational state excitation of H_2O molecules. Cross sections and resulting reaction rates for rotational state excitation are about four orders of magnitude larger for H_2O than for O_2 or CO_2 since H_2O molecules possess a large permanent magnetic

Figure 6.6: Calculated electron energy distribution function of a volume element **with** a significant amount of H_2O resulting from solving Equations (6.1)-(6.5). The prescribed neutral densities are: O_2 density $n_{n,1} = 1.0 \times 10^{15}$ m^{-3}, CO_2 density $n_{n,2} = 0.33 \times 10^{15}$ m^{-3} and H_2O density $n_{n,3} = 0.05 \times 10^{15}$ m^{-3}. Resulting electron density and temperature are $n_e = 1.5 \times 10^{10}$ m^{-3} and $T_e = 137K$. Dashed black line marks the transition energy E_t.

dipole moment (e.g., Anzai et al., 2012; Demtröder et al., 2006). As a result, H_2O rotational cooling counteracts or even compensates the heating of thermal electrons from Coulomb collisions with suprathermal electrons. As a consequence of smaller electron temperatures, electrons within volume elements with H_2O recombine much faster and the resulting electrons to neutrals ratio is about 30% smaller than in volume elements without H_2O. This effect is anti-intuitive since we could expect an increase of electron density from adding more and more ionizable neutral particles to a volume element.

High energy part of the suprathermal electron energy distribution function: We find that the amplitudes of the distribution function's high energy part (> 10 eV) only weakly depend on the total neutral density n_n since both production and degradation loss increase linearly with the neutral density nearly negating each other. This behavior can be seen from Equation (B.2) in Appendix B. The total neutral density n_n will vanish in Equation (B.2) if we introduce relative neutral abundances $\zeta_s = n_{n,s}/n_n$ and neglect processes that are not dominant at energies larger than 10 eV, namely, recombinations with ions and electron-electron collisions.

However, the amplitudes of the suprathermal electron distribution function depend significantly on the relative composition, namely, on the parameters ζ_s as a result of the different ionization cross sections of O_2, CO_2 and H_2O. For instance, O_2 dominated volume elements show $\sim 10\%$ larger amplitudes than H_2O dominated ones and CO_2 dominated volume elements show $\sim 50\%$ larger amplitudes than H_2O dominated ones.

From Equation (6.33) - (6.35), we see that the atmospheric UV emission is sensitive to the amplitudes of the electron energy distribution function above 14 eV. Therefore, the atmospheric composition seems to play an important role for the atmospheric UV emission of Callisto as one would expect from figure 3 of Wedlund et al. (2011) by comparison of the mean energy expended in collisions of electrons with O_2 and CO_2 gases.

6.4.1.2 Electron density and temperature

Now, we show the spatial structure of the calculated electron densities for a spherically symmetric O_2 atmosphere and explain how the prescribed asymmetric H_2O distribution impacts the derived ionosphere.

Figure 6.7 and Figure 6.8 show calculated electron densities and electron temperatures of Callisto's ionosphere in the equatorial XY-plane for a spherically
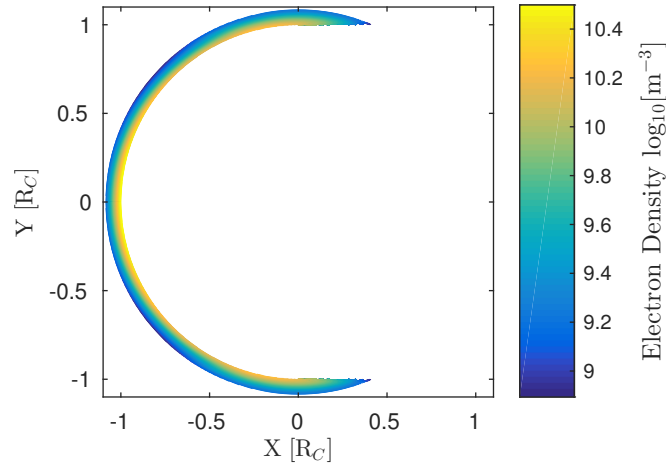
Figure 6.7: Ionospheric electron densities in the equatorial plane. The Sun is shining from the -X direction. The prescribed atmosphere consists of a spherically symmetric O_2 atmosphere with a column density of 3.0×10^{19} m^{-2}, the CO_2 column density is 0.80×10^{19} m^{-2} and the H_2O atmosphere is incorporated as described by Equation (5.4).
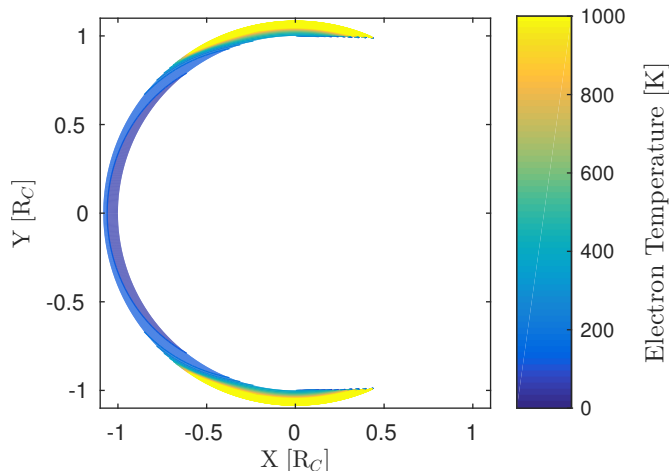
Figure 6.8: Ionospheric electron temperatures in the equatorial plane. The atmospheric configuration is the same as in Figure 6.7. The temperature range is limited to 0-1000 K in order to illustrate temperature variations at lower altitudes which are relevant for the model results. Electron temperatures exceed 1000 K reaching maximum values of $\sim$3000 K at higher altitudes in the terminator region.

symmetric and optically thin O_2 atmosphere with $N_{O2}^{min} = N_{O2}^{max} = 3.0 \times 10^{19}$ m^{-2}. For a fixed altitude, electron densities have a maximum at the subsolar point and first decrease with an increasing subsolar angle β reaching a minimum at $\beta \approx 55°$. For larger subsolar angles, electron densities increase again and finally decrease to zero behind the terminator on the night side. The ionosphere also extents to the positive X hemisphere at higher altitudes where the line between atmosphere and Sun does not intersect Callisto. Note that calculated electron temperatures only weakly vary with varying prescribed O_2 densities. In the terminator region, electron temperature are between 120 K and 1000 K within an altitude range of 60 km and increases up to $\sim$3000 K at 200 km. In the subsolar region, electron temperatures are between 120 K and 300 K within the investigated altitude range of 0-200 km.

The subsolar maximum and the electron density enhancement around the terminator result from the assumed asymmetric H_2O distribution. For $\beta \lesssim 55°$, the relative H_2O abundance is sufficiently large that H_2O rotational state excitations cool down the thermal electrons to temperatures close to the assumed neutral temperature of 120 K (see Figure 6.8). For $\beta \gtrsim 55°$, the relative H_2O abundance becomes sufficiently small so that H_2O rotational cooling is no longer that effective. As a result, the electron temperature increases, the recombination rate decreases

and the electron density increases.

Figure 6.9 shows radial electron column densities as a function of the subsolar angle β for both an atmosphere with the assumed H_2O distribution and without any H_2O at all. For $\beta \gtrsim 25°$, the increase of loss rates due to the inclusion of H_2O starts to dominate over the increase of electron production due to the inclusion of H_2O. In comparison to an atmosphere without H_2O, the inclusion of H_2O as an additional atmospheric species leads to an approximately 12% smaller mean electron column density.

For the purpose of future modeling studies of Callisto's plasma environment and interpretations of observations, we derive the following approximated linear relation between the mean electron column density $\bar{N}_e$ and the O_2 column density N_{O2} of Callisto's atmosphere in case of a spherically symmetric O_2 distribution including H_2O

$$\bar{N}_e = 5.1 \times 10^{11} \text{ m}^{-2} + 4.0 \times 10^{-9} N_{O2} \quad \text{for } N_{O2} < 3 \times 10^{20} \text{ m}^{-2} . \quad (6.36)$$

The first term on the left hand side of Equation (6.36) represents the mean electron column density originating from the water vapor pressure correlated
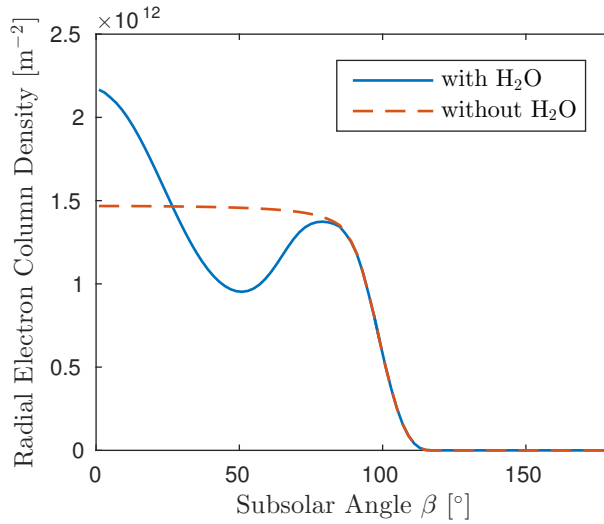
Figure 6.9: Radial electron column densities as a function of the subsolar angle β for an atmosphere including H_2O (blue solid line) and without H_2O (red dashed line). For the blue model, the H_2O density distribution follows the water vapor pressure distribution as described by Equation (5.4). For both models, the O_2 column densities are $N_{O2}^{max} = N_{O2}^{min} = 3.0 \times 10^{19}$ m^{-2} and the CO_2 column density is set to $N_{CO2} = 0.8 \times 10^{19}$ m^{-2}.

H_2O density distribution and the spherically symmetric CO_2 atmosphere with $N_{CO2} = 0.8 \times 10^{19}$ m^{-2}. Note that the above fit is valid for a medium solar activity level comparable to the activity level during C-20, C-22, C-23 and the HST/COS observation from November 17, 2011.

6.4.2 Density and structure of atmospheric O_2

First, we perform a comparison of model results with radio occultation results before we move on to a comparison of model results with HST observations and end up with a joint comparison.

6.4.2.1 O_2 density from comparing model results with Galileo radio occultation observations

In order to compare model results to radio occultation results, we extract LOS electron column densities (N_{LOS}^e according to Equation 6.32) of the flybys C-9, C-20, C-22 and C-23 and associated observational errors from the radio occultation results of Kliore et al. (2002). For entries and exits of all flybys, Figure 6.10 shows these radio occultation LOS electron column densities as black circles including error bars located at four LOS closest approach altitudes z_{int} (0, 25, 50, and 75 km). In each panel of Figure 6.10, colored lines mark the corresponding LOS electron column densities derived from our ionosphere model. Each color is assigned to a certain prescribed atmospheric O_2 column density shown in the color scale on the right side of Figure 6.10. Here, the O_2 atmosphere is assumed to be spherically symmetric, i.e., $N_{O2}^{min} = N_{O2}^{max}$.

Our model calculations show that the discrepancy between entry and exit observations seen during the flybys C-22 and C-23 can be explained by a photoionization driven ionosphere as suggested by Cunningham et al. (2015). For the flybys C-20, C-22 and C-23, the entry tangential points are located slightly on the day side and the exit tangential points are located slightly on the night side. Therefore, the difference between entry and exit LOS electron column densities is a consequence of the photoionization driven asymmetric ionosphere around the terminator as also well visible in Figure 6.4 for flyby C-22.

While the observations show LOS electron column density peaks above Callisto's surface, the model results do not show such structures in the range of observed
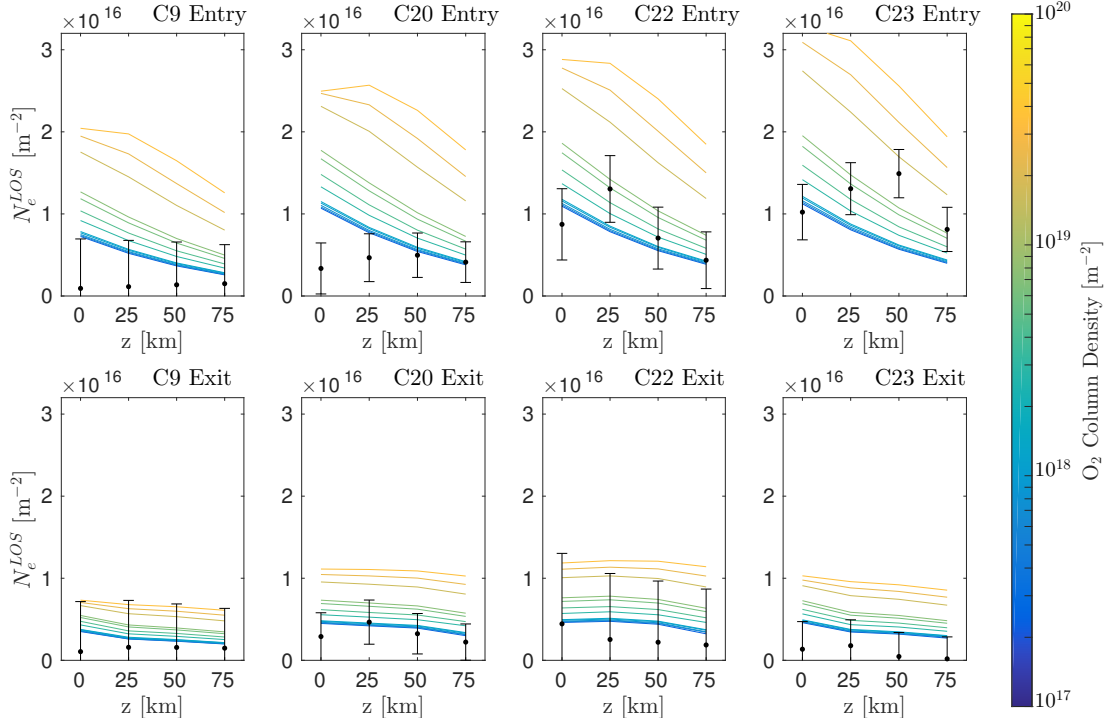
Figure 6.10: Calculated and observed radio occultation LOS electron column densities of different closest approach altitudes. The prescribed CO_2 atmosphere is spherically symmetric with $N_{CO2} = 0.8 \times 10^{19}$ m^{-2} and H_2O is distributed as described by Equation (5.4). Black circles with error bars represent radio occultation results extracted from Kliore et al. (2002), colored lines represent model results for spherically symmetric O_2 atmospheres with different column densities according to the color scale.

electron column density values. Strong peaks above Callisto's surface can be seen in the observational results of the entries of C-22 and C-23 in Figure 6.10 at $z_{int} = 25$ km and $z_{int} = 50$ km. For O_2 column densities up to 10^{21} m^{-2}, model results show that a photoionization driven ionosphere does not possess comparable peak structures. Therefore, our results demonstrate that the observed peak structures are not caused by the combination of photoionization and an optically thick atmosphere as expected by Kliore et al. (2002). We will discuss this issue in more detail in Section 6.5.3. Note that the observational error ranges of the associated LOS electron column densities are relatively large with relative errors of 15%-40%. Although our model does not reveal the observed peak structure, some atmosphere setups fit to the full set of observations within a 1σ error range as we will discuss in the following.

The calculated LOS electron column densities are not heavily affected by possible

subsolar-terminator asymmetries of the O_2 atmosphere and depend basically on the O_2 column density at the terminator $N_{O2}^{\min}$. In order to determine the terminator O_2 column density quantitatively from a comparison of model results with radio occultation observations, we introduce a formal unbiased measure: the reduced Chi-Square parameter χ_{red}^2 quantifying the goodness of fit between model results and observations. In case of $\chi_{red}^2 \approx 1$, the deviation of the model prediction is in the same range as the observational error - the 1σ range. Atmosphere models with $\chi_{red}^2 > 1$ imply inadequate fits between model and observations, while atmosphere models with $\chi_{red}^2 \leq 1$ formally fit the observations within the error bars.

Assuming that the atmospheric density does not significantly vary at the terminator between different flybys, we derive that χ_{red}^2 will be smaller than one if N_{O2}^{min} is smaller than 0.40×10^{19} m^{-2}. We interpret this O_2 column density as an upper bound of the terminator O_2 column density. Note that this upper bound depends on the prescribed density of the CO_2 atmosphere. For smaller prescribed CO_2 column densities, the upper bound increases. In analogy to Figure 6.10, Figure 6.11 shows the radio occultation LOS electron column densities for a prescribed CO_2 column density of $N_{CO2} = 0.32 \times 10^{19}$ m^{-2}, which is the lower bound of the observational error range of Carlson (1999) (see Section 3.1.1). In this case, χ_{red}^2 will be smaller than one if N_{O2}^{min} is smaller than 1.0×10^{19} m^{-2}. We do not present results for CO_2 column densities that are larger than the mean value ($N_{CO2} = 0.80 \times 10^{19}$ m^{-2}) given by Carlson (1999) since in this case the upper bound will become even smaller. Therefore, the maximum terminator O_2 column density is $0.4^{+0.6} \times 10^{19}$ m^{-2} according to χ_{red}^2 and considering the uncertainties of the CO_2 column density.

Note that according to the χ_{red}^2 criteria, a pure CO_2 atmosphere with a column density of $N_{CO2} = 0.80 \times 10^{19}$ m^{-2} at the terminator also explains the radio occultation observations. Therefore, only based on the radio occultation observations, we cannot rule out an atmosphere with a dominant CO_2 abundance at the terminator but a sufficient subsolar O_2 abundance satisfying the HST/COS observations (see Section 6.4.2.2) but low enough O_2 densities in the terminator region not affecting electron densities.

Although the fitting parameter analysis indicates a reasonable fit of model results and observations, a visual inspection of Figure 6.10 and Figure 6.11 still reveal some misfits. The peak structures during C-22 and C-23 and the outstanding
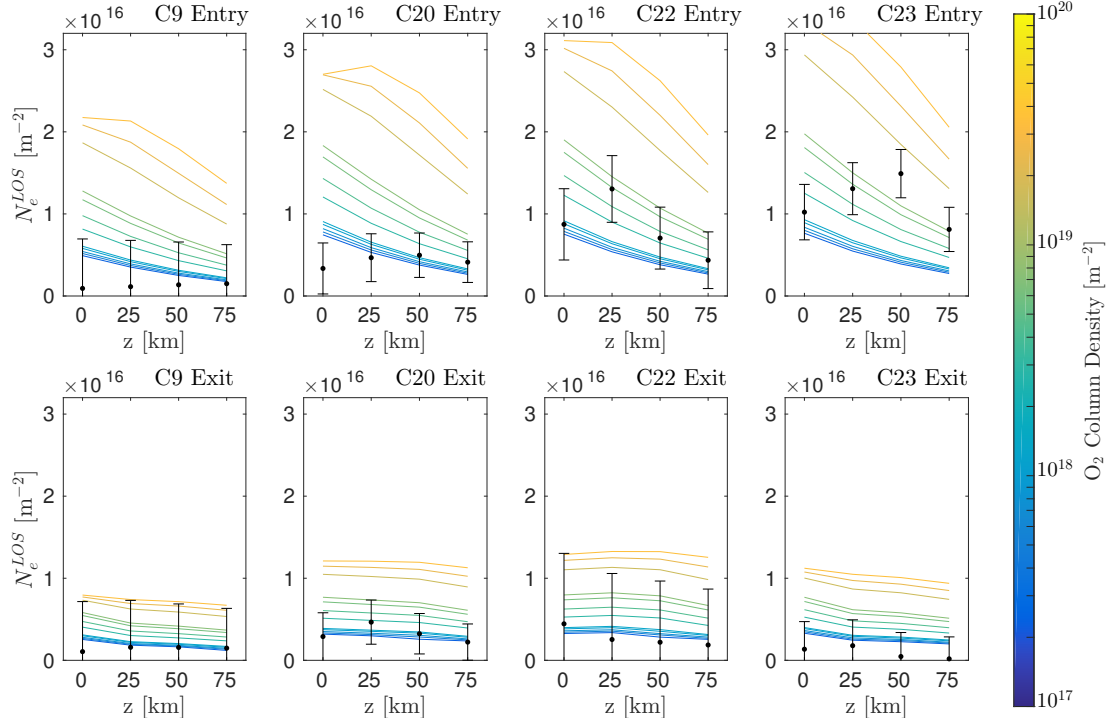
Figure 6.11: Calculated and observed radio occultation LOS electron column densities of different closest approach altitudes as in Figure 6.10. The CO_2 column density is set to $N_{CO2} = 0.32 \times 10^{19}$ m^{-2} and the H_2O column density is distributed as described by Equation (5.4).

low ionospheric signal during C-9 might indicate that the atmosphere-ionosphere system possess dynamics which we do not cover with our model. In this regard, electron transport and atmospheric dynamics might play an important role, which might provide an explanation of these differences. These questions will be discussed in more detail in Section 6.5.

6.4.2.2 O_2 density from comparing model results with Hubble Space Telescope observations

For spherically symmetric O_2 atmospheres, the comparison between model results and HST/COS observations from Cunningham et al. (2015) yields an O_2 column density of $N_{O2} = 2.1^{+1.1}_{-1.1} \times 10^{19}$ m^{-2} on the basis of the OI λ135.6 nm emission (see Figure 6.12). This O_2 column density is 2-5 times larger than the maximum O_2 column density of $0.4^{+0.6} \times 10^{19}$ m^{-2} that we have derived from radio occultation observations. As we will discuss in Section 6.4.2.3, an atmospheric O_2
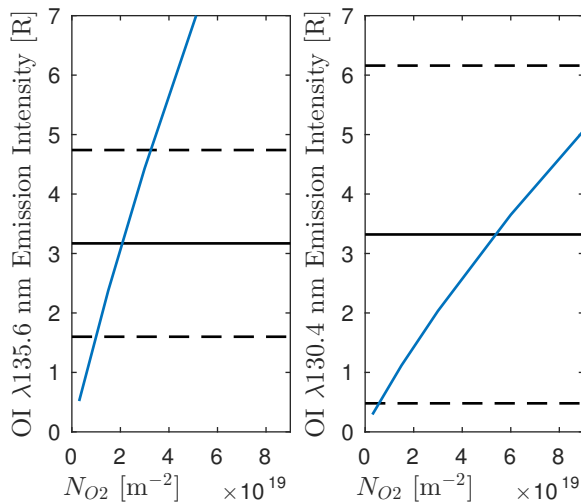
Figure 6.12: Comparison of modeled atmospheric UV emission intensities for OI λ135.6 nm (left panel) and OI λ130.4 nm (right panel) with observational constraints of Cunningham et al. (2015) as a function of O_2 column density assuming spherical symmetry of the atmosphere. Solid blue lines represent the model outcome, solid black lines mark the measured values by Cunningham et al. (2015), dashed lines mark the associated observational error range.

density gradient between subsolar and terminator region can possibly explain this difference. Note that the derived O_2 column densities correspond to an optically thin atmosphere.

The relation between the OI emission intensities and the O_2 column density is approximately linear. The linear behavior shown in Figure 6.12 also shows that the upper part of the suprathermal electron energy distribution function is to some extend nearly independent of the total neutral density, at least for $N_{O2} < 3 \times 10^{20}$ m^{-2}. For larger O_2 column densities outside the range shown in Figure 6.12, the characteristic of the derived OI λ135.6 nm emission experience a saturation effect, which is due to the effect of optical depth. We extract the following fit between the O_2 column density and the brightness of the disk averaged OI λ135.6 nm emission from Callisto's atmosphere for the purpose of future modeling work and interpretations of observations:

$$I_{135.6} = 1.51 \times 10^{-19} \text{ R m}^2 \ N_{O2} \quad \text{for } N_{O2} < 3 \times 10^{20} \text{ m}^{-2} \ . \tag{6.37}$$

Note that this fit is valid for solar conditions similar to those prevailing on November 17, 2011, the day of the HST/COS observation. The associated
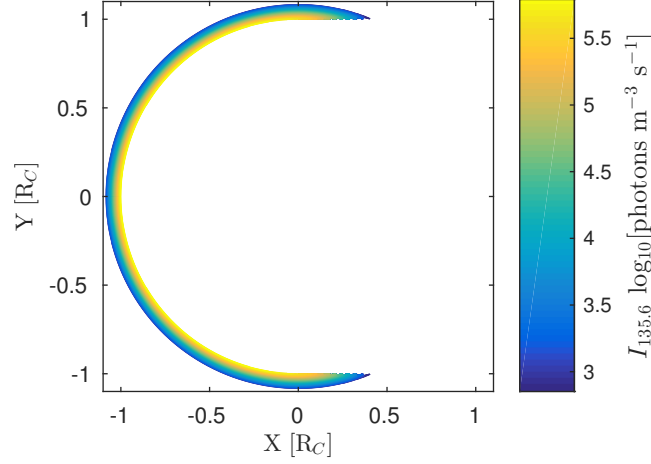
Figure 6.13: OI $\lambda 135.6$ nm emission intensity distribution in the equatorial plane. The Sun is shining from the -X direction. The prescribed atmosphere consists of a spherically symmetric O_2 atmosphere with a column density of 3.0×10^{19} m^{-2}, the CO_2 column density is 0.80×10^{19} m^{-2} and the H_2O atmosphere is incorporated as described by Equation (5.4).

prescribed atmosphere also includes CO_2 with $N_{CO2} = 0.8 \times 10^{19}$ m^{-2} and H_2O is distributed as described by Equation (5.4).

The spatial structure of the local UV emission intensity is shown in Figure 6.13 for the OI $\lambda 135.6$ nm emission line. As a consequence of the linear dependence on the O_2 density, the atmospheric OI $\lambda 135.6$ nm emission intensities decrease nearly exponentially with increasing altitude and have their maximum at the surface except at the night side. In the subsolar region, the OI $\lambda 135.6$ nm emission intensity is slightly weakened due to the large subsolar H_2O column densities, which cause relatively large optical depths and roughly 10% smaller amplitudes of the electron energy distribution function at energies above 10 eV.

In analogy to the formulation in Cunningham et al. (2015), we calculate the relation between the rate of electron-ion pair production and the emission of one OI $\lambda 135.6$ nm photon. We find that this ratio is variable and decreases with increasing O_2 column densities as shown in Figure 6.14, where we set the numbers of electron-ion pairs in relation to the relative amount of atmospheric O_2. The variation in this ratio is caused by the relative abundances of species, the total atmospheric abundance, and the fractional partitioning of solar EUV radiation into OI $\lambda 135.6$ nm emission. For the derived O_2 column density of 2.1×10^{19} m^{-2}, there is one emitted OI $\lambda 135.6$ nm photon per every 60 electron-ion
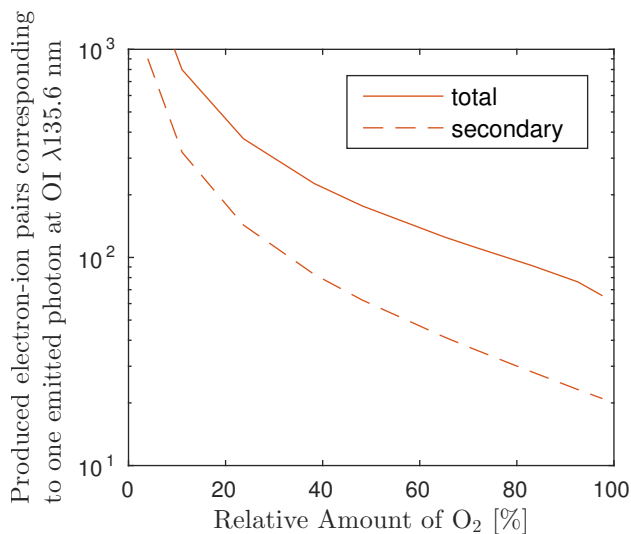
Figure 6.14: Ratio between production rates of electron-ion pairs and emission rate of OI $\lambda 135.6$ nm photons as a function of the relative atmospheric O_2 abundance. The solid red line shows the ratio considering the total production rate and the dashed red line shows the ratio considering only secondary electron impact ionization. The derived mean O_2 column density of 2.1×10^{19} m^{-2} corresponds to a relative abundance of $\sim$50%.

pair produced by secondary ionization or per every 170 electron-ion pair produced by photoionization including secondary ionization. For increasing O_2 column densities, these ratios converge to approximately one emitted OI $\lambda 135.6$ nm photon per every 22 electron-ion pair produced by secondary ionization or per every 65 electron-ion pair produced by photoionization including secondary ionization.

The OI $\lambda 130.4$ nm emission multiplet is only partially usable to constrain the O_2 abundance since an important contribution to the OI $\lambda 130.4$ nm emission might be produced from not only O_2, but also from O, CO_2, and H_2O. For all the latter species, the OI $\lambda 130.4$ nm emission is brighter than their OI $\lambda 135.6$ nm emission intensities. We have not considered O in our phenomenological atmosphere model in Chapter 5 since the density contribution of O is expected to be minor below an altitude of 100 km in comparison to O_2, CO_2 and H_2O (Liang et al., 2005). The calculated OI $\lambda 130.4$ nm emission originating from O_2 can be roughly approximated by $I_{130.4} \approx I_{135.6}/2$ as a result of the ratio between the associated electron dissociation excitation cross sections. For the derived range of N_{O2}, the observed OI $\lambda 130.4$ nm emission intensity agrees with our model results within the range of observational uncertainties. However, the uncertainties are relatively large and do not allow tight constraints on the atmospheric column densities of O_2

and O. If we neglect the uncertainties of the HST/COS observations, the observed ratio between OI λ135.6 nm and OI λ130.4 nm emissions will be approximately 1:1. An additional abundance of O with a relative abundance of 5%-10% of the O_2 abundance might explain this 1:1 ratio. Note that this is a very rough estimation based on the ratios between OI λ130.4 nm and OI λ135.6 nm emission intensities of pure molecular and pure atomic oxygen taken from Cunningham et al. (2015): $I^{O2}_{130.4}/I^{O2}_{135.6} \approx 0.5$ and $I^{O}_{130.4}/I^{O}_{135.6} \approx 8.0$ including an averaged approximation of the non-linear resonance scattering effect for atomic oxygen.

We derive a disk averaged HI λ121.6 nm emission intensity below 1 R. Unfortunately, the Lyman-alpha emission from Callisto's atmosphere cannot easily be extracted from the observations since the observed Lyman-α intensity is dominated by the reflected sunlight from Callisto's surface. Therefore, there is no available data which can be compared to our model results.

It is remarkable that incorporating CO_2 and H_2O into our model reduces the resulting UV emission intensity of the atmospheric O_2 part by approximately 20%. This effect results from the impact of different neutral species on the upper energy regime of the electron energy distribution function. The electron energy distribution function is about 10% smaller in the upper energy regime for volume elements where H_2O is the dominant species, specially in the subsolar region. Since the composition of different species determines the ratio between production rate and degradation rate in the upper energy part, it plays an important role regarding the UV emission intensity.

6.4.2.3 Atmospheric asymmetry from a joint comparison

As mentioned in Chapter 5, a day-night asymmetry of Callisto's O_2 atmosphere might be driven by the surface ice temperature dependency of the atmospheric production processes surface sputtering and sublimation. Our parametrized O_2 atmosphere model allows for an independent variation of the subsolar O_2 column density N^{max}_{O2} and the terminator O_2 column density N^{min}_{O2}. The assumed O_2 column density distribution of the sunlit hemisphere follows a cosine law as shown in Figure 5.1.

The comparison of radio occultation results with model results shows that the radio occultation LOS electron column densities depend basically on the terminator O_2 column density N^{min}_{O2} and depend only weakly on the subsolar
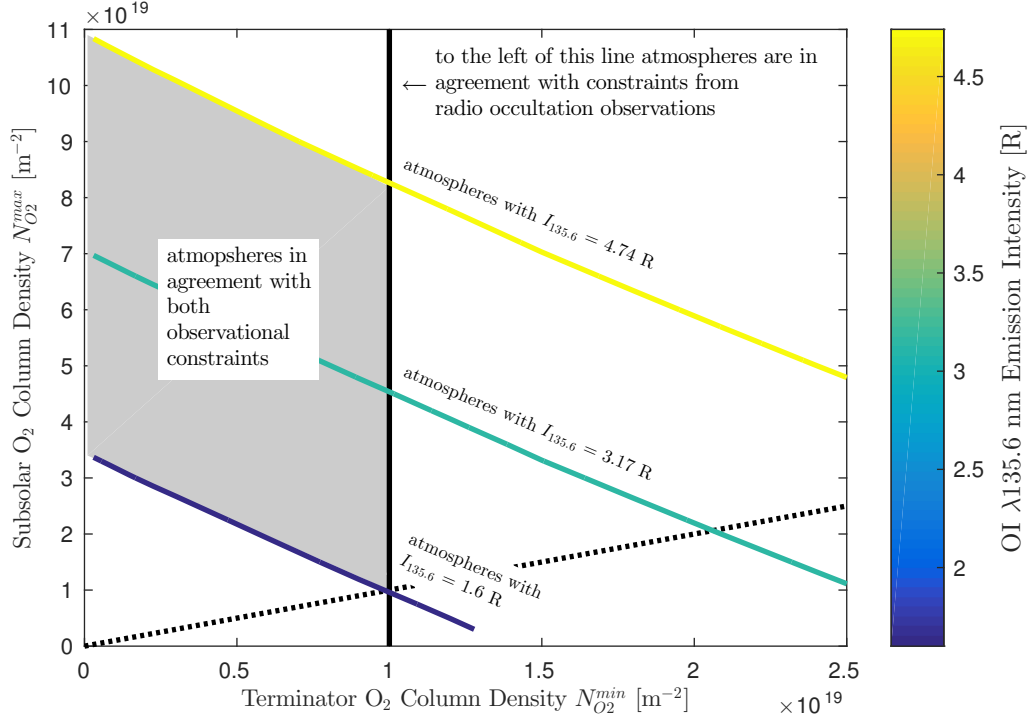
Figure 6.15: Comparison of modeled atmospheric UV emission intensities with observational constraints of Cunningham et al. (2015) and Kliore et al. (2002). The prescribed asymmetric atmosphere is a function of two model parameters: the terminator O_2 column density N_{O2}^{min} (x-axis) and the subsolar O_2 column density N_{O2}^{max} (y-axis). The blue-green line identifies atmospheric configurations for which our model predicts UV emission intensities equal to the observational results of Cunningham et al. (2015), dark-blue and yellow lines show the corresponding lower and upper error range. The black solid line marks the upper bound of the terminator O_2 column density derived by the analysis of radio occultation observations with respect to all flybys and assuming the minimum CO_2 column density of 0.32×10^{19} m^{-2}. The dotted black line marks cases of spherically symmetric O_2 atmospheres. The gray area is the derived parameter space of N_{O2}^{min} and N_{O2}^{max} that agrees with both observational constraints with respect to the observational uncertainties.

O_2 column density $N_{O2}^{\max}$. Therefore, we already know from the comparison of model results for spherically symmetric O_2 atmospheres with radio occultation observations (see Section 6.4.2.1) that the terminator O_2 column densities $N_{O2}^{\min}$ need to be smaller than $0.4^{+0.6} \times 10^{19}$ m^{-2}, also for the case of an asymmetric O_2 atmosphere.

According to this terminator O_2 column density range, we derive a possible subsolar O_2 column density range by comparing model results with the HST/COS observation of the disk averaged OI λ135.6 nm emission intensity. As a blue-green

line, Figure 6.15 shows all combinations of $N_{O2}^{\min}$ and $N_{O2}^{\max}$ which generate the observed intensity of 3.17 R according to Cunningham et al. (2015). Note that the scaling differs between the axes of $N_{O2}^{\min}$ and $N_{O2}^{\max}$. The dark-blue and yellow lines mark the characteristics according to the lower and upper error boundaries of the HST/COS observation. The solid black line marks the derived upper bound of the terminator O_2 column density $N_{O2}^{\min}$ from the comparison between model results and radio occultation observations. The gray area marks the possible combinations of $N_{O2}^{\min}$ and $N_{O2}^{\max}$ with respect to both the radio occultation observations of Kliore et al. (2002) and the HST/COS observation of Cunningham et al. (2015).

The model-observation comparison in Figure 6.15 implies that Callisto's atmosphere possesses very likely a day-night asymmetry. The prescribed O_2 atmosphere needs to be asymmetric with $N_{O2}^{\max} > N_{O2}^{\min}$ in order to explain HST/COS observations and radio occultation observations simultaneously. Only if both error bars on the observational constraints are included, we will find a single combination for which no asymmetry is required, namely, $N_{O2}^{\min} = N_{O2}^{\max} = 1.0 \times 10^{19}$ m^{-2}.

In order to estimate the asymmetry factor F_{as} of the O_2 atmosphere quantitatively using Equation (5.2), we assume a CO_2 column density of 0.80×10^{19} m^{-2} and, hence, a terminator O_2 column density of 0.4×10^{19} m^{-2} according to the comparison of model results and radio occultation observation (see Section 6.4.2.1). For $N_{O2}^{min} = 0.4 \times 10^{19}$ m^{-2}, we then calculate the possible range of N_{O2}^{max}. As a result, an asymmetry factor of $F_{as} = 15_{-9}^{+9}$ explains both observational constraints, where the error corresponds to the observational error range of the HST/COS observation. The associated subsolar O_2 column densities are in the range of $2.4 - 9.8 \times 10^{19}$ m^{-2}.

Note that the derived asymmetry factor is very sensitive to the assumed terminator CO_2 column density. A larger terminator CO_2 density requires less O_2 at the terminator to explain the observed electron densities. This implies a stronger day-night asymmetry of the O_2 atmosphere, while terminator CO_2 densities smaller than the assumed value of 0.80×10^{19} m^{-2} lead to smaller O_2 asymmetries.

6.5 Discussion of the ionosphere model results

We have developed a three dimensional model of Callisto's photoionization driven ionosphere, which simultaneously calculates the spatial distribution of electron densities and atmospheric UV emission intensities from electron energy distribution functions. The model includes photoionization, secondary ionization, electron-electron collisions and the energetically important collisions of electrons with neutrals and ions. The model is simplified as it does not consider electron and ion transport processes and does not describe the night side ionosphere.

A comparison between model results and the HST/COS observations of Cunningham et al. (2015) implies an average O_2 column density of $2.1^{+1.1}_{-1.1} \times 10^{19}$ m^{-2}. This value is about one order of magnitude smaller than the O_2 column density that was initially suggested by Kliore et al. (2002). However, our result is in fair agreement with the result of Cunningham et al. (2015), who derived an O_2 column density of $3.4^{+2.0}_{-1.8} \times 10^{19}$ m^{-2} from their HST/COS observations using a simpler model. Further, a joint comparison of radio occultation and HST/COS observations with our model results indicates a subsolar-terminator asymmetric O_2 atmosphere. We are able to explain HST/COS observations and radio occultation observations simultaneously by prescribing a 15^{+9}_{-9} times larger O_2 column density at the subsolar point than at the terminator.

In order to evaluate the significance of our findings, the following questions need to be addressed:

1. How can the local approximation, i.e., the neglect of electron and ion transport affect the ionospheric structure and change the interpretation regarding the atmospheric structure?

2. We assumed a constant and homogeneous scale height of 30 km for all atmospheric species. How will our model results be affected, if we assume the extreme case of decoupled scale heights for different species?

3. We neglect neutral winds which might be caused by the H_2O and O_2 density gradients between day and night side. What wind speeds are expected and how would a wind driven atmospheric redistribution affect our model results?

4. Our model cannot explain LOS electron column density peaks at higher altitudes. What are the reasons for this?

5. Are there hints for atmospheric variations with respect to the orbital phase as predicted for Europa by Plainaki et al. (2013) or due to variable rates of impinging magnetospheric ions?

In the following, we individually discuss the questions raised above.

6.5.1 The local approximation

Our ionosphere model is based on the assumption that collisions of electrons with particles dominate over electron transport processes within Callisto's ionosphere. Now, in order to evaluate this assumption, we compare electron collision time scales and electron transport time scales.

We estimate the average collision time between electrons and neutrals by the mean flight time between two collisions:

$$\tau_{\text{coll}}(\underline{r}, E) = \left(v_{\text{e}}(E) \; n_n(\underline{r}) \; \sigma_{tot}(E) \right)^{-1}, \tag{6.38}$$

where v_{e} is the electron velocity, $n_n(\underline{r})$ the total neutral density at the location $\underline{r}$, and σ_{tot} the effective total cross section between electrons and the neutrals O_2, CO_2 and H_2O depending on the electron energy and the chemical composition of a volume element. For this discussion, we consider volume elements with the chemical composition of 50% O_2, 25% CO_2 and 25% H_2O according to the relations of the derived atmosphere. The electron velocity is approximated by the kinetic velocity $v_{\text{e}}(E) \approx \sqrt{2E/m_e}$. Regarding suprathermal electron collision time scales, Equation (6.38) is evaluated for a broad set of electron energies: 0.1 eV, 1 eV, 10 eV, 50 eV. Regarding thermal electron collision time scales, Equation (6.38) is evaluated using an energy of 0.1 eV, which corresponds to an electron temperature of 774 K.

To assess the role of ionospheric transport for the electron densities and UV emissions, we examine the time scales during which electrons are transported from the ionosphere out into the Jovian magnetosphere. In detail, transport time scales τ_{trans} are approximated by the ratio of appropriate length scales and the effective electron velocity. Transport time scales of suprathermal electrons are

approximated by the ratio of Callisto's atmospheric scale height ($H \approx 30$ km) to the kinetic electron velocity v_e: $\tau_{trans}^{sup} \approx H/\sqrt{2E/m_e}$. For thermal electron transport time scales, we consider collective plasma effects. Here, a distinction needs to be drawn between thermal electron transport along and perpendicular to the Jovian magnetic field. However, we will show that both transport time scales are approximately equal.

The perpendicular transport time scale is driven by the advection of the Jovian magnetospheric plasma. The advection time can be approximated by the ratio of Callisto's atmospheric scale height ($H \approx 30$ km) to the effective bulk plasma velocity $v_{p,\mathrm{eff}}$ of the magnetospheric plasma near the satellite. Close to Callisto, the magnetospheric plasma is decelerated by a reduction factor α, which has been introduced by Saur et al. (2002). We use a conservative approximation of this reduction factor with $\alpha \approx 0.1$ in agreement with Strobel et al. (2002). Therefore, the perpendicular transport time scale is given by $\tau_\perp \approx H/v_{p,\mathrm{eff}} \approx 1.5$ s with $v_{p,\mathrm{eff}} \approx \alpha \, v_p$ and the plasma velocity $v_p \approx 192$ km s^{-1} taken from Kivelson et al. (2004).

The parallel transport time scale of the thermal population is approximated by a typical length scale of the atmosphere-ionosphere system, which is also the scale height $H \approx 30$ km, divided by the effective electron velocity parallel to the magnetic field. In principal, electrons can move freely parallel to the magnetic field, however, the electron motion is controlled by the ambient ions with one of the requirements being quasi-neutrality. Significant differences of electron and ion velocities generate ambipolar electric fields which tie electron and ion transport. Due to the large inertia of the ions, the effective parallel transport velocity is approximated by the mean ion velocity. Even though the ambipolar field accelerates the ions to some extend, the ions are mainly accelerated by the electric field induced by the magnetospheric plasma flow. For the perpendicular transport, a good approximation for newly generated ions is that they acquire a kinetic gyration velocity given by the local plasma velocity. The gyration velocity is initially perpendicular to the magnetic field. The resulting ion distribution function isotropizes subsequently. Therefore, a reasonable estimate for the parallel ion velocity is given by the local plasma velocity $v_{p,\mathrm{eff}} \approx \alpha \, v_p$. Thus, parallel and perpendicular transport times are similar, i.e., $\tau_{\mathrm{trans}}^{\mathrm{therm}} \approx \tau_\perp \approx \tau_\parallel \approx 1.5s$.

Figure 6.16 shows ratios of collision time scales and transport time scales

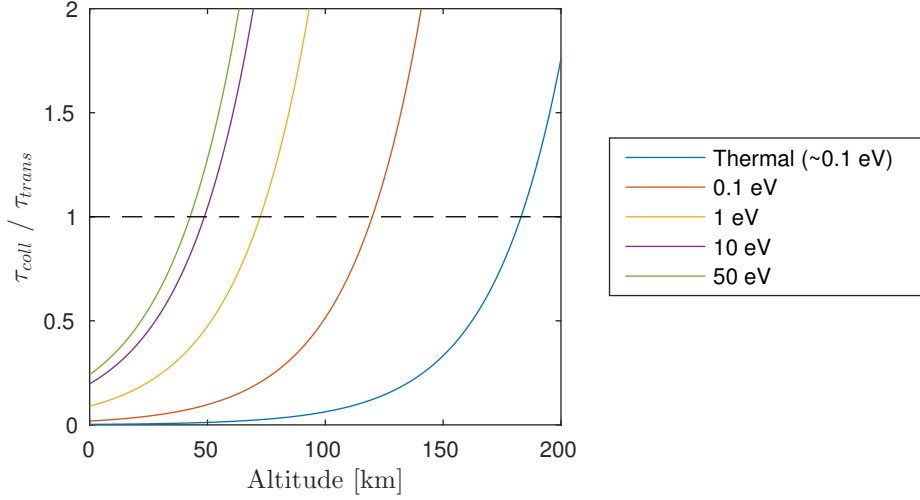**Figure 6.16:** Ratios between collision time scales and transport time scales $\tau_{\text{coll}}/\tau_{trans}$ as a function of altitude using the approach for thermal electrons (blue line) and the approach for suprathermal electrons (other lines). The black dashed line denotes the limit where the collision time scales equal transport time scales.

$\tau_{\text{coll}(\underline{r})}/\tau_{trans}$ for a neutral column density of $\sim3.5\times10^{19}$ m^{-2} and a neutral scale height of $H = 30$ km. We find that collisions dominate over transport up to an altitude of ~45 km for suprathermal electrons and up to 180 km for thermal electrons. For suprathermal electrons, we estimate the altitude limit of the local approximation conservatively for 50 eV electrons as the majority of photoelectrons ($\sim95\%$) is produced at energies smaller than 50 eV (see, e.g., Figure 6.3). As a consequence, electron transport can lead to a substantial loss of ionospheric electrons above an altitude of ~45 km. Therefore, derived O_2 column densities might be underestimated. Note that the atmospheric volume below the altitude of 45 km contains $\sim78\%$ of the total atmospheric mass. If we omit UV emissions and electron densities from above 45 km, our ionosphere model will require, therefore, 20%-30% larger O_2 column densities in order to meet the observational constraints from HST/COS and Galileo radio occultation observations.

The non-uniform nature of the transport effect could also play a role in shaping Callisto's ionosphere. After the deceleration of the magnetospheric plasma, the plasma is accelerated again when it is diverted around Callisto. Therefore, the plasma might reach peak velocities at the flanks of Callisto and minimum velocities above the upstream region. This difference can lead to an asymmetric distribution of the transport effect. However, a detailed discussion of these three dimensional

transport effects is out of the scope of this study.

6.5.2 Neutral winds

From our results, we expect a significant density gradient of Callisto's atmosphere between day and night side. Here, we estimate the resultant neutral wind speed v_n and sonic Mach number M_s. The lifetime of O_2 and CO_2 molecules is much longer than the lifetime of H_2O molecules, which have a sticking coefficient close to one. In contrast to O_2 and CO_2, the production and loss processes of H_2O are expected to be faster than the transport processes. Therefore, we focus on the estimation of velocities of O_2 and CO_2 molecules regarding neutral winds.

We estimate the sonic Mach number as follows: We assume a one dimensional mass density distribution $\rho(x)$ of an ideal isotherm gas where the equation of state is $p = \rho c_s^2$ with the atmospheric pressure p and the sonic speed $c_s = \sqrt{\gamma k_B T_n / m_n}$. Due to the assumption of an isothermal atmosphere, the polytropic exponent is set to $\gamma = 1$. Further, m_n represents the neutrals' mass. From the Navier-Stokes equation

$$\frac{1}{\rho}\frac{dp}{dx} = \frac{1}{2}\frac{d(v_n^2)}{dx} \tag{6.39}$$

we get the following conserved quantity:

$$v_n^2 + \frac{2}{\gamma}c_s^2 \log(\rho) = \text{cst} . \tag{6.40}$$

For a total O_2 and CO_2 mass density at the subsolar point ρ_{sub} and at the terminator ρ_{term}, the sonic Mach number M_s is then given by:

$$M_s^2 = \frac{2}{\gamma} \log\left(\frac{\rho_{sub}}{\rho_{term}}\right) . \tag{6.41}$$

For Callisto, we estimate that neutral winds will become supersonic if the O_2 asymmetry factor F_{as} is larger than $\sim$2.5. If the asymmetry factor decreases to 1.5, then wind speeds will be driven with Mach numbers of about 0.6. In contrast, our comparison between model results and observations discussed in Section 6.4.2.3 yields an asymmetry factor in the range of 6-24. The neutral winds tend to decrease atmospheric asymmetries generated by the atmospheric sources and sinks. Thus, the winds makes the lower values of our derived atmospheric

asymmetries more likely compared to the larger values.

Moreover, we identify three possible reasons why a more realistic atmospheric asymmetry factor might be smaller than the one derived by our study. First, if CO_2 column densities of the terminator region are smaller than the prescribed ones, the resulting asymmetry factor will be smaller, too, as already discussed in Section 6.4.2.3. Second, we derive the asymmetry factor from radio occultation observations of the terminator region and HST/COS observations of the day side. These observations did not occur at the same time, there is a time gap of more than one decade between the HST/COS and the radio occultation observations and there is also a two years time gap between the flybys C-9 and C-23. Therefore, unknown and non-considered changes of the neutral atmosphere with time might play a role in interpreting the observations of Callisto's atmosphere-ionosphere system. In this regard, we discuss the possible effect of an O_2 density orbital phase dependency in Section 6.5.4. Third, if sufficient H_2O molecules are transported to the terminator region despite their sticking coefficient close to one, electron densities will be smaller than predicted in the terminator region due to the electron cooling by rotational state excitation of H_2O. To meet the constraints of the radio occultation observations, the required O_2 terminator density would increase in this case. As a consequence, if we assume a redistribution of H_2O from the subsolar region to the terminator, our comparisons of model results and observations will yield a weaker atmospheric O_2 asymmetry.

6.5.3 The LOS electron column density peaks above the surface - a puzzle

For the flybys C-22 and C-23, Kliore et al. (2002) derived that the electron density n_e reaches a maximum above the surface. To invert the observed LOS electron column densities N_e^{LOS} obtained from the radio occultation technique into local electron densities n_e, Kliore et al. (2002) solved an Abel's integral equation assuming that the electron density distribution is spherically symmetric (see also sections 3.1.3 and 3.4). This implies that if the electron density n_e has a maximum above the surface, the LOS column density N_e^{LOS} needs to have a maximum above the surface, too.

An important aspect is that in all of the observations of Kliore et al. (2002) the radio LOS is approximately parallel to the solar ray path. If a spherically

symmetric neutral atmosphere falls of faster than $1/r$, the neutral LOS column density N_n^{LOS} will have its maximum for rays grazing the surface. But N_n^{LOS} is never maximum for a ray path at higher altitudes. If N_n^{LOS} is maximal for a ray path just grazing the surface, then the optical depth will be maximum for the ray path just grazing the surface, too. This implies that the total number of electrons produced by photoionization integrated along the solar ray path has its maximum for ray path just touching the surface. If we additionally assume that the recombination rate coefficient is spatially constant, the LOS electron column density will be maximum also along the ray paths just grazing the surface in agreement with our model outcome. Only for very large prescribed O_2 densities, the actual deviation between the solar ray path and the radio LOS causes electron column density peaks characteristics, which however misfit the observations (see, e.g, Figure 6.10). Thus, without transport of electrons, transport of electron energy (heat convection or heat conduction) and associated strongly inhomogeneous recombination rate coefficients, or multi-ion-chemistry effects, Callisto's peak electron density above the surface in Kliore et al. (2002) cannot be explained.

Note that Cunningham et al. (2015) and Liang et al. (2005) compared locally calculated electron density altitude profiles at the terminator with the electron density altitude profiles of Kliore et al. (2002) and found a good agreement of model and observation. However, Cunningham et al. (2015) and Liang et al. (2005) did not take into account that the profiles of Kliore et al. (2002) assume a spherically symmetric ionosphere while their models include asymmetries due to the effect of optical depth. If we extract comparable altitude profiles at the terminator from our model outcome, these profiles will show peaks above the surface, too, very similar to those of Cunningham et al. (2015) and Liang et al. (2005). However, we have to stress that we can only compare modeled and observed radio occultation LOS electron column densities with each other.

Electron transport and the moon-plasma interaction could play a role in creating LOS electron column density peaks above the surface as indicated by the results of Seufert (2012). The shape of the ionosphere might be modified by the interaction with the magnetospheric plasma. However, a detailed discussion of the effects of plasma dynamics is beyond the scope of this study.

6.5.4 Possible time-variability of Callisto's atmosphere

Based on the radio occultation results, there are two factors that possibly introduce a variation of the atmospheric density with time: the angle between sunlight and plasma flow as suggested by Kliore et al. (2002) and the magnitude of the magnetospheric plasma flux.

If the atmospheric density varies with the orbital phase, in particular between eastern and western elongation, similar to what Plainaki et al. (2013) derived for Europa, this could explain why there was only a very weak ionospheric signal during flyby C-9. Assuming perfect co-rotation of the Jovian magnetospheric plasma at Callisto's orbit, Callisto's upstream side was sunlit during C-20, C-22, C-23 at western elongation while the downstream side was sunlit during C-9 at eastern elongation. Plainaki et al. (2013) calculated that the O_2 atmosphere at Europa is expected to be approximately three times denser at western elongation than at eastern elongation due to the temperature dependence of sputtering efficiency. At western elongation, the majority of ambient energetic magnetospheric ions impinge on the sputtering efficient day side, while, at eastern elongation, only a minor portion of the energetic magnetospheric ions impinge on the sputtering efficient day side. If we apply these considerations to Callisto's atmosphere, the comparison of our model results with radio occultation results of C-9 will become more plausible. Figure 6.17 shows how the fitting between model results and radio occultation results will improve with respect to C-9 if the O_2 atmosphere is assumed to be three times denser during western elongation (C-20, C-22 and C-23) than during eastern elongation (C-9). The improved fit indicates that the low LOS electron column densities during C-9 are a result of the combination of smaller atmospheric densities and low solar activity (see Figure 6.2). These considerations also agree with the speculations of Kliore et al. (2002) that efficient sputtering accompanied by photoionization generates an ionosphere that is observable with radio occultation methods.

When Cunningham et al. (2015) observed UV emission from Callisto's atmosphere with HST/COS, Callisto was at about 15° east from the Sun-Jupiter line. At this position, approximately 40% of the day side hemisphere will overlap with the upstream hemisphere if we assume co-rotation of the magnetospheric plasma. Cunningham et al. (2015) reported also on earlier HST/COS observations that did not reveal any significant UV emission from Callisto's atmosphere. These
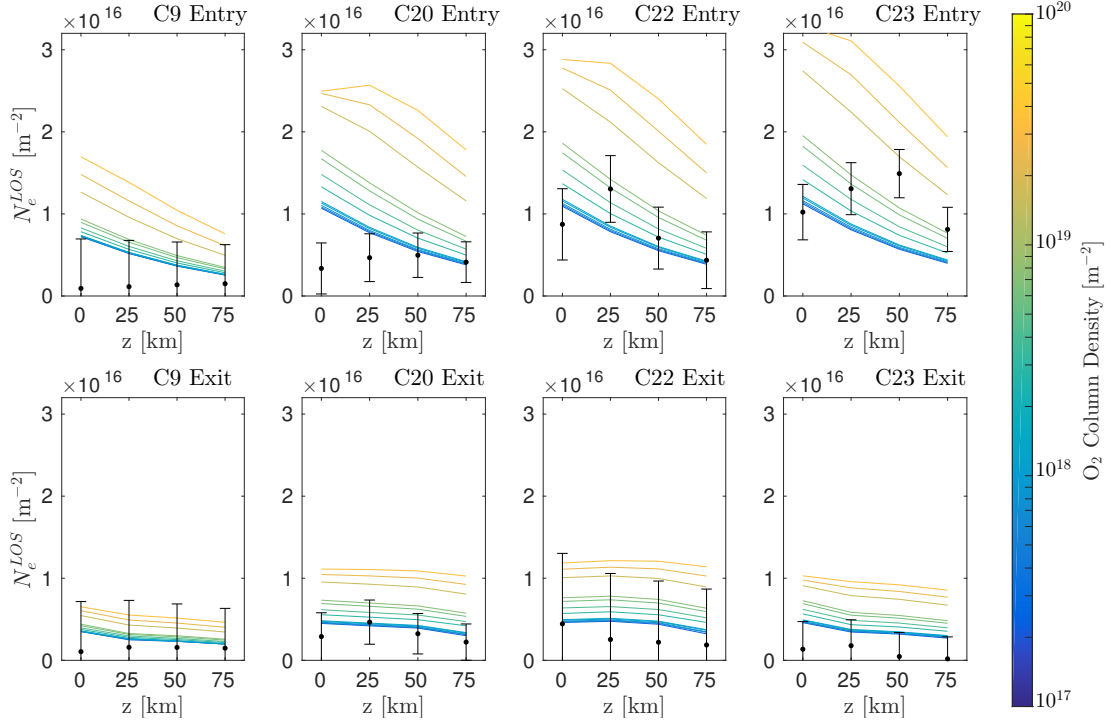
Figure 6.17: Radio occultation LOS electron column densities of different closest approach altitudes as in Figure 6.10. For western elongation, the CO_2 atmosphere is set to $N_{CO2} = 0.8 \times 10^{17}$ m^{-2} and H_2O is distributed as described by Equation (5.4). The atmosphere is assumed to be 3 times denser during western elongation (C-20, C-22, C-23) than during eastern elongation (C-9). The given O_2 column densities refer to the western elongation column density, which means that prescribed O_2 column densities during C-9 are 3 times smaller than illustrated by the colored lines.

observations were conducted when a smaller ratio of Callisto's day side hemisphere overlapped with the upstream hemisphere. Additionally, the solar photon flux was by a factor of two smaller in the EUV range during these earlier observations in comparison to the observation on November 17, 2011. Therefore, the available HST/COS observations also indicate that the atmospheric O_2 density might vary with the orbital phase and that the interplay of sputtering and photoionization is important for Callisto's atmosphere-ionosphere system and its observability. In order to test the hypothesis of the orbital phase variability rigorously, further HST observations of Callisto are required, especially when Callisto is located at western elongation. In Chapter 7, we present atmospheric OI λ135.6 nm emission intensities that are expected for an orbital phase dependent atmosphere density based on the modeling study of Plainaki et al. (2013) and our ionosphere model.

Moreover, magnetospheric variability is a second possible candidate for generating atmospheric O_2 density time-variations. The strongest ionospheric signal was detected during the entry of flyby C-23 when Callisto was close to the Jovian current sheet, a region of enhanced magnetospheric plasma particle flux (e.g., Seufert, 2012). An increased magnetospheric plasma particle flux can lead to an increase of the O_2 production rate via surface sputtering if it is accompanied by an increased energetic ion population. The effect on the atmosphere is non-linear because the atmospheric loss is affected by the plasma as well (e.g., Saur et al., 1998). The magnitude of the plasma particle flux is very variable at Callisto's orbit and has large uncertainties when extracted from the Galileo data (e.g., Seufert, 2012). From the limited set of available HST/COS observations, we, however, cannot identify a clear correlation between UV emission intensities and distances to the Jovian current sheet. Moreover, a detailed analysis of the role of the plasma transport requires also a proper description of Callisto's interaction with the upstreaming plasma.

7 Airglow predictions for a sputtering dominated atmosphere

In the previous chapter, we have already noted that assuming an orbital phase dependent O_2 atmosphere according to the study of Plainaki et al. (2013) improves the fitting of our ionosphere model with respect to radio occultation data from Kliore et al. (2002). In this chapter, we present predictions of atmospheric UV emission intensities for different orbital phases under the assumption that Callisto's O_2 atmosphere is created by surface sputtering and that, therefore, the Europa-atmosphere model of Plainaki et al. (2012) and Plainaki et al. (2013) is applicable. These predictions can be used by observers for interpretations of (future) Hubble Space Telescope observations of Callisto. Note that our here presented considerations are based on the atmosphere model of Plainaki et al. (2013) developed for Europa. It would be preferable to use a physical atmosphere model of Callisto that incorporates surface sputtering as an atmospheric source process. To our knowledge, only Vorburger et al. (2015) presented such an atmosphere model for Callisto. However, since their model does neither include collisions within the atmosphere nor a possible orbital dependency of the atmospheric density, we use the Europa-model of Plainaki et al. (2013) instead. The model of Plainaki et al. (2013) does not include collisions either, but it describes the potential orbital phase dependency. In the following, we explain how we modify this Europa-model in order to describe Callisto's atmosphere.

7.1 Deriving an orbital phase dependent O_2 atmosphere model for Callisto

Figure 7.1 shows the modeled atmosphere of Europa according to the study of Plainaki et al. (2013) for different orbital phases as published in Milillo et al. (2016). Plainaki et al. (2013) used the surface temperature dependent sputtering
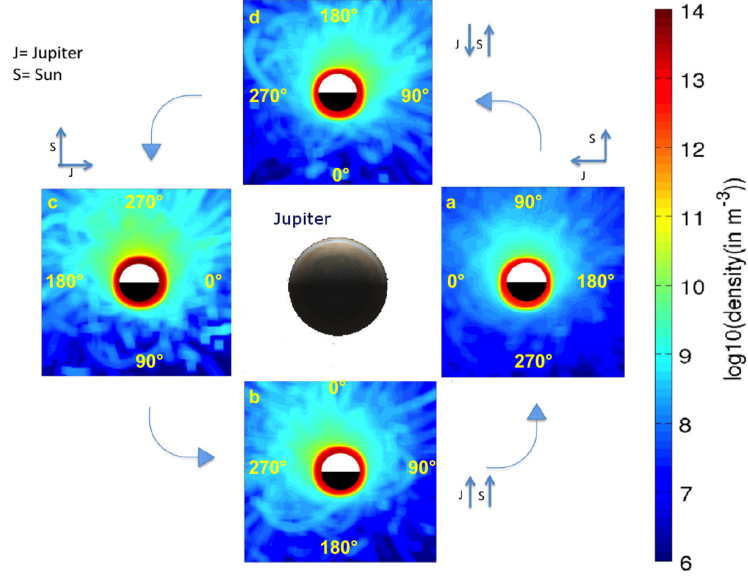
Figure 7.1: Atmosphere of Europa for different orbital phases as modeled by Plainaki et al. (2013). Longitudes are shown as yellow numbers for each position. This figure is taken from Milillo et al. (2016). Note that there is a small mistake. The longitudes 90° and 270° of the upper panel needs to be interchanged. The longitude of 90° is defined to be at the leading hemisphere.

yield according to Famá et al. (2008) and applied a Monte Carlo method to simulate the trajectories of multiple sputtered O_2 particles assuming that these particles do not experience any collisions. Based on this O_2 atmosphere model of Europa, Milillo et al. (2016) derived a 4-dimensional fit to describe the spatial distribution and the orbital phase dependency of the O_2 density n_{O2}^E analytically:

$$log_{10}\left[n_{O2}^E(r, \alpha_{eq}, \alpha_{lt}, \alpha_S)\right] = (p_5(\alpha_S) + p_6(\alpha_S)\ cos(\alpha_{eq} - p_7(\alpha_S))\ cos(\alpha_{lt})))$$
$$\times\ e^{-p_4(r-1)} - \frac{r-1}{p_1} + p_2(\alpha_S) \qquad (7.1)$$
$$+ p_3(\alpha_S)\ cos(\alpha_{eq} - p_7)\ cos(\alpha_{lt})$$

with the longitude of the subsolar point α_S in the coordinate system shown in Figure 7.1, the angle to the subsolar point in the equatorial plane $\alpha_{eq} = Long. - \alpha_S$ and off the equatorial plane α_{lt}, and with the radial distance r with possible values within the range of 1.05 to 5 Europa radii (R_E). Milillo et al. (2016) found the

following fitting parameters that describe the results of Plainaki et al. (2013):

$$p_1 = 2.51(\pm 0.4) \ ,$$
$$p_2(\alpha_S) = 9.0 - 0.3 \ sin(\alpha_S) \ ,$$
$$p_3(\alpha_S) = 0.71 - 0.09 \ sin(\alpha_S) \ ,$$
$$p_4 = 5.2 \ ,$$
$$p_5(\alpha_S) = 5.825 - 0.045 \ sin(\alpha_S) \ ,$$
$$p_6(\alpha_S) = -0.92 + 0.155 \ sin(\alpha_S) \ ,$$
$$p_7(\alpha_S) = -28 \ cos(\alpha_S) \ .$$

In the following, we explain how we adopt Expression (7.1) for Callisto. First, in order to account for the difference between the atmospheric scale heights of Europa and Callisto, we take the density distribution at the minimum valid Europa centered distance of 1.05 R_E, namely, $n_{O2}^E(1.05R_E, \alpha_{eq}, \alpha_{lt}, \alpha_S)$ as the surface density of a hydrostatic and isothermal atmosphere with the assumed scale height of Callisto's atmosphere, i.e., $H = 30$ km. Second, in order to account for the difference between the atmospheric densities, we scale the resulting column density distribution using the HST/COS observation of Callisto's O_2 atmosphere from November 17, 2011, which occurred when the subsolar point was located at $\alpha_S \approx 15°$ (compare with Figure 7.1). For this orbital phase, we have derived a mean O_2 column density of $2.1^{+1.1}_{-1.1} \times 10^{19}$ m^{-2} for Callisto's O_2 atmosphere by comparing the results of our ionosphere model with HST/COS observations (see Section 6.4.2.2). In this way, we find an orbital phase dependent O_2 column density distribution of $\tilde{N}_{O2}(\alpha_{eq}, \alpha_{lt}, \alpha_S) \approx 10 \ n_{O2}^E(1.05R_E, \alpha_{eq}, \alpha_{lt}, \alpha_S) \ H$. The scaling factor ~ 10 is chosen such that the spatial mean value of $\tilde{N}_{O2}(\alpha_{eq}, \alpha_{lt}, 15°)$ approximately equals $2.1^{+1.1}_{-1.1} \times 10^{19}$ m^{-2}.

Note that the following considerations are made under the preliminary assumption that surface sputtering dominates the O_2 atmosphere formation at Callisto. According to Equation (7.1), the extrema of neutral column densities are expected for eastern elongation (local time of 6:00, $\alpha_S = 270°$) and western elongation (local time of 18:00, $\alpha_S = 90°$). At eastern elongation, the atmosphere is expected to be least dense since the majority of magnetospheric particles impinge on the night side surface. In contrast, the atmosphere is expected to become densest at western elongation when the majority of magnetospheric particles impinge on the
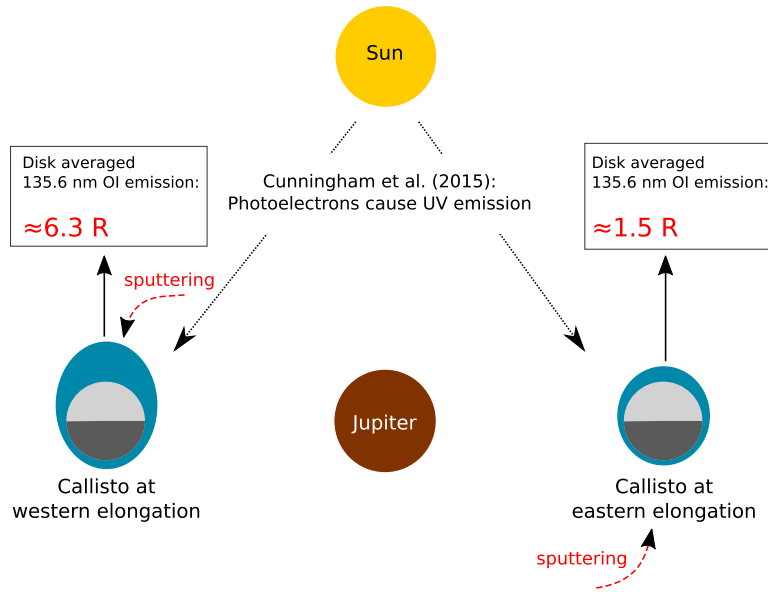
Figure 7.2: Scheme of principles for testing the hypothesis that surface sputtering creates an orbital phase dependent atmospheric O_2 density. Callisto is shown at eastern (right) and western (left) elongation with its atmosphere illustrated by the blue area. Note that the larger the blue area the larger the atmospheric O_2 density. This illustration is not true to scale.

warmer day side surface. The expected atmospheric asymmetry is a day-night asymmetry in both cases due to the dominance of the temperature dependency. This means that according to Plainaki et al. (2013), the surface ice temperature is the dominant parameter influencing the sputtering yield, while the rate of impinging particles is a secondary parameter. Both extreme cases, eastern and western elongation, are illustrated in the scheme in Figure 7.2, where a denser atmosphere is marked by an enlarged blue region around Callisto.

7.2 The idea of the hypothesis test

Using the Callisto-adopted orbital phase dependent O_2 density model of the previous section, we construct a test for the hypothesis that surface sputtering is the dominant O_2 atmosphere production process and creates an orbital phase dependent O_2 density variation as proposed initially for Europa by Plainaki et al. (2013). This test consists of the prediction and measurement of UV emissions at different orbital phases.
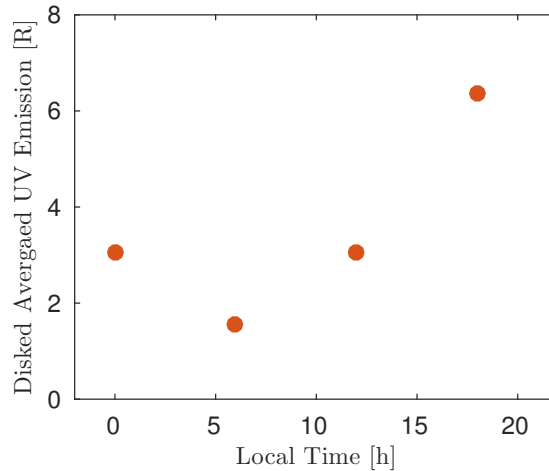
Figure 7.3: Predicted disked averaged OI $\lambda 135.6$ mn emissions of Callisto atmosphere as a function of local time under the assumption of a local time dependent atmosphere density according to Equation (7.1).

Figure 7.2 summarizes the principle ideas of this hypothesis test. If surface sputtering is the dominant source of atmospheric O_2, the generation of O_2 and the generation of OI $\lambda 135.6$ nm emission is decoupled. While magnetospheric particles cause surface sputtering and, hence, the production of O_2, the OI $\lambda 135.6$ nm emission is caused by photoelectrons which are primarily created by the ionizing radiation of the Sun (Strobel et al., 2002; Cunningham et al., 2015). Therefore, we can prescribe the O_2 atmosphere according to Equation (7.1) and then apply the ionosphere model of Section 6, i.e., Equations (6.1) - (6.5) and Equation (6.34). In this way, we can predict the OI $\lambda 135.6$ nm emission of Callisto's atmosphere, for instance, for western and eastern elongation. Figure 7.3 shows the predicted OI $\lambda 135.6$ nm UV emission intensities as a function of local time, i.e., orbital phase. Note that these predictions can be compared with telescope observations. Here, we only present the concept of testing the hypothesis of a sputtering dominated atmosphere formation. Indeed, HST/COS observations have already been conducted for both western and eastern elongation of Callisto in March 2017. These HST observations are led by John Spencer, the observational results are going to be published elsewhere.

If the hypothesis of an orbital phase dependent atmosphere is true, we will expect that the observations reveal significantly different airglow intensities at eastern and western elongation. At western elongation where the atmosphere is expected to be densest, we predict an OI $\lambda 135.6$ nm emission intensity of ~ 6.3 R

and at eastern elongation where the atmosphere is expected to be least dense, we predict an OI λ135.6 nm emission intensity of $\sim$1.5 R (see Figure 7.2). The so far published HST/COS observations from Cunningham et al. (2015) had an error range of $\sim$1.5 R regarding the OI λ135.6 nm emission intensity. Therefore, we expect a detectable discrepancy between eastern and western elongation since the expected error ranges of the predicted airglow intensities $1.5^{+1.5}_{-1.5}$ R and $6.3^{+1.5}_{-1.5}$ R would not overlap. If the hypothesis of an orbital phase dependent atmosphere is wrong, we will expect no detectable difference between airglow emissions at western and eastern elongation. In this case, surface sputtering might still play an important role, but it would apparently not create a strong orbital phase dependency of the atmospheric O_2 density.

8 Modeling electromagnetic induction in Callisto's ionosphere

On the basis of our model of Callisto's atmosphere-ionosphere system discussed in Chapter 5 and Chapter 6, we now investigate the ionospheric currents that are induced in Callisto's ionosphere and the associated magnetic fields. Up to now, there has been no detailed study of induction processes in Callisto's ionosphere. The magnetic field measurements by the Galileo magnetometer during the flybys C-3 and C-9 have been interpreted as signals of induction within a conductive spherical shell due to Jupiter's time variable magnetic field. This shell has been interpreted to be a conductive subsurface water ocean (Khurana et al., 1998). In order to determine the implications of ionospheric induction on this interpretation, we revisit the magnetic field measurements from the flybys C-3 and C-9 and calculate magnetic fields created by induction within Callisto's ionosphere due to Jupiter's time-variable magnetic field. Ionospheric conductivities are derived from the results of our modeling study of Callisto's atmosphere-ionosphere system, which are presented in Chapter 6 or in Hartkorn et al. (2017). From modeling the ionospheric induction, we gain new insight into properties of a possible subsurface ocean and its existence. Note that this Chapter 8 is submitted for publication in a similar version in Hartkorn and Saur (2017).

8.1 Basics of induction currents within Callisto's ionosphere

As discussed in Chapter 6, Callisto's ionosphere is mainly generated by photoionization and possesses an anisotropic and spatially varying electrical conductivity. This ionosphere is embedded in the flow of magnetized plasma of Jupiter's magnetosphere, which generates a motional electric field $\underline{E}^M$ seen in the rest frame of Callisto. The time-variable magnetic field of Jupiter's magnetosphere induces an

additional electric field $\underline{E}^{\dot{B}}$. Both electric fields drive ionospheric electric currents, which can be continued in parts into the Jovian magnetosphere through Callisto's Alfvén wings. In this section, we discuss the basic physical mechanisms of this setup. We construct a simplified analytic model to quantify the electric fields and the various electric currents in an ionosphere which couples to the surrounding magnetospheric plasma.

8.1.1 Conductivity structure of Callisto and its environment

The majority of Callisto's interior is expected to consist of a mixture of ice and rock (Anderson et al., 2001), which is approximately electrically non-conductive (as sketched in region III in Figure 8.1). Callisto might possess a conductive core (region V in Figure 8.1) and a conductive subsurface layer consisting of saline liquid water (Khurana et al., 1998), partly molten ice or polluted ice (Neubauer, 1998) (shown as region IV in Figure 8.1). These potential subsurface layers possess an isotropic conductivity σ_{iso} and the related conductivity tensor can be written as $\underline{\underline{\sigma}}_{iso} = \sigma_{iso}\underline{\underline{I}}$ with $\underline{\underline{I}}$ being the unit tensor. Therefore, Ohm's law for region III, IV and V reads

$$\underline{j} = \sigma_{iso}\underline{E} \ , \tag{8.1}$$

with the electric current density $\underline{j}$ and the electric field $\underline{E}$.

In contrast, the surrounding magnetized plasma possesses an anisotropic conductivity structure. Callisto's ionosphere (region II in Figure 8.1) reaches down to Callisto's surface, i.e., the top of region III, as shown by our results in Section 6.4. Ohm's law of the ionospheric region is given by

$$\underline{j} = \sigma_{\parallel}\underline{E}_{\parallel} + \sigma_P\underline{E}_{\perp} + \sigma_H\frac{\underline{B} \times \underline{E}}{B} \ , \tag{8.2}$$

where $\underline{E}_{\parallel}$ is the electric field parallel to the magnetic field $\underline{B}$, $\underline{E}_{\perp}$ the electric field perpendicular to the magnetic field, $\sigma_{\parallel}$ the electrical conductivity parallel to the magnetic field, σ_P the Pedersen conductivity, σ_H the Hall conductivity and B the magnitude of the magnetic field.

At the top of the ionosphere, currents can couple to Jupiter's magnetospheric plasma (region I in Figure 8.1). In this study, we assume a sub-Alfvénic plasma interaction at Callisto since this has been observed during all Callisto flybys of the Galileo spacecraft (e.g., Khurana et al., 1998; Seufert, 2012). Depending on
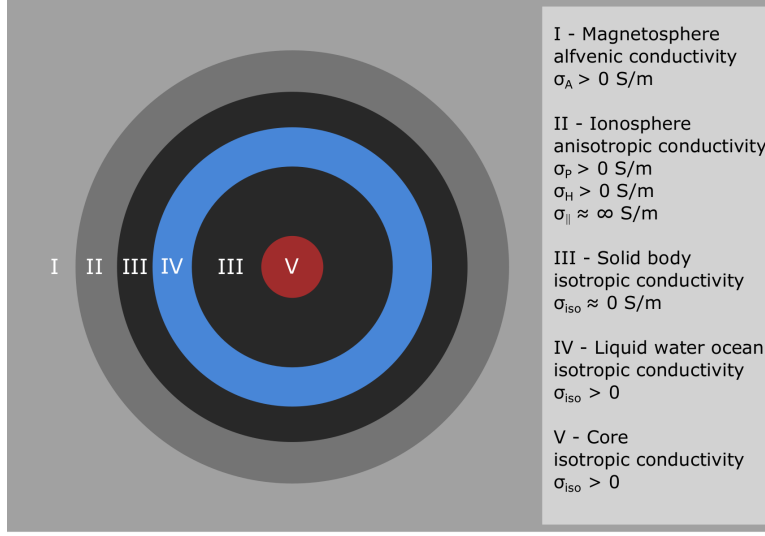
Figure 8.1: Schematic sketch of the different conductivity layers I-V of Callisto (structures III-V) and its environment (structures I-II).

the Alfvén travel time τ_A between Callisto and Jupiter's ionosphere compared to the convection time t_{conv} of the plasma past Callisto, the magnetospheric coupling can be described in the limit of the unipolar inductor model ($\tau_A/\tau_{conv} \ll 1$) or the Alfvén wing model ($\tau_A/\tau_{conv} \gg 1$) as discussed, e.g., in Neubauer (1998), Strobel et al. (2002) and Saur (2004). Because the ionospheric conductance of Jupiter and the Alfvén conductance assume similar values, both models generate similar coupling strengths besides some minor geometrical differences (Saur, 2004), which are not relevant for the principal discussion in this and the following sections. For mathematical simplicity, we assume in the following the Alfvénic far field coupling and describe the continuation of the ionospheric currents in the magnetosphere (region I in Figure 8.1) as

$$\underline{J}_A = \Sigma_A \nabla \cdot \underline{E}_\perp \; \underline{e}_A \; , \tag{8.3}$$

with the Alfvén conductance Σ_A and the unit vector along the Alfvén wing $\underline{e}_A$ (Neubauer, 1998).

8.1.2 Analytic induction model with Alfvénic far field coupling

Note that the analytic model described in the following (Section 8.1.2 - Section 8.1.4) has been mainly developed by Joachim Saur and is presented here similarly as published in Hartkorn and Saur (2017) since this model is crucial for the understanding of the subsequent modeling studies and discussions.

In order to understand currents induced in Callisto's ionosphere, we need to understand the associated induced electric fields. Two effects lead to electric fields seen in the rest frame of Callisto: First, the relative movement of plasma with a frozen-in magnetic field induces an unperturbed motional electric field $\underline{E}^M = -\underline{v} \times \underline{B}$, where $\underline{v}$ represents the plasma velocity in the rest frame of Callisto. Second, the time-variable magnetospheric field induces according to Faraday's law of induction $\nabla \times \underline{E} = -\partial_t \underline{B}$ an electric field $\underline{E}^{\dot{B}}$. The electric field $\underline{E}^M$ is approximately curl free, while $\underline{E}^{\dot{B}}$ is divergence free. These electric fields drive electric currents that separate charge, which generates curl-free electric fields. The resulting total electric field $\underline{E}$ can, thus, be written as the sum of the curl free part $\underline{E}^P$, which includes secondary fields in addition to $\underline{E}^M$, and the divergence free part $\underline{E}^{\dot{B}}$:

$$\underline{E} = \underline{E}^P + \underline{E}^{\dot{B}} = -\nabla\Phi - \partial_t \underline{A} \tag{8.4}$$

with the scalar potential Φ given by $\underline{E}^P = -\nabla\Phi$ and the vector potential $\underline{A}$ through $\underline{E}^{\dot{B}} = -\partial_t \underline{A}$ and $\underline{B} = \nabla \times \underline{A}$.

To better understand the resulting currents and secondary magnetic fields at Callisto, we apply a simplified model of an ionospheric cylinder of radius R, which is subject to both types of electric fields $\underline{E}^M$ and $\underline{E}^{\dot{B}}$. The cylinder shall represent Callisto's ionosphere and is chosen because it adopts to the anisotropic nature of the ionospheric electrical conductivity and, thus, is more convenient for mathematical reasons. Principal conclusions derived with this model would also hold for a spherical ionosphere.

The setup of the cylinder model is illustrated in Figure 8.2, where the induced electric fields $\underline{E}^M$ and $\underline{E}^{\dot{B}}$ are shown in yellow. The coordinate system (x,y,z) is chosen that the z-axis is the symmetry axis of the cylinder and the x-axis is aligned with the unperturbed magnetospheric plasma flow $\underline{v}_0$. The y-axis completes a right handed orthogonal coordinate system. Further, we use associated cylindrical
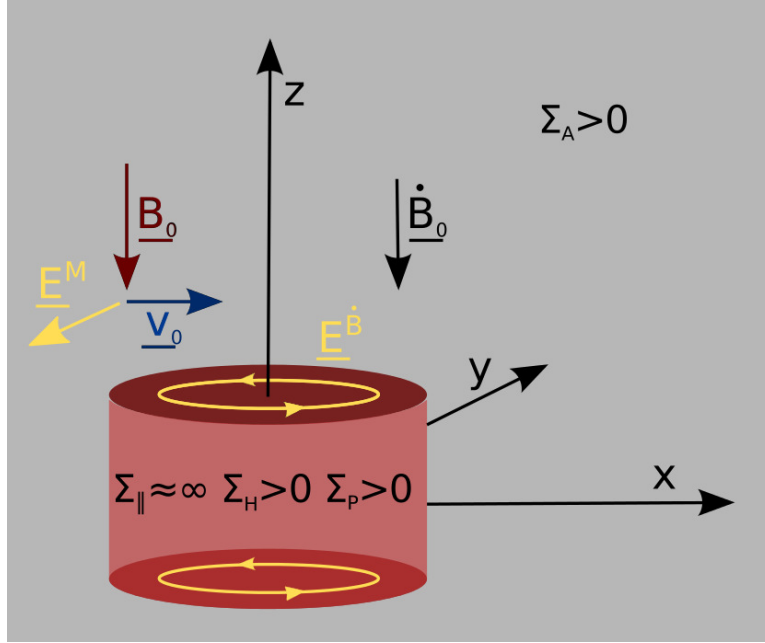
Figure 8.2: Design of the analytic induction model setup. The conductance within the red cylinder is anisotropic with Hall and Pedersen conductances and a nearly infinite parallel conductance. Outside the cylinder, currents can continue along the Alfvén characteristics due to a non-zero Alfvén conductance. Both types of induced electric fields $\underline{E}^M$ and $\underline{E}^{\dot{B}}$ ares shown in yellow. The magnetic field $\underline{B}_0$ is illustrated in red, its partial time derivative $\underline{\dot{B}}_0$ in black and the unperturbed magnetospheric flow velocity $\underline{v}_0$ in blue.

coordinates (r, φ, z).

The model derived here is a model that is based on perturbation theory, i.e., it assumes a given background magnetic field $\underline{B}_0 = -B_0 \underline{e}_z$ and calculates within that field the resultant electric field and electric currents. It is valid for the sub-Alfvénic case of plasma interaction and best applicable for small Alfvén Mach numbers. The Alfvén Mach number for Callisto varies from 0.02 to 8.5, with the lowest numbers the furthest away from the current sheet (Kivelson et al., 2004). Our model is intended for the case outside of the current sheet.

We assume for simplicity of this basic study that the magnetic background field $\underline{B}_0$ and its partial time derivative $\underline{\dot{B}}_0 \equiv \partial_t \underline{B}_0$ are both directed along the z-direction, here, $\underline{\dot{B}}_0 = -\dot{B}_0 \, \underline{e}_z$. This assumption is approximately valid for the magnetic field configuration at Callisto's orbital position when Callisto is outside of the current sheet. Further, our model is applicable for time intervals over which the change due to $\underline{\dot{B}}_0$ is small compared to $\underline{B}_0$ and describes quasi-stationary

solutions over time scales during which $\underline{\dot{B}}_0$ can be assumed to be approximately constant. Also this condition is met in case of Callisto when it is outside of the current sheet.

For the given configuration described above, the time-varying field $\underline{\dot{B}}_0$ generates according to Faraday's law of induction the electric field

$$\underline{E}^{\dot{B}} = \dot{B}_0 \frac{r}{2} \, \underline{e}_\varphi \, . \tag{8.5}$$

Under the assumption that the conductivity is spatially confined within the ionospheric cylinder, and the parallel conductivity is approximately infinite (see Section 8.2.2), Ohm's law in Equation (8.2) can be integrated along the magnetic field to obtain height integrated currents

$$\underline{J}_\perp = \Sigma_P \underline{E}_\perp + \Sigma_H \frac{\underline{B} \times \underline{E}}{B} \, , \tag{8.6}$$

with Σ_P the Pedersen conductance and Σ_H the Hall conductance, which have been integrated only within one hemisphere of the cylinder, i.e., starting from $z = 0$ (similar to Neubauer (1998) and Saur et al. (1999)). Thus, the total conductances of the total cylinder are twice as large. The ionospheric currents of each hemisphere can continue within the ambient magnetospheric plasma as Alfvénic currents $\underline{J}_A$ in its associated Alfvén wing where the wing currents are related to the electric field via Equation (8.3).

The electric current $\underline{J}_\perp$ perpendicular to $\underline{B}_0$ in Callisto's ionosphere is given by the electric field $\underline{E}$ in Equation (8.4) and the anisotropic Ohms law in Equation (8.6). Outside of the ionosphere, the electric current can only be closed by approximately field-aligned Alfvénic currents given by Equation (8.3). Current continuity, i.e.,

$$\nabla \cdot \underline{j} = 0 \tag{8.7}$$

needs to be applied for the ionospheric and field aligned currents. Thus, inserting (8.3) and (8.6) into (8.7) and using (8.4) and (8.5), leads to the following equation for the electric potential Φ

$$\dot{B}_0 \frac{r^2}{2} (\partial_r \Sigma_H) + \dot{B}_0 \Sigma_H r = \partial_r \left[r (\Sigma_p + \Sigma_A) \, \partial_r \Phi \right] + \frac{1}{r} \partial_\varphi \left[(\Sigma_P + \Sigma_A) \, \partial_\varphi \Phi \right]$$
$$+ (\partial_r \Sigma_H)(\partial_\varphi \Phi) - (\partial_\varphi \Sigma_H)(\partial_r \Phi) \, . \tag{8.8}$$

The mathematical procedure to derive Equation (8.8) is straight forward and identical to the description in the appendix of Saur et al. (1999) except for the two terms on the left hand side of Equation (8.8).

An analytic solution of Equation (8.8) can be achieved, when we assume that the Pedersen and Hall conductances are constant within the cylinder of radius R and zero outside. At large $r \to \infty$, the perturbations of the electric field caused by ionospheric currents need to vanish, i.e., $\underline{E}_0$ needs to be obtained. This implies for the electric potential at large distance that Φ becomes $\Phi_0 = E_0 \, r \sin \varphi$. In this case, Equation (8.8) can be solved (e.g., see appendix A of Hartkorn and Saur (2017)), which leads to the potential Φ^i inside the ionospheric cylinder, i.e., for $r \leq R$

$$\Phi^i = E_0 r (a \sin \varphi + b \cos \varphi) + \frac{\dot{B}_0}{4} \frac{\Sigma_H}{\Sigma_P + \Sigma_A} r^2 \ . \tag{8.9}$$

For the potential Φ^e outside the ionospheric cylinder, i.e., for $r \geq R$ we find

$$\Phi^e = E_0 \frac{R^2}{r} (g \sin \varphi + h \cos \varphi) + E_0 r \sin \varphi \tag{8.10}$$

with

$$a = \frac{2\Sigma_A (2\Sigma_A + \Sigma_P)}{\Sigma_H^2 + (2\Sigma_A + \Sigma_P)^2} \ , \tag{8.11}$$

$$b = -\frac{2\Sigma_A \Sigma_H}{\Sigma_H^2 + (2\Sigma_A + \Sigma_P)^2} \ , \tag{8.12}$$

$g = a - 1$, and $h = b$.

With the solution (8.9) combined with (8.4) and Ohm's law (8.6), we can calculate the currents within the cylinder using that they are perpendicular to the magnetic field. In spherical coordinates, these currents can be written as

$$J_{\perp,\varphi} = \left(\Sigma_P + \frac{\Sigma_H^2}{\Sigma_P + \Sigma_A} \right) E^{\dot{B}}$$
$$- \Sigma_P E_0 (a \cos \varphi - b \sin \varphi) + \Sigma_H E_0 (a \sin \varphi + b \cos \varphi) \ , \tag{8.13}$$

$$J_{\perp,r} = \left(\Sigma_A \frac{\Sigma_H}{\Sigma_P + \Sigma_A} \right) E^{\dot{B}}$$
$$- \Sigma_P E_0 (a \sin \varphi + b \cos \varphi) - \Sigma_H E_0 (a \cos \varphi - b \sin \varphi) \ . \tag{8.14}$$

It is remarkable that the ionospheric loop current $J_{\perp,\varphi}$ driven by the time-variability

of the magnetic field is controlled by an effective conductance

$$\Sigma_{eff} = \Sigma_p + \frac{\Sigma_H^2}{\Sigma_p + \Sigma_A} \ , \tag{8.15}$$

which will be approximately equal to the Cowling conductance known from the Earth equatorial electro jet in case of $\Sigma_A \ll \Sigma_H \sim \Sigma_P$ (e.g., Cowling, 1932; Baumjohann and Treumann, 2012). The time-variable magnetic field also drives radial electric currents controlled by an effective conductance

$$\Sigma_{eff}^r = \Sigma_A \frac{\Sigma_H}{\Sigma_p + \Sigma_A} \ , \tag{8.16}$$

determining the current closure into the magnetosphere. This effective conductance Σ_{eff}^r will be on the order of the Alfvén conductance if $\Sigma_A \ll \Sigma_H \sim \Sigma_P$.

8.1.3 Cowling channel effect in Callisto's ionosphere

In case of $\Sigma_A \ll \Sigma_H \sim \Sigma_P$, the effective conductance Σ_{eff} in Equation (8.15) describes an enhancement effect which is caused by the anisotropy of the ionospheric conductivity. At Callisto, the Alfvén conductance Σ_A within the ambient plasma lies between 0.1 S outside the current sheet and 25 S inside the current sheet (Strobel et al., 2002; Kivelson et al., 2004). It is, therefore, very much smaller than the ionospheric Pedersen conductance Σ_P, which is on the order of 3200 S (800 - 5600 S), and the ionospheric Hall conductance Σ_H, which is on the order of 8800 S (2200 - 15600 S) (Σ_P and Σ_H have been extracted from our ionosphere model of Chapter 6 as discussed in Section 8.2.2). Here, the given ranges for Σ_P and Σ_H in the brackets refer to the minimum and maximum values derived from the height integration along the magnetic field at the magnetic pole (minimum) and the magnetic equator (maximum).

Figure 8.3 illustrates the enhancement effect for simplicity under the assumption that $\Sigma_A \approx 0$, which is a good approximation of Callisto's case $\Sigma_A \ll \Sigma_P \sim \Sigma_H$ (see Equation (8.15)). This illustration shows that due to the time varying magnetic field, a primary Pedersen current $\underline{j}_P^{prim}$ is induced within the shell, which is in this case a pure loop current. Further, primary Hall currents $\underline{j}_H^{prim}$ are driven which are directed radially outward. If $\Sigma_A \neq 0$, these Hall currents will be continued into Jupiter's magnetosphere but limited by the Alfvén conductance. The limitation

of this ionosphere magnetosphere coupling is expressed by the effective radial conductance given in Equation (8.16). If the coupling is limited, the Hall currents will generate charge separation causing a secondary compensation electric field $\underline{E}^C$. This compensation field drives secondary Pedersen currents $\underline{j}_P^{sec}$ directed radially inward and a secondary Hall current $\underline{j}_H^{sec}$, which is a loop current again and, hence, enhances the primary Pedersen loop current leading to an effective azimuthal conductance given by Equation (8.15). In particular Equation (8.15) and (8.16) can be interpreted such that in the case of an approximate parallel alignment of the background magnetic field and its time derivative, a cylindrical or spherical shell with anisotropic conductivity structure characterized by the conductances Σ_P and Σ_H responses in a similar way to the time varying magnetic field as a shell of the same geometry with an isotropic conductivity structure characterized by the conductance Σ_{eff}.

In the case of no ionospheric current continuation in the Jovian magnetosphere, a complete Cowling channel would be established as shown in Figure 8.3. The formation of such enhancement effects, i.e., Cowling channels, are known in different
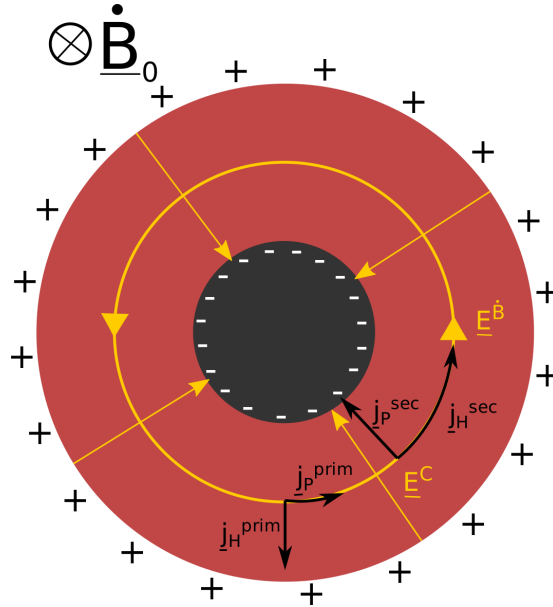
Figure 8.3: Schematic illustration of Cowling channel effect within Callisto's ionosphere. The ionosphere is illustrated by the red region and its extend has been enhanced for clarity reasons. The view is into the direction of a time varying magnetic field $\underline{\dot{B}}_0$. The induced electric field $\underline{E}^{\dot{B}}$ and the compensation electric field $\underline{E}^C$ are shown by yellow arrows. Primary and secondary Pedersen and Hall currents are shown by black arrows.

geometries from the Earth's equatorial electro jet (e.g., Cowling, 1932; Baumjo-hann and Treumann, 2012). According to Expression (8.15), the enhancement effect at Callisto depends on the current continued via Alfvén waves and, there-fore, on the ratio of the Alfvén conductance and the perpendicular ionospheric conductances. Hence, Equation (8.15) describes a marginally incomplete Cowling channel for Callisto.

8.1.4 Comparison of electric fields and currents driven at Callisto

In this section, we compare the strengths of the electric fields induced by the motion of Callisto and by the time-variable magnetic field and their related current systems. For this purpose, we estimate the respective electric field amplitudes and current amplitudes using our analytic cylinder model. For the following order of magnitude discussion, the radius of the cylinder R is set to the radius of Callisto $R_C = 2410$ km.

The amplitude of the unperturbed motion electric field $\underline{E}^M = -\underline{v}_0 \times \underline{B_0}$ is

$$E_0 = v_0\,B_0 \approx d\,\Omega\,B_0 \; , \tag{8.17}$$

with the synodic angular rotation frequency of Jupiter $\Omega = 2\pi/T$, where the synodic rotation period is given by $T = 10.18$ h, and d is the distance of Callisto from the center of Jupiter, which is 1.89×10^6 km. Here, we assume that the magnetospheric plasma at the location of Callisto is fully co-rotating. The amplitude of the electric field induced by the time-variable magnetic field $E^{\dot{B}}$ is maximal at $r = R$ with

$$E^{\dot{B}} = \dot{B}_0 R/2 \approx \frac{B_0}{T} R/2 = \frac{B_0 \Omega R}{4\pi} \; , \tag{8.18}$$

where we assume that $\dot{B}_0$ can be approximated by B_0/T. The ionospheric electrical conductances reduce the amplitude of the motional electric field E^M to (calculated from Equation (8.9) or see similar expressions in Saur et al. (1999))

$$E^p = E_0 \frac{2\Sigma_A}{(\Sigma_H^2 + (\Sigma_P + 2\Sigma_A)^2)^{1/2}} \approx E_0 \frac{2\Sigma_A}{(\Sigma_H^2 + \Sigma_P^2)^{1/2}} \; , \tag{8.19}$$

where we have assumed that $\Sigma_A \ll \Sigma_P \sim \Sigma_H$. Note that the electric field due to the time-variable magnetic field in the ionosphere is modified by the induction processes itself, i.e., the induction generates electric currents, which cause time-variable magnetic fields modifying the inducing electric field. This process will be investigate quantitatively in Section 8.2.

First, we compare the electric field due to $\underline{\dot{B}}_0$ with the perturbed motional electric field. Considering the maximum ionospheric electric field due to $\underline{\dot{B}}_0$, we find the ratio

$$\frac{E^{\dot{B}}}{E_p} = \frac{1}{4\pi} \frac{R}{d} \frac{(\Sigma_H^2 + \Sigma_P^2)^{1/2}}{\Sigma_A} \approx 0.04 - 9.5 \ , \tag{8.20}$$

where we use the range of Alfvén conductances $\Sigma_A = 0.1 - 25$ S as reported by Kivelson et al. (2004) and use $\Sigma_P = 3200$ S and $\Sigma_H = 8800$ S according to our discussion in Section 8.2.2. This range of the Alfvén conductance will be used also for the following estimates in this section.

Now we estimate the electric currents driven in Callisto's ionosphere. The azimuthal electric current due to the time-variable magnetic field, i.e., the first term in Expression (8.13) can be integrated in the radial direction to obtain the total electric loop current

$$J_{\varphi,total}^{\dot{B}} = \Sigma_{eff} \dot{B}_0 R^2 / 4 \ . \tag{8.21}$$

The radial current generated by $\underline{\dot{B}}_0$ at $r = R$ and integrated over the surface of the cylinder, i.e., the current which closes as Alfvénic currents is

$$J_{r,total}^{\dot{B}} = \Sigma_{eff}^r \dot{B}_0 \pi R^2 \tag{8.22}$$

The integrated current driven by the motional electric field $\underline{E}_M$ which closes in one Alfvén wing is given by (calculated from Expression (8.14) or expressions in Saur et al. (1999))

$$J_{A,total}^M = 4\Sigma_A E_0 \left(\frac{\Sigma_P^2 + \Sigma_H^2}{\Sigma_H^2 + (\Sigma_P + 2\Sigma_A)^2} \right) R \approx 4\Sigma_A E_0 R \tag{8.23}$$

for $\Sigma_A \ll \Sigma_P \sim \Sigma_H$.

Now we compare the loop current in the ionosphere to the total Alfvénic current

driven by the motional electric field. The ratio is

$$\frac{J_{\varphi,total}^{\dot{B}}}{J_{A,total}^{M}} = \frac{1}{32\pi}\frac{R}{d}\frac{\Sigma_H^2 + \Sigma_P^2}{\Sigma_P\Sigma_A} \approx 0.01 - 3.5 \tag{8.24}$$

for the same Σ_A, Σ_P and Σ_H as for the relation in Expression (8.20). The ratio of the radial current driven by the $\underline{\dot{B}}_0$ due to the Hall effect compared to currents of the motional electric field is

$$\frac{J_{r,total}^{\dot{B}}}{J_{A,total}^{M}} = \frac{1}{8}\frac{R}{d}\frac{\Sigma_H}{\Sigma_P} \approx 4.4 \times 10^{-4} \ . \tag{8.25}$$

This implies that the Alfvénic currents are primarily caused by the motional electric field, and not by the induction electric field due the time-variable magnetic field.

The main results of the estimates made above is that the electric fields and the electric currents due to the time-variable magnetic field can reach the same order of magnitude as those generated due to the motion of Jupiter's magnetospheric plasma for the assumed conductances. The further outside Callisto is from the central current sheet the smaller the Alfvén conductance, while the ionospheric conductances vary less strongly in a photoionization driven ionosphere. Thus, the importance of induction in the ionosphere compared to the effects of the plasma interaction (i.e., of the motional electric field) is enhanced the further Callisto is away from the current sheet. Note that these considerations are only orders of magnitude estimates to identify the various roles of electromagnetic induction in Callisto's ionosphere. We also note that these estimates include simplifying assumptions such as constant conductivities within a cylinder.

Note that our analytic cylinder model is based on a fluid approach and assumes, therefore, small ion gyroradii in comparison with Callisto's radius. Now we show that this assumption is valid, especially when Callisto is located outside of the current sheet. Because Callisto's ionosphere is photoionization dominated, the bulk part of the ionospheric ions are produced within the ionosphere and are not convected into the ionosphere from the magnetosphere. When an ion is generated it is picked up by the local electric field and acquires an associated gyroradius. Assuming that the electric field can be approximated by the modified motional

electric field $\underline{E}^P$ from Equation (8.19), the ion gyroradius is given by

$$r_g = \frac{v_\perp}{\omega_{ci}} = \frac{E^p \, m_i}{B_0^2 q_i} = \frac{m_i}{q_i} \frac{d \, \Omega}{B_0} \frac{2\Sigma_A}{(\Sigma_H^2 + \Sigma_P^2)^{1/2}} \approx 0.05 - 140 \text{ km} , \qquad (8.26)$$

with $v_\perp$ the plasma (ion) velocity perpendicular to the magnetic field, ω_{ci} the ion cyclotron frequency (gyrofrequency), m_i and q_i the mass and charge of a O_2^+ ion, respectively. At Callisto, O_2^+ is the major ionospheric ion species as discussed in Chapter 6. For the magnetic field, we consider the range $B_0 = 4 - 42$ nT (Kivelson et al., 2004). During the relevant Galileo flybys C-3 and C-9, Callisto was outside the current sheet with $B_0 \approx 35$ nT and $\Sigma_A \approx 1$ S. In this case, the resultant r_g is on the order of 1 km and, hence, significantly smaller than the radius of Callisto. This ratio justifies the applied fluid based model of the ionospheric conductivities.

As a consequence of our analytic cylinder model we find that ionospheric currents induced by a time varying magnetic field play an important role at Callisto. Further, our analytic model has shown that there is only a weak continuation of ionospheric currents generated by $\underline{\dot{B}}$ in the Jovian magnetosphere. Therefore, we will neglect this continuation by considering the environment surrounding Callisto's ionosphere to be non-conductive in the following quantitative study.

8.2 Quantitative numerical induction model

Now, we focus on a detailed description of induction driven by the time-variable magnetic field in Callisto's ionosphere. We compare calculated magnetic fields with the measurements from the flybys C-3 and C-9. Our numerical calculations of magnetic induction are performed in the Callisto centered CPhiO coordinate system (x', y', z'), which we have presented in Section 2.2.

8.2.1 Calculating induced magnetic fields

In order to calculate the induced magnetic fields due to the time-variable magnetic field in Callisto's ionosphere, we now abandon the cylindrical model from the previous section and apply a more realistic model of Callisto's ionosphere. We then investigate the electrodynamical behavior of this setup when it is exposed to a time varying magnetic field. We write the magnetic field $\underline{B}$ as a sum of the time-constant magnetic field $\underline{B}_{cst}$, the inducing magnetic field $\delta\underline{B}$ and the induced field $\underline{B}_{ind}$ such
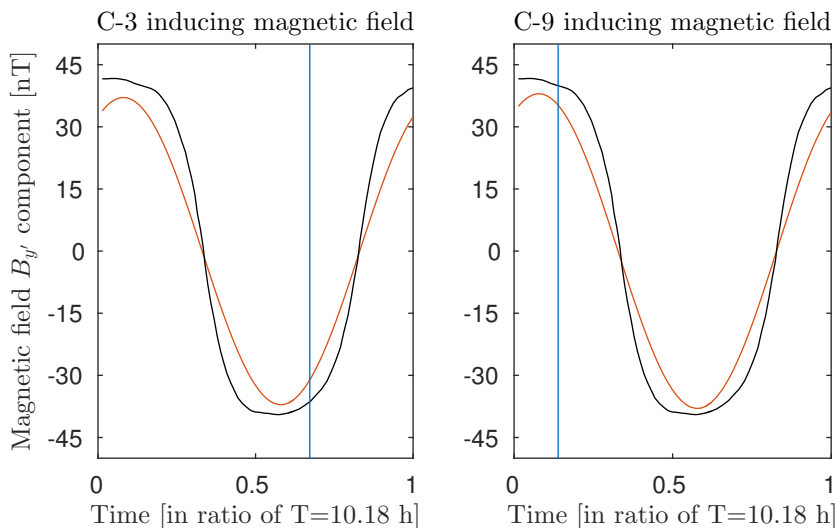
Figure 8.4: y' component of the derived inducing magnetic field $\delta\underline{B}(t)$ at Callisto (red lines) for flyby C-3 (left panel) and flyby C-9 (right panel), shown over a single synodic rotation period of Jupiter's magnetic field $T = 10.18$ h. The point $t = 0$ corresponds to the System III coordinate west longitude point $\lambda_{III} = 0$ (Kivelson et al., 1999, figure 1b). The blue lines mark the times of the flybys t_0. The y'-component of the magnetic field $\underline{B}^m(t)$ according to Kivelson et al. (1999) is shown as black line.

that $\underline{B} = \underline{B}_{cst} + \delta\underline{B} + \underline{B}_{ind}$. The time-constant magnetic field $\underline{B}_{cst}$ together with the inducing magnetic field $\delta\underline{B}$ represent Jupiter's magnetospheric field at the location of Callisto, which we also call the primary magnetic field $\underline{B}_p = \underline{B}_{cst} + \delta\underline{B}$. The purpose of our model is to calculate the induced magnetic field for a given primary magnetic field. At Callisto, the time-constant magnetic field possesses only a significant z'-component of approximately -6.5 nT (Kivelson et al., 1999, figure 1b). The inducing field is well approximated by its x'-component and y'-component $\delta\underline{B} = \delta B_{x'}\underline{e}_{x'} + \delta B_{y'}\underline{e}_{y'}$ as the weak time variation of the inducing field's z'-component is negligible in a first-order treatment. For the frequency of the inducing field, we consider only the synodic rotation frequency of Jupiter since this is the dominant one at Callisto (e.g., Seufert et al., 2011).

The induced field is generally delayed in time with respect to the inducing field in layers of finite conductivity, i.e., it might possess a temporal phase shift ϕ between $-90°$ and $0°$. Therefore, we need to consider the time characteristics of the inducing field $\delta\underline{B}(t)$ and estimate its vector amplitude $\delta\underline{B}_0$ and its current phase ϕ_0 for the times of the flybys using complex notation, i.e., $\delta\underline{B} = Re\left\{\delta\underline{B}_0 e^{i\phi_0}\right\}$.

We derive $\delta\underline{B}_0$ and ϕ_0 as follows: First, we determine the inducing magnetic

Flyby	ϕ_0	Comp.	$\delta\underline{B}_0$ [nT]	$\text{Re}\{\delta\underline{B}_0 e^{i\phi_0}\}$ [nT]	$\delta\underline{B}^{C/A}$ [nT]
C-3	213°	x	5.09	-4.27	-4.27
		y	37.10	-31.10	-31.05
C-9	22°	x	2.90	2.69	2.70
		y	38.0	35.23	35.55

Table 8.1: Inducing field amplitudes $\delta\underline{B}_0$ and phases ϕ_0 at the times of the flybys C-3 and C-9 corresponding to the synodic rotation period of Jupiter $T = 10.18$ h, observed inducing magnetic field $\delta\underline{B}^{C/A}$ at closest approach and representation through maximum inducing field and associated phase, i.e., $\delta\underline{B}(t_0) = \text{Re}\{\delta\underline{B}_0 e^{i\phi_0}\}$.

field $\delta\underline{B}^{C/A}$ at the time of closest approach for specific Galileo flybys from the magnetic field data of the individual flyby as described by Zimmer et al. (2000). The times of the specific flybys t_0, i.e., the times of the closest approaches are marked by blue vertical lines in Figure 8.4, where the time dependence of the y'-component of the inducing field is shown for the flybys C-3 and C-9. Second, we determine a combination of $\delta\underline{B}_0$ and ϕ_0 such that the inducing field $\delta\underline{B}$ ($\delta B_{y'}$ shown as red line in Figure 8.4) fits to the measurement $\delta\underline{B}^{C/A}$ at the times of each individual flyby. In Figure 8.4, the inducing field at the closest approach is given by the point where the red and the blue curve intersect, associated values are given in Table 8.1. Third, these values can be compared with the model of the Jovian magnetic field presented by Kivelson et al. (1999). This model provides the magnetic field at Callisto's position $\underline{B}^m(t)$ as a function of time. Figure 8.4 shows $B_{y'}^m(t)$ as black line for a synodic period of Jupiter's rotation. Our approach leads to an inducing magnetic field (red line), which fits the general characteristic of the field $\underline{B}^m$. Derived quantities of $\delta\underline{B}_0$, ϕ_0, $\delta\underline{B}(t_0)$ and $\delta\underline{B}^{C/A}$ are given in Table 8.1.

For given constant and inducing magnetic fields, we solve the dynamic Maxwell equations in order to determine the induced field $\underline{B}_{ind}$ at Callisto:

$$\nabla \times \underline{E} = -\dot{\underline{B}} , \tag{8.27}$$

$$\nabla \times \underline{B} = \mu_0\underline{j} + \mu_0\epsilon_0\dot{\underline{E}} , \tag{8.28}$$

with the vacuum permittivity ϵ_0 and the vacuum permeability μ_0. The relation between the electric field $\underline{E}$ and the electric current $\underline{j}$ is given by Equation (8.2) for the ionosphere and by Equation (8.1) for Callisto's interior. Here, we neglect the

current continuation into the magnetospheric plasma, which practically amounts to assuming Callisto's ionosphere is surrounded by a vacuum (see discussion in Section 8.1). We solve Equation (8.27) and Equation (8.28) in frequency domain using a field potential formalism with the magnetic vector potential $\underline{A}$. The resulting field potential equation is solved numerically for given spatial conductivity tensor distributions using the software package COMSOL Multiphysics® and its AC/DC module extension (COMSOL, 2013). The numerical solution is based on a finite element solver that is applied to a three dimensional simulation setup.

The simulation setup contains Callisto as a sphere with the radius R_C, the ionosphere and an environmental spherical shell enveloping the ionosphere with a thickness of $2R_C$. Optionally, we also consider spherical conductivity structures in the subsurface which can represent saline water (e.g., Zimmer et al., 2000), polluted ice or partly molten ice, i.e., dirty ice (Neubauer, 1998). Both, Callisto and the environment above the ionosphere are modeled as approximate electrical insulators with a finite conductivity of 10^{-8} S m^{-1} (see discussion in Section 8.1). The outer boundary conditions are initialized by infinite elements enveloping the simulation domain (e.g., Zienkiewicz et al., 1983). According to Figure 8.1, our model setup includes regions II, III and optionally region IV as illustrated in Figure 8.1. We do not discuss cases including a core since Zimmer et al. (2000) already found that a core has to have a relatively large extend to explain the observed induction signals, which is too large to be consistent with results of gravitational measurements from Anderson et al. (1998) (see also Section 3.1.4).

For the sake of simplicity, we neglect that the conductivity tensor in Equation (8.1) and Equation (8.2) depends secondarily on the induced field itself. Consequently, we restrict the functional dependency of the conductivity tensor to the primary magnetic field, i.e., $\underline{\underline{\sigma}} = \underline{\underline{\sigma}}(\underline{B}_p)$.

8.2.2 Setup of the ionosphere

Due to computational constraints and since we are interested in the integral induction effect of the ionosphere seen from Galileo flyby trajectories outside the ionosphere, our basic model of Callisto's ionosphere is a simple spherical shell with globally constant Pedersen, Hall and parallel conductivities. In the following, we describe how we derive these representative conductivities and the spatial extend of the ionospheric shell.

First, we calculate the spatial conductivity distribution of Callisto's ionosphere according to our ionosphere model from Chapter 6. Our ionosphere model describes the day side ionosphere which is primarily generated by photoionization (Cunningham et al., 2015). A night side ionosphere is likely present due to electron impact ionization and transport effects. As the night side ionosphere is only very weakly constrained and expected to be less conductive than the day side ionosphere, we consider only the day side ionosphere in order to derive global average conductivities. Since a consideration of the night side ionosphere would increase derived average conductivities of a global ionosphere, later derived ionospheric conductivities are lower limits in this regard.

For the day side ionosphere, our ionosphere model from Chapter 6 provides the spatial distributions of the electron density $n_e(\underline{r})$, the O_2^+ density $n_{i,1}(\underline{r})$ and neutral densities $n_{n,1}(\underline{r})$, $n_{n,2}(\underline{r})$ and $n_{n,3}(\underline{r})$ for O_2, CO_2 and H_2O (see nomenclature in Chapter 6). For deriving electrical conductivities, we choose the spherical symmetric O_2 density distribution with an O_2 column density of 2.1×10^{19} m^{-2} that fits best to the HST observations reported by Cunningham et al. (2015) (see Section 6.4.2.2). Assuming a single ion species O_2^+ in agreement with the findings of Liang et al. (2005), we calculate the spatial distribution of Pedersen, Hall and parallel conductivities according to

$$\sigma_p(\underline{r}) = \frac{n_e \, e}{B_p} \left(\frac{\nu_{en}\omega_{ce}}{\nu_{en}^2 + \omega_{ce}^2} + \frac{\nu_{in}\omega_{ci}}{\nu_{in}^2 + \omega_{ci}^2} \right) , \qquad (8.29)$$

$$\sigma_H(\underline{r}) = \frac{n_e \, e}{B_p} \left(\frac{\omega_{ce}^2}{\nu_{en}^2 + \omega_{ce}^2} - \frac{\omega_{ci}^2}{\nu_{in}^2 + \omega_{ci}^2} \right) , \qquad (8.30)$$

$$\sigma_{\parallel}(\underline{r}) = n_e \, e^2 \left(\frac{1}{m_e \nu_{en}} + \frac{1}{m_i \nu_{in}} \right) , \qquad (8.31)$$

with the magnitude of the primary magnetic field $B_p = |\underline{B}_p|$ ($\sim$33 nT for C-3 and $\sim$37 nT for C-9), e the elementary charge and the electron cyclotron frequency $\omega_{ce} = eB_p/m_e$. Note that both cyclotron frequencies, ω_{ce} and ω_{ci}, are defined as positive numbers in the here applied convention. The electron-neutral collision frequency ν_{en} is given by $\nu_{en} = \sum_{s=1}^{3} n_{n,s}(\underline{r})\sigma_{en,s}\overline{v_e}$ (e.g., Baumjohann and Treumann, 2012) where s refers to the neutrals species and with total electron-neutral cross sections $\sigma_{en,s}$ taken from Anzai et al. (2012) for an average electron energy of $\overline{E}_e = 0.1$ eV and with the average electron velocity $\overline{v}_e = \sqrt{2\overline{E}_e/m_e}$. The ion neutral collision frequency ν_{in} is given by $\nu_{in} = \sum_{s=1}^{3} 2.6 \times 10^{-15} n_{n,s}(\underline{r})\sqrt{\alpha_s/\mu_s}$
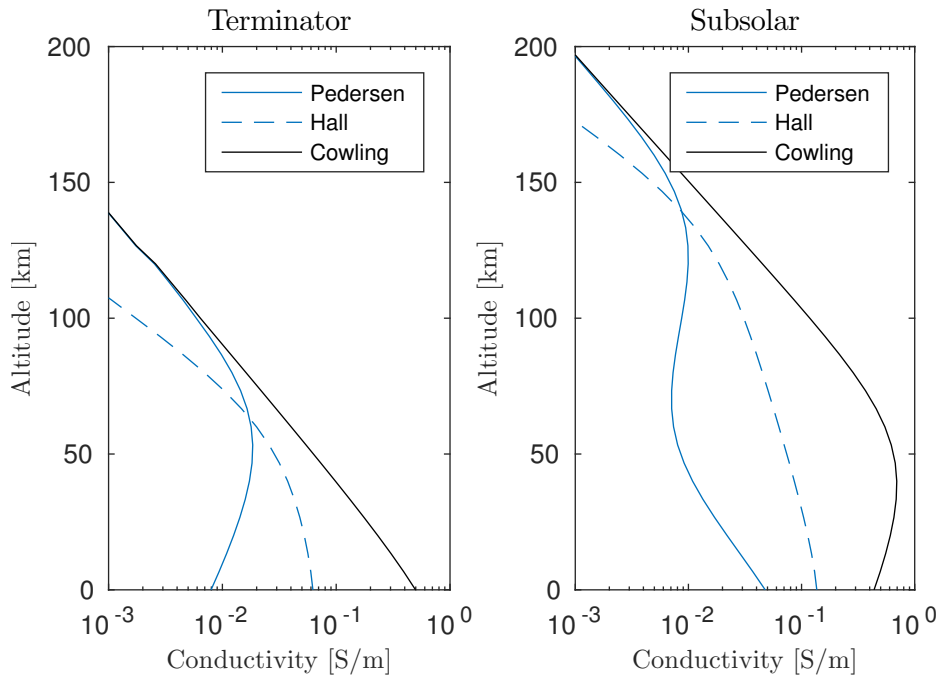
Figure 8.5: Altitude profiles of Pedersen (σ_P), Hall (σ_H) and Cowling (σ_C) conductivity as derived from our ionosphere model, at the terminator (left panel) and at the subsolar point (right panel). Pedersen (blue solid line) and Hall (blue dashed line) conductivities are calculated according to Equations (8.29) and (8.30), Cowling conductivities σ_C (black solid line) are calculated according to $\sigma_C = \sigma_P + \sigma_H^2/\sigma_P$. The underlying atmosphere consists of a spherically symmetric O_2 atmosphere with a column density of 2.1×10^{19} m^{-2}, the CO_2 column density is 0.80×10^{19} m^{-2} and the H_2O atmosphere is incorporated as described by Equation (5.4).

(Banks and Kockarts, 1973) with reduced masses $\mu_s = (m_s m_i)/(m_s + m_i)$, m_s representing the mass of the neutral species s, and polarizabilities α_s taken from Banks and Kockarts (1973, Table 9.10) for O_2 and CO_2 and from Nir et al. (1973) for H_2O. Exemplary, Figure 8.5 shows Pedersen and Hall conductivity altitude profiles for the terminator and the subsolar point derived from our ionosphere model using Equation (8.29), (8.30) and (8.31). In order to illustrate the significance of the Cowling channel effect, Figure 8.5 shows the associated Cowling conductivity profiles as well.

From the calculated three dimensional conductivity distribution, we infer global averages of Pedersen, Hall and parallel conductivity ($\overline{\sigma}_P, \overline{\sigma}_H, \overline{\sigma}_\parallel$) which then characterize the ionospheric shell of our simulation setup. The averages are calculated by integrating the local conductivity values over the whole model ionosphere and dividing the result through the volume of the here used model

ionosphere $V_{iono} = \frac{4\pi}{3}((R_C + H_{iono})^3 - R_C^3)$ where H_{iono} is the thickness of our model ionosphere. For example, the average Pedersen conductivity is calculated by

$$\overline{\sigma}_P = \frac{1}{V_{\text{iono}}} \int_{\text{ionosphere}} \sigma_P(\underline{r}) \, \mathrm{d}V \ . \tag{8.32}$$

The thickness of the ionospheric shell H_{iono} shall reflect the spatial extend of Callisto's ionosphere. Additionally, we have to consider that the larger the chosen H_{iono}, the smaller the distance between the top of the model ionosphere and the closest approach altitudes of the Galileo flybys C-3 and C-9, which could disturb the desired integral effect of the ionosphere. Hall conductivity profiles inferred from our ionosphere model show their maximum at the surface and decrease exponentially with altitude with a scale height of 60-80 km. The peaks of the inferred Pedersen conductivity profiles are located at altitudes between 60 and 120 km (see Figure 8.5). The closest approach altitudes of the flybys C-3 and C-9 are 418 km and 1136 km, respectively. We found that a thickness of $H_{iono} = 100$ km reflects the spatial extend of Callisto's ionosphere, is numerically treatable and is also sufficiently small with respect to the closest approach altitudes.

For the chosen ionospheric shell thickness of 100 km, we derive an average Pedersen conductivity of 0.008 S m^{-1}, an average Hall conductivity of 0.022 S m^{-1} and an average parallel conductivity of 80 S m^{-1}. These conductivities are valid for both considered flybys C-3 and C-9 as the ionizing solar flux had similar intensities during both flybys. For discussions in Section 8.1 and Section 8.4, we derive height integrated conductivities from the used ionospheric shell. Minimum conductances are derived at the magnetic poles of Callisto where we find a Pedersen conductance of $\Sigma_P^{min} = 800$ S and a Hall conductance of $\Sigma_H^{min} = 2200$ S. Maximum conductances are derived at the magnetic equator of Callisto where we find a Pedersen conductance of $\Sigma_P^{max} = 5600$ S and a Hall conductance of $\Sigma_H^{max} = 15600$ S. The associated mean values are given by $\Sigma_P = 3200$ S for the Pedersen conductance and by $\Sigma_H = 8800$ S for the Hall conductance.

Our induction model allows for investigations of the effects of likely day-night asymmetries of the ionospheric conductivity distribution using the parametrization

$$\underline{\underline{\sigma}}_{dn}(\beta) = \underline{\underline{\sigma}}_0 \left(1 + \kappa \, cos(\beta)\right) , \tag{8.33}$$

where $\underline{\underline{\sigma}}_0$ is the conductivity tensor at the terminator and κ defines the asymmetry strength.

8.3 Results of the induction model

In Figure 8.6 and Figure 8.7, we present calculated magnetic fields for a 100 km thick spherically symmetric model ionosphere with the derived conductivities $\sigma_P = 0.008$ S m^{-1}, $\sigma_H = 0.022$ S m^{-1} and $\sigma_\parallel = 80$ S m^{-1} (red lines) in comparison with magnetic field data of the flybys C-3 and C-9 (black lines). As a reference, the blue lines represent the induction response of a subsurface ocean which possesses the minimum conductivity to be considered a reasonable fit to the observations as discussed by Zimmer et al. (2000). These authors found that induced magnetic fields have been observed during the flybys C-3 and C-9 that can be explained by amplitudes of the induced magnetic field at Callisto's surface $\tilde{A}$ in the range of $\tilde{A} = 0.7 - 1.3$ for vanishing phase shifts ϕ, i.e., $\phi \approx 0°$. Thus, the blue lines in Figure 8.6 and Figure 8.7 represent the case $\tilde{A} = 0.7$ and $\phi = 0°$. In this regard, induction in our derived global ionosphere explains the observed magnetic field sufficiently well for flyby C-3, i.e., red lines in Figure 8.6 fit to the observations at least as well as the blue lines. Regarding flyby C-9, induction in the ionosphere causes amplitudes similar to the ones caused by the minimal required ocean. However, the associated characteristic of $B_{x'}$ possesses a spatial shift with regard to the magnetic field data.

In general, the characteristics of the ionosphere case (red lines in Figure 8.6 and Figure 8.7) are slightly shifted in comparison to the ocean case (blue lines). This shift is a result of the anisotropic conductivity tensor $\underline{\underline{\sigma}}(\underline{B}_p) = \underline{\underline{\sigma}}(\underline{B}_{cst} + \delta\underline{B})$ and the non-parallel alignment of $\underline{B}_{cst}$ ($\underline{B}_p$) and $\delta\underline{B}$. In the case of Callisto, the time-constant magnetic field $\underline{B}_{cst}$ is perpendicular to the inducing field $\delta\underline{B}$. For both configurations C-3 and C-9, the constant magnetic field $\underline{B}_{cst}$ is roughly five times smaller than the inducing magnetic field. However, since the constant field is non-zero and not directed into the direction of the time-variable inducing field, the inducing magnetic field and the primary magnetic field are not parallel aligned. Therefore, the plane perpendicular to the primary magnetic field, in which Pedersen currents flow, is inclined to the plane in which the loop electric field $\underline{E}^{\dot{B}}$ is induced. This inclination causes an inclination of the induced magnetic

dipole field and, hence, a spatial phase shift in magnetic fields seen along flyby trajectories.

This shift will be partly compensated if we include in addition to the conductive ionosphere a conductive subsurface layer which possesses an isotropic conductivity. As a case study, we present results of a setup including the ionosphere
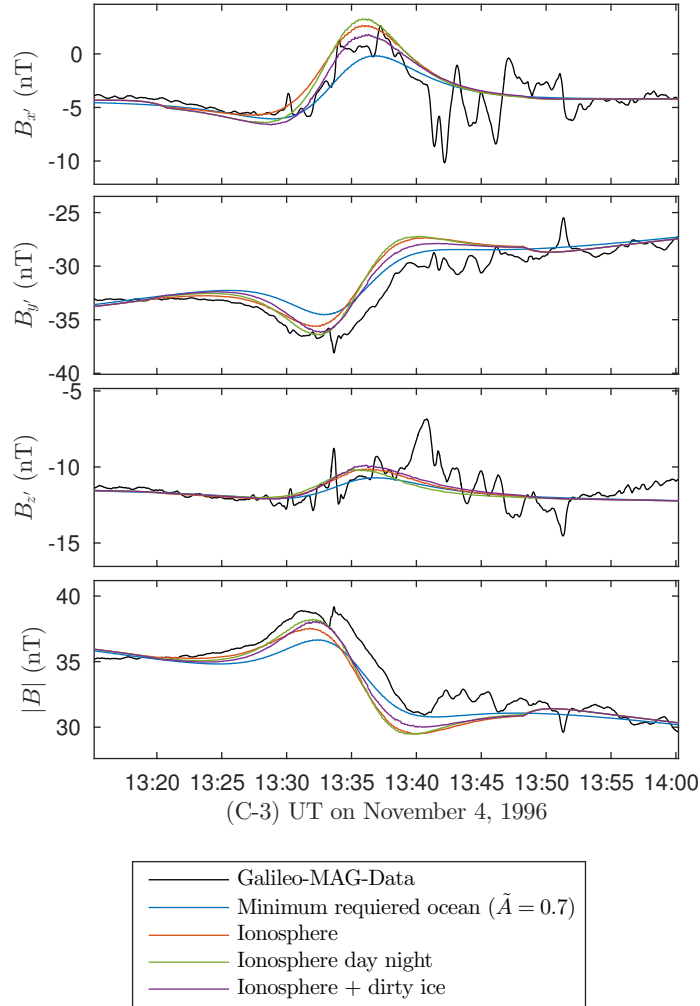
Figure 8.6: Magnetometer data during flyby C-3 (black line) in comparison with modeled magnetic field responses for a subsurface ocean that possesses a relative magnetic field amplitude of $\tilde{A} = 0.7$ and no phase shift $\phi = 0°$ at Callisto's surface (blue line), for a spherically symmetric ionosphere with $\sigma_P = 0.008$ S m^{-1}, $\sigma_H = 0.022$ S m^{-1} and $\sigma_{\parallel} = 80$ S m^{-1} (red line), for the associated asymmetric ionosphere that is four times more conductive at the day side than at the night side (solid green line) and for a spherically symmetric ionosphere plus a 300 km thick surface layer with a conductivity of 0.01 S m^{-1} representing dirty ice (purple line).
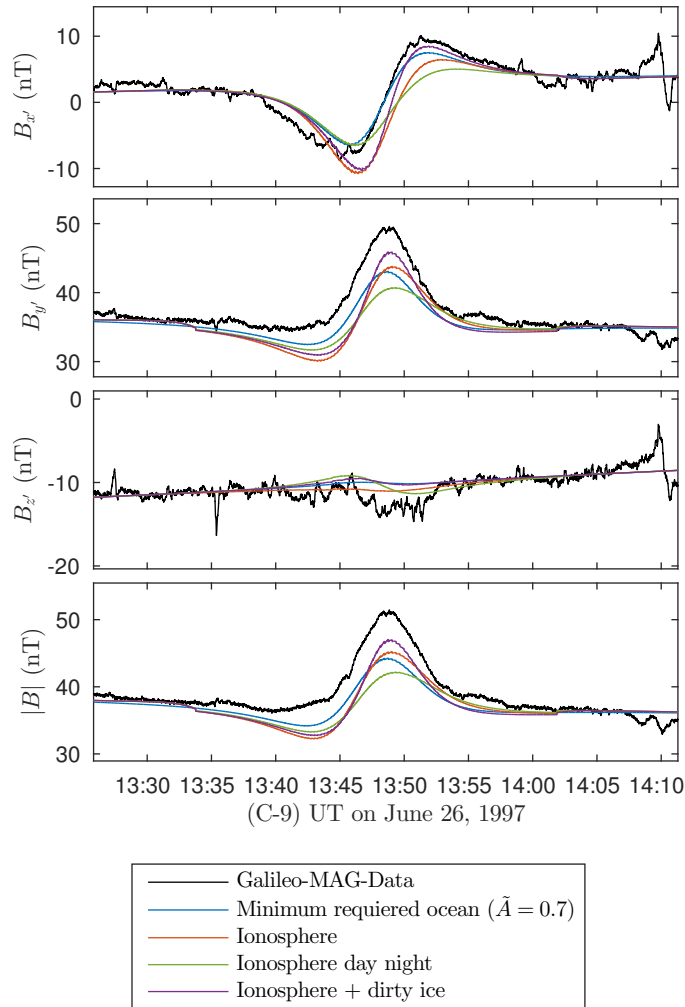
Figure 8.7: Magnetometer data during flyby C-9 (black line) in comparison to modeled magnetic fields with the same labeling as in Figure 8.6.

in combination with a 300 km thick surface shell with an electrical conductivity of 0.01 S m^{-1}. According to Neubauer (1998), this conductivity is roughly the maximal possible conductivity of 'dirty ice' (contaminated or partly molten water ice). Therefore, this case represents a solid interior with a maximal possible conductivity. The resulting magnetic field components are shown as purple lines in Figure 8.6 and Figure 8.7. In comparison with the 'ionosphere only' case, the amplitudes of the induced field are amplified by roughly 25%. Additionally, the fit of $B_{x'}$ for flyby C-9 is improved since the shift with respect to the observations is almost completely compensated.

We find very similar results as for this 'dirty ice' case, if we include in addition

to the ionosphere a highly conductive layer with an upper boundary at a depth of ∼450 km. Such a layer could represent a deeply lying subsurface ocean. Note that Zimmer et al. (2000) found a maximum possible upper ocean boundary at a depth of 270 km when considering no induction within Callisto's ionosphere. Hence, both flybys could be explained by a setup including a globally homogeneous ionosphere in combination with a weakly conductive surface layer or in combination with a deeply lying subsurface ocean.

However, Callisto's ionosphere is probably not globally homogeneous. The photoionization driven ionosphere possesses a day-night asymmetry. In order to illustrate the effect of such spatial inhomogeneities, we present another case study, where the ionosphere is assumed to be four times more conductive at the day side than at the nights side according to Equation (8.33) with an asymmetry factor $\kappa = 0.6$. For the conductivity tensor at the terminator $\underline{\underline{\sigma}}_0$ we use $\sigma_P = 0.008$ S m^{-1}, $\sigma_H = 0.022$ S m^{-1} and $\sigma_\parallel = 80$ S m^{-1} according to the symmetric case discussed above. With this asymmetric ionosphere, the ionospheric induction response possesses larger amplitudes regarding flyby C-3 (see green line in Figure 8.6). Therefore, this induction response fits better to the observations than in case of the spherically symmetric ionosphere. This amplification is due to the fact that the Galileo spacecraft passed by the day side of Callisto during flyby C-3, where the ionosphere is more conductive in this case study. However, the assumed day-night asymmetry of the conductivity worsens the fit to the observations in the case of flyby C-9 (green line in Figure 8.7), during which the Galileo spacecraft passed by the night side.

As a consequence of our case studies, magnetic induction within Callisto's ionosphere suffices to explain the magnetic field measurements seen during flyby C-3 while it does not suffice to completely explain the magnetic field measurements seen during flyby C-9. Therefore, an explanation of the C-9 observations likely requires the consideration of further processes such as Callisto's plasma interaction or induction within conductive subsurface layers.

8.4 Discussion of the induction model results

Our model results show that induction within Callisto's ionosphere plays a major role and needs to be considered when interpreting the magnetic field measurements

of the flybys C-3 and C-9. In the following, we address three questions in this regard:

1. Which role does plasma interaction play for the flybys C-3 and C-9?

2. How important is the anisotropic conductivity and in particular the Cowling channel effect regarding interpretations of flyby measurements?

3. How important is the ionospheric induction at the other Galilean moons?

8.4.1 The role of plasma interaction

Here, we discuss the role of the interaction of the magnetospheric plasma with Callisto's atmosphere-ionosphere system, i.e., the effects of the electric current driven by the motional electric field $\underline{E}^M$. As shown in Section 8.1.4, induction currents driven by this process are expected to be in the same order of magnitude as induction currents driven by $\underline{\dot{B}}$.

During flyby C-9, the Galileo spacecraft passed through the upstream magnetic pile up region with a closest approach altitude of 418 km. The magnetic fields generated by the plasma interaction and the induction fields are qualitatively different, but show similar magnetic field perturbations for the particular geometry of the C-9 flyby. The plasma interaction primarily drives quadrupole magnetic field perturbations near the moon while the induction due to the time-variable magnetic field primarily generates dipolar magnetic field perturbations. For flyby C-9, we expect that the pile up due to the plasma interaction causes an enhancement of the $B_{y'}$ component with a peak near the crossing of the trajectory through the '$y' = 0$' plane (occurring at time = 13:48:48 UT) and a sign reversal of the $B_{x'}$ component also near $y' = 0$ based on the symmetry of the interaction (see e.g., Neubauer (1999)). This crossing occurs near the time of closest approach (occurring at time = 13:47:51 UT). The structure of the plasma perturbations for this flyby is, thus, similar to induction in an isotropically conductive layer. Therefore, beside an isotropically conductive subsurface layer, the plasma interaction is also able to compensate the shift of the ionospheric induction response in $B_{x'}$, i.e., the red line in Figure 8.7. According to equation (45) in Neubauer (1998), we find that the plasma interaction driven perturbation of the $B_{y'}$ component is approximately 12 nT at the closest approach altitude of flyby C-9. Based on this estimate, the

plasma interaction could amplify the magnetic field perturbation from induction in the ionosphere by roughly 150% during this flyby. Therefore, the Galileo spacecraft likely measured a combined effect of induction and plasma interaction during flyby C-9 as also previously suggested by Seufert (2012) and Liuzzo et al. (2015). Particularly, this combined effect could explain the C-9 observation also in the likely case of a day-night asymmetry of Callisto's ionospheric conductivity.

For flyby C-3, the Galileo spacecraft passed through the downstream wake region with a closest approach altitude of 1136 km. The observations show an increased magnetic field strength, which can be mostly explained by induction in the ionosphere alone. It is therefore possible that the plasma interaction might not play a significant role along the C-3 trajectory, which would be consistent with the relative large distance of the closest approach. The electric currents driven by the plasma interaction generate in principal a decreased magnetic field on the downstream side, which is contrary to the observations. However, wake effects might additionally modify these magnetic field environment and partially compensate the decreased field. For instance, Saur et al. (2002) describe such wake effects for Io and Simon et al. (2012) for Rhea. These authors show that in case of a cold or dilute wake, pressure gradients form directed outwards to the wake boundaries. As a result, a diamagnetic current system establishes causing magnetic fields which are directed into the direction of the background magnetic field and enhance the magnetic field.

8.4.2 Significance of the Cowling channel effect

In the following, we discuss the enhancement effect due to the anisotropic conductivity using the example of flyby C-9. In Section 8.1, we have introduced and quantified the Cowling channel effects in Callisto's ionosphere and we have estimated its importance. In Figure 8.8, we illustrate the quantitative effect of the Cowling channel on Callisto's magnetic field environment for flyby C-9. Here, the green line represents the induction response of a spherically symmetric ionosphere with an anisotropic conductivity structure with $\sigma_P = 0.008$ S m^{-1}, $\sigma_H = 0.022$ S m^{-1} and $\sigma_\parallel = 80$ S m^{-1}. In this case, we artificially neglect the dependency of the conductivity tensor on the constant magnetic field component which is perpendicular to the inducing magnetic field, i.e., here $\underline{\sigma} = \underline{\sigma}(\delta \underline{B})$. In this way we avoid the additional effect of the inclined induced dipole, which is

also caused by the anisotropy as discussed in Section 8.3. The yellow line and the light blue line are model results for shells with an isotropic conductivity, but with the same structure as the model ionosphere with the anisotropic conductivity. The related isotropic conductivity is set to the Pedersen or the Hall conductivity which have been used in the anisotropic case, i.e., $\sigma_{iso} = 0.008$ S m^{-1} (solid yellow line) or $\sigma_{iso} = 0.022$ S m^{-1} (solid light blue line) respectively. In comparison, the induction response is much stronger in the anisotropic case (solid green line) than in the isotropic cases (solid yellow and solid light blue line). Therefore, neither the Pedersen conductivity nor the Hall conductivity can describe the anisotropic case in general.

In Section 8.1, we have introduced the effective conductivity of an anisotropic conductivity structure. We have shown that a good approximation of this effective conductivity of Callisto's ionosphere is given by the Cowling conductivity $\sigma_C = \sigma_P + \sigma_H^2/\sigma_P$ according to Equation (8.15) in the case, when the Alfvén conductance is much smaller than the Pedersen and Hall conductances. For the discussed ionosphere with conductivities $\sigma_P = 0.008$ S m^{-1} and $\sigma_H = 0.022$ S m^{-1}, the Cowling conductivity is $\sigma_C = 0.685$ S m^{-1}, which is approximately nine times larger than the associated Pedersen conductivity and three times larger than the associated Hall conductivity.

To illustrate the impact of the effective conductivity, Figure 8.8 shows the induction response of a shell, where the isotropic conductivity is set to the Cowling conductivity, i.e., $\sigma_{iso} = \sigma_C = 0.685$ S m^{-1} (dashed purple line). We see that for the anisotropic conductivity tensor $\underline{\underline{\sigma}} = \underline{\underline{\sigma}}(\delta\underline{B})$, the induction response of the anisotropic structure (green line) is very similar to the induction response of the isotropic structure possessing the associated Cowling conductivity (dashed purple line) as we also expect from our analytic model discussed in Section 8.1. For the more realistic case $\underline{\underline{\sigma}} = \underline{\underline{\sigma}}(\underline{B}_p)$ where $\underline{B}_p$ is not parallel to $\delta\underline{B}$, ionospheric induction signals (red line in Figure 8.8) are spatially shifted with respect to the case where we assumed $\underline{\underline{\sigma}} = \underline{\underline{\sigma}}(\delta\underline{B})$ and with respect to the observed magnetic field. This discrepancy with regard to the observations suggests that other effects such as induction in a subsurface layer (dirty ice or water ocean) and the plasma interaction play an important role in the case of flyby C-9 (see discussions in Section 8.3 and Section 8.4.1). Moreover, this example shows explicitly that an ionosphere with anisotropic conductivity structure can only

be approximated to some extend by a shell with an isotropic conductivity. Such an approximation is useful for the estimation of the magnitude of the expected magnetic field perturbation. We use this approximation in the following Section 8.4.3 to estimate the strength of ionospheric induction currents at the other Galilean moons. However, in case of complex magnetic field configuration and for the purpose of detailed interpretations of spacecraft magnetometer data, the ionospheric conductivity anisotropy has to be included into model calculations.
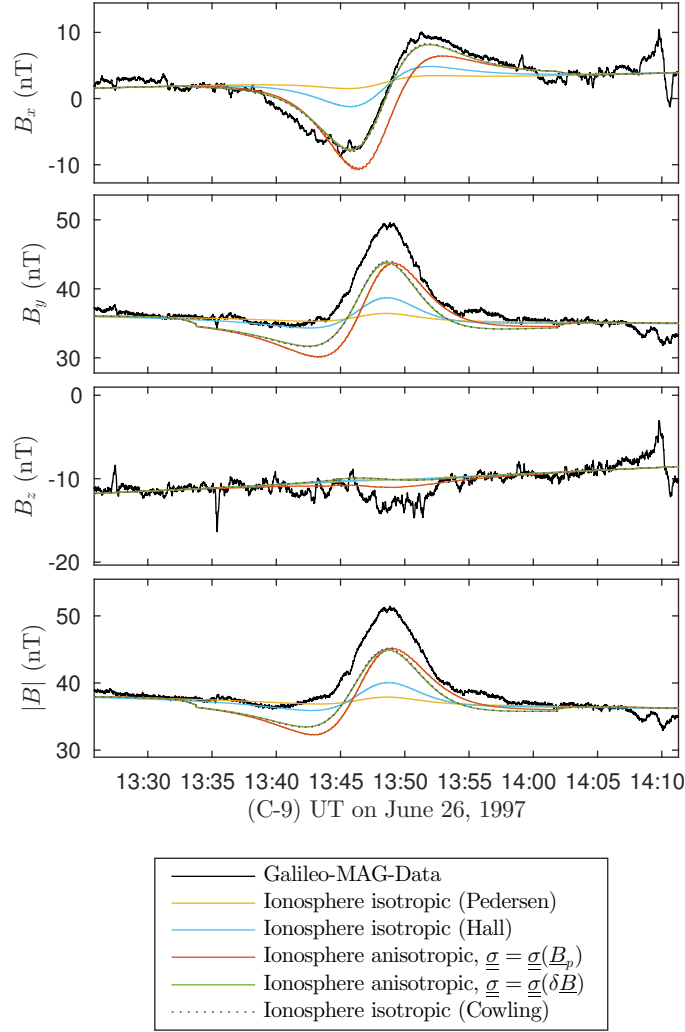
Figure 8.8: Induction signatures of shells with $\underline{\underline{\sigma}} = \underline{\underline{\sigma}}(\underline{B}_p)$ (solid red line) and with $\underline{\underline{\sigma}} = \underline{\underline{\sigma}}(\delta\underline{B})$ (solid green line) in comparison with shells with isotropic conductivity. Used Pedersen, Hall and Cowling conductivities are $\sigma_P = 0.008$ S m^{-1}, $\sigma_H = 0.022$ S m^{-1} and $\sigma_C = 0.685$ S m^{-1}. Galileo magnetometer data during flyby C-9 is shown as black line.

	Io	Europa	Ganymede	Callisto
Σ_A [S]	4.4	4.9	4.2	12
*Σ_P [S]	200	30	2	800
*Σ_H [S]	150	10	0.1	2200
Σ_{eff}^r [S]	3.2	1.4	0.07	32
Σ_{eff} [S]	310	33	2	6850
Σ_{ocean} [S]	2.0×10^4	5.0×10^4	1.0×10^4	5.0×10^4
$\tilde{A}_{iono}$	0.05	0.004	4×10^{-4}	0.83
ϕ_{iono}	-78°	-90°	-90°	-40°
$\tilde{A}_{ocean}$	0.85	0.88	0.82	0.9
ϕ_{ocean}	-22°	-11°	-29°	-7°

Table 8.2: Average Alfvén (Σ_A), Pedersen (Σ_P) and Hall (Σ_H) conductances for Io, Europa and Ganymede taken from Kivelson et al. (2004) and in case of Callisto taken from this study (see Section 8.2.2); Associated effective conductances Σ_{eff} and Σ_{eff}^r according to Equations (8.15) and (8.16); Conductances of subsurface oceans Σ_{ocean} as discussed for Io by Khurana et al. (2011), for Europa by Schilling et al. (2007), for Ganymede by Saur et al. (2015) and for Callisto by Seufert (2012). Amplitudes $\tilde{A}_{iono}$ and phases ϕ_{iono} of induced magnetic field at the moon's surface due to induction within the ionosphere with $\tilde{A}$ ranging from 0 (approximately insulator) to 1 (perfect conductor) and ϕ ranging from -90° (delayed in time) to 0° (in-phase with the inducing field) (e.g., Zimmer et al., 2000); Amplitudes $\tilde{A}_{ocean}$ and phase shifts ϕ_{ocean} of induced magnetic fields due to induction in a subsurface ocean. *In case of a spherical shell, the ionospheric conductances relevant for induction Σ_P and Σ_H need to be derived from an integration of the conductivities along the radial extend of the conductive shell. Here, we use such conductances only for Callisto as derived in Section 8.2.2. However, for a first-order estimation of ionospheric induction at the other Galilean moons, known conductances of Io, Europa and Ganymede suffice, which have been derived by integrations along the magnetic field.

8.4.3 Induction in ionospheres of other Galilean moons

Induction due to the time-variable Jovian magnetic field will also occur in the ionospheres of the other Galilean moons. For a first-order estimation of the relative importance of induction, we treat the ionospheres as shells with an isotropic effective conductance derived from Equation (8.15) and assume an ionosphere thickness of 100 km at all moons.

Table 8.2 lists effective ionospheric conductances and the conductances associated with expected subsurface oceans. Further, we compare in Table 8.2 resulting amplitudes $\tilde{A}$ at the surfaces of the moons and phase shifts ϕ of the induced magnetic fields. We provide these values for both subsurface oceans ($\tilde{A}_{oceans}, \phi_{oceans}$)

and ionospheres ($\tilde{A}_{iono}, \phi_{iono}$). For Io, we considered the magma ocean argued to exist by Khurana et al. (2011) based on modeling of Galileo magnetic field measurements. From an analysis of Hubble Space Telescope observations, the existence of the magma ocean was, however, put into question by Roth et al. (2017). For the other icy moons, we assume a saline subsurface water ocean as the internal conductive layer.

Based on $\tilde{A}_{ocean}$ we estimate the properties of induction within an ionosphere. We find that the contribution of the ionospheric induction compared to the maximum possible induction inside the moon is $\sim$5% at Io, $\sim$0.4% Europa, $\sim$0.04% at Ganymede and $\sim$80% at Callisto. Hence, ionospheric induction seems to play a negligible role at Ganymede. The reason for this are Ganymede's small ionospheric conductances that are caused by Ganymede's internal dynamo magnetic field. However, ionospheric induction should be considered at Io, maybe also at Europa and certainly at Callisto when details of the moons' interior conductivity structure are derived from magnetic field measurements.

9 Summary and conclusions

The first objective of this study has been to constrain density and structure of Callisto's atmosphere based on available observations. For this purpose, we use a local model for the electron energy distribution function at every location in Callisto's atmosphere to jointly explain the ionosphere observations by Kliore et al. (2002) and the atmospheric UV emission observed by Cunningham et al. (2015). Using our model, we characterize the density and structure of the O_2-component in Callisto's atmosphere and the electron density. We derive an average O_2 column density of $2.1^{+1.1}_{-1.1} \times 10^{19}$ m^{-2} in agreement with the HST/COS obervations from November 17, 2011. As a result, Callisto's atmosphere is expected to be optically thin and O_2-dominated, which is in agreement with the findings of Cunningham et al. (2015) regarding the O_2 atmosphere. A subsolar-terminator asymmetric O_2 atmosphere with a maximum O_2 column density at the subsolar point significantly improves the synchronous fitting with the OI $\lambda135.6$ nm emission observation of Cunningham et al. (2015) and the electron density observation of Kliore et al. (2002). Our model predicts that the O_2 column density is about 0.4×10^{19} m^{-2} at the terminator and the associated subsolar O_2 column density is in the range of $2.4 - 9.8 \times 10^{19}$ m^{-2}. In fact, our analysis of the radio occultation observations of Kliore et al. (2002) shows that the terminator O_2 density could be in principle zero corresponding to an infinite subsolar-terminator asymmetry. However, under the consideration of neutral winds lower values of the derived O_2 asymmetries are much more likely than larger values. Therefore, it is very unlikely that the O_2 density vanishes at the terminator. Moreover, we will find smaller asymmetries of the O_2 atmosphere if we prescribe smaller terminator CO_2 column densities according to the observational error range of the atmospheric CO_2 density from Carlson (1999).

Further, we find that the detailed atmospheric composition crucially affects the suprathermal electron energy distribution function and the associated UV emission intensity. We calculate that on average one OI $\lambda135.6$ nm photon is emitted per every 170 electron ion pairs generated and per every 60 electron ion pairs produced by secondary electron impact ionization. The relative abundance of H_2O strongly affects the electron density. In contrast to the case of O_2 and CO_2

molecules, electron cooling by rotational state excitation of H_2O molecules plays an important role in the thermal electron energy range. If the relative abundance of H_2O is larger than 4%, this cooling mechanism will cause more rapid cooling of the thermal electrons leading to increased dissociative recombination and lower electron densities.

The current ionosphere model lacks the effect of electron transport and the interaction between Callisto and the upstreaming magnetospheric plasma. These factors might also play a role regarding spatial and temporal variations of atmosphere and ionosphere. Note that electron transport is affected by particle collisions and the electromagnetic field environment of Callisto, which is modified by the interaction of Callisto with the magnetospheric plasma.

The second objective of this study has been to determine the impact of possible atmospheric sources on the time-variability of the atmosphere ionosphere system and potential observations. Based on our results from the ionosphere modeling, we suppose that Callisto's O_2 atmosphere consists of a dense subsolar region and a less dense terminator region. This asymmetry could be driven by a surface sputtering driven atmosphere and the asymmetry of this source process, i.e., effective surface sputtering on the day side and less effective surface sputtering on the night side where the sputtering efficiency is suppressed due to the lower surface ice temperatures. Comparisons between our ionosphere model results and radio occultation and HST/COS observations support the hypothesis of Kliore et al. (2002) that Callisto's atmospheric density is larger at western elongation when magnetospheric particles predominately impinge on the day side than at eastern elongation when magnetospheric particles predominately impinge on the night side. This hypotheses can be generalized by the hypotheses that Callisto's atmospheric O_2 density varies with the orbital phase similar to what is expected at Europa according to Plainaki et al. (2013). In order to test this hypothesis we predict HST/COS observations of the atmospheric OI $\lambda135.6$ nm emission intensity for different orbital phases of Callisto. As basis of this predictions, we use the Europa atmosphere model of Plainaki et al. (2013) and an associated parametrization of this model by Milillo et al. (2016). We rescale the densities of this model to the expected densities of Callisto's atmosphere using the existent atmospheric OI $\lambda135.6$ nm emission observation from Cunningham et al. (2015). On the basis of our calculations, we will expect four times larger OI $\lambda135.6$ nm emission

intensities at western elongation than at eastern elongation if surface sputtering is the dominant atmospheric source process and creates an orbital phase dependent density variation. Otherwise, if the atmosphere formation is predominately driven by sublimation, we will not expect an orbital phase dependency of Callisto's airglow at the 135.6 nm wavelength.

The third objective of this study has been to determine the importance of electromagnetic induction in Callisto's ionosphere with respect to the magnetic field measurements of the Galileo flybys C-3 and C-9, which have been interpreted as evidence for induction within a subsurface ocean. Based on our ionosphere model, we construct a conductivity model of Callisto's ionosphere and calculate the induction due to the external time-variable magnetic field of Jupiter. Our results show that this induction process significantly contributes to the magnetic field perturbations seen during the Galileo flybys C-3 and C-9. We find that the anisotropic conductivity of the ionosphere plays an important role since it causes an incomplete Cowling channel creating ionospheric induction responses that are stronger than expected from the sole consideration of Pedersen and Hall conductances. Since the magnetic field measurements from the flybys C-3 and C-9 have been previously interpreted as evidence for a subsurface saline water ocean, we have to ask the question, what are the implications of our study on this possible subsurface ocean?

Our results show that the magnetic fields seen during flyby C-3 can solely be explained by induction within Callisto's ionosphere. Particularly, a likely ionospheric day-night asymmetry is in agreement with the observations. Conductive subsurface layers can not be ruled out but are not required to explain the magnetic fields seen during this flyby. It appears that the plasma interaction might have only played a minor role during this flyby. However, to obtain a better understanding of flyby C-3, the role of plasma interaction requires further investigations and modeling studies.

Our results also show that a major part of the magnetic fields seen during flyby C-9 can be explained by induction within Callisto's ionosphere. For flyby C-9, Callisto's plasma interaction is expected to be an additional important process amplifying the induction response since it generates qualitatively similar magnetic field perturbations compared to the induction response in this case. However, a day-night asymmetry of Callisto's ionosphere weakens the response of

both ionospheric induction and plasma interaction. Induction in an additional 300 km thick surface layer of dirty ice or a deeply lying subsurface ocean is a possible mechanism which amplifies the ionospheric induction response such that a good agreement with the observations is achieved also in case of an asymmetric ionosphere. To obtain a better understanding of flyby C-9 and its implications on Callisto's subsurface, the associated plasma interaction and, in particular the degree of Callisto's ionospheric day-night asymmetry needs further investigations.

We come to the conclusion that induction within Callisto's ionosphere plays a major role and need to be considered when modeling Callisto's magnetic field and plasma environment. Particularly, it needs to be considered when deriving properties of the electrically conductive structure in the moon's interior. We can think of possible scenarios where the day-night asymmetry of Callisto's ionospheric conductivity is not too strong (on the order of 4:1) and the plasma interaction enhances the magnetic field for the C-9 flyby in addition to the induction fields and has little importance during the C-3 flyby. In this case, the effect of ionospheric induction currents puts the existence of a subsurface water ocean into question. However, if the magnetic field measurements by the Galileo spacecraft can be explained without a subsurface ocean, the ocean might still exist. If induction within the ionosphere generates an induction response near saturation, additional induction in a subsurface ocean will be simply 'barely visible' anymore. Based on the current uncertainties about Callisto's night side ionosphere, the existence of 'dirty ice' and its conductivity, and the plasma interaction, it is difficult to draw rigorous conclusions about a subsurface ocean at Callisto. Our results show that such an ocean could be located significantly deeper as previously thought. It might even not be necessary at all to explain the Galileo magnetic field measurements for a certain set of conditions for Callisto's ionosphere and its plasma interaction. Further modeling will help to better understand these conditions.

Finally we state that the future in-situ and remote sensing measurements of Callisto's plasma and magnetic field environment taken by the JUICE spacecraft and future HST observation will be most important for constraining Callisto's global atmosphere-ionosphere system and its interior structure. We hope that our findings can help to interpret and understand these coming observations.

A Ionosphere model: chemical reaction time scales

In order to evaluate the assumption that O_2^+ is the dominant ion species, we analyze time scales of chemical reactions of CO_2^+ and H_2O^+ with O_2 forming O_2^+. Figure A.1 shows a comparison of associated ion-neutral loss time scales with ion transport (diffusion) time scales for CO_2^+ and H_2O^+. The chemical time scales are approximated using

$$\tau_{chem}^{CO2+} = [k_{c1}\, n_{O2}(z)]^{-1} ,$$ (A.1)

$$\tau_{chem}^{H2O+} = [k_{c2}\, n_{O2}(z)]^{-1}$$ (A.2)

with $k_{c1} = k(CO_2^+ + O_2 \rightarrow O_2^+ + CO_2)= 5.3 \times 10^{-17}$ m^3 s^{-1} (Copp et al., 1982), $k_{c2} = k(H_2O^+ + O_2 \rightarrow O_2^+ + H_2O)= 4.6 \times 10^{-16}$ m^3 s^{-1} (Rakshit and Warneck, 1980), $n_{O2}(z) = 0.66 \times 10^{15} \exp(-z/H)$ m^{-3} with the altitude z and the scale height H of 30 km, according to the findings of this study.
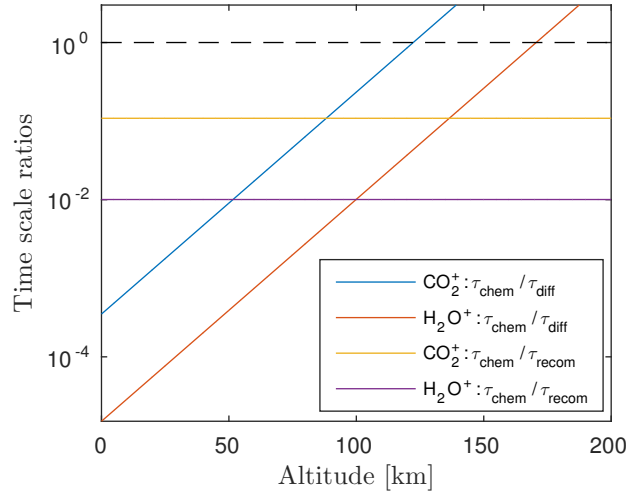
Figure A.1: Ion neutral loss time scales forming O_2^+ over ion diffusion time scales for CO_2^+ (blue line) and H_2O^+ (red line). Ion neutral loss time scales forming O_2^+ over recombination time scales for CO_2^+ (yellow line) and H_2O^+ (purple line).

The ion diffusion time scale is estimated using

$$\tau_{diff} = \frac{H_i^2}{D_i} = \frac{k_B(T_i + T_e)\nu_{in}}{m_i g(z)^2} \approx 10^{-15} \frac{k_B(T_e + T_i)(R_C + z)^4}{G^2 M_C^2 m_i} n_n(z) \; , \qquad \text{(A.3)}$$

where we set the ion scale height H_i to the neutral scale height of 30 km, D_i denotes the ion diffusion coefficient, T_i the ion temperature and T_e the electron temperature which both are set to 300 K, m_i the ion mass, $g(z)$ the altitude dependent gravity acceleration, G the gravitational constant and M_C Callisto's mass: $M_C = 1.076 \times 10^{23}$ kg . The ion neutral collision frequency ν_{in} is set to $\nu_{in} = 1.0 \times 10^{-15} \, n_n(z)$ m^3 s^{-1} (Banks and Kockarts, 1973) with the neutral density altitude dependency $n_n(z) = 1.2 \times 10^{15} \exp(-z/H)$ m^{-3} according to the findings of this study.

Recombination time scales are estimated using

$$\tau_{recom}^{CO2+} = [k_{r1} \, n_e(z)]^{-1} \; , \qquad \text{(A.4)}$$

$$\tau_{recom}^{H2O+} = [k_{r2} \, n_e(z)]^{-1} \qquad \text{(A.5)}$$

with $k_{r1} = k(CO_2^+ + e \rightarrow CO + O) = 3.8 \times 10^{-13}(T_e/300K)^{-0.5}$ m^3 s^{-1} (Brian and Mitchell, 1990), $k_{r2} = k(H_2O^+ + e \rightarrow OH + H + H) = 3.05 \times 10^{-13}(T_e/300K)^{-0.5}$ m^3 s^{-1} (Rosén et al., 2014), $n_e(z) \approx 1.0 \times 10^{10} \exp(-z/H_e)$ m^{-3}, H_e the electron scale height which is set to the neutral scale height of 30 km and the electron temperature T_e approximated by 300 K.

For the major part of the atmosphere where O_2 is not expected to be significantly less dense than H_2O, the above estimation shows that the dominant ion is O_2^+ and the equilibrium of ion chemistry is reached sufficiently fast.

B Ionosphere model: numerical implementation

The numerical solution of the coupled equations (6.1) - (6.5) is achieved in the following way: As a first step we approximate the ion density $n_{i,1}^{(0)}$ and the electron density $n_e^{(0)}$ by a simple chemical equilibrium model using a starting electron temperature of $T_e^{(0)} = 300$ K:

$$n_e^{(0)} = n_{i,1}^{(0)} = \sqrt{\frac{\sum_s \int_0^{\hat{E}} P_{e,s}(E)\,\mathrm{d}E}{\alpha(T^{(0)})}}\ . \tag{B.1}$$

Using these first approximations of $n_{i,1}$ and n_e and a reasonable guess of the transition energy E_t in the order of ~ 1 eV, we can treat equation (6.1) as an inhomogeneous linear integral equation of type 2 in order to calculate the suprathermal electron energy distribution function $F_{\text{sup}}^{(0)}(\text{E})$. There is no general solution of this type of equation. Therefore, the method presented below is only valid for this specific problem.

For a fixed location, the solution of equation (6.1) is found recursively using

$$
\begin{aligned}
F_{\text{sup}}^{(0)}(E) = E^{-1/2} &\left(n_e \sigma_{ee}(E, n_e, T_e) + n_{i,1}\sigma_{rec,1}(E) + \sum_s^{N_n} n_{n,s} \sum_{t_s=1}^{T_s} \sigma_{st_s}(E) \right)^{-1} \\
&\times \left[\sum_s^{N_n} \left(P_{e,s}(E)\sqrt{\frac{m_e}{2}} + n_{n,s} \int_{I_s}^{\hat{E}} \mathrm{d}\tilde{E}\ \sqrt{E + \tilde{E}} \right.\right. \\
&\times \left(\sigma_{I,s}(E + \tilde{E}, E) + \sigma_{I,s}(E + \tilde{E}, \tilde{E} - I) \right) F(E + \tilde{E}) \\
&+ \left. n_{n,s} \sum_{t_s=1}^{T_s-1} \sqrt{E + \epsilon_{st_s}}\ \sigma_{st_s}(E + \epsilon_{st_s}) F(E + \epsilon_{st_s}) \right) \\
&+ \left. n_e\ \sqrt{E + \Delta E}\ \sigma_{ee}(E, n_e, T_e)\ F(E + \Delta E) \right]\ .
\end{aligned}
\tag{B.2}
$$

Starting at the maximum energy E_{max} which photoelectrons can have, we subse-

quently calculate the number of electrons of the energy level below. Note that for a photoionization driven ionosphere an effective upper limit of $E_{\max}$ is given by the nature of the solar spectrum. The described procedure is possible since our model only considers degradation of suprathermal electrons to lower energy levels, as no acceleration processes are present.

Using the resulting distribution function, we calculate all production and heating terms of the fluid equations (6.2), (6.3) and (6.4) according to equations (6.6), (6.15) - (6.21), (6.30) and (6.31). The coupled non-linear fluid equations are solved numerically using a standard Newton-Method ensuring the quasi neutrality condition and yielding new electron densities $n_e^{(1)}$, ion densities $n_{i,1}^{(1)}$ and electron temperatures $T_e^{(1)}$.

We use this new set of $(n_e^{(1)}, n_{i,1}^{(1)}, T_e^{(1)})$ as new starting values to evaluate the suprathermal electron energy distribution function again. The whole process is repeated until the full set of variables $(F_{\sup}^{(i)}(E), n_{i,1}^{(i)}, n_e^{(i)}, T_e^{(i)})$ converges after several iteration steps when i becomes sufficiently large.

A second iteration process can then be applied varying the transition energy E_t until thermal and suprathermal electron energy distribution functions perfectly match at E_t. However, comprehensive tests have revealed that the macroscopic observables electron density, electron temperature and UV emission intensity are very robust with respect to the choice of the transition energy as expected from Hoegy (1984). Within the possible transition energy range of 0.1-5 eV, electron densities vary less than 2%, electron temperatures vary less than 5% and UV emission intensities vary less than 1%. Therefore, we choose a fixed transition energy of 1 eV for all volume elements to improve the computational performance.

For the calculation of the suprathermal electron energy distribution function, we choose an energy resolution of 0.01 eV as a trade-off of the smallest discrete energy loss ϵ_{min} and the computational efficiency. For the purpose of computational performance, we approximate processes with an discrete energy loss smaller than 0.01 eV by an energy loss of 0.01 eV and a simultaneous rescaling of the associated cross sections according to the method of Swartz (1985). Rotational state excitation is treated in this way (see caption of Table 6.1).

The lower boundary of the simulation energy domain is set to E_t while the upper boundary of the simulated energy domain is set 100 eV since only a negligible amount of photoelectrons is produced above 100 eV.

List of Figures

List of Tables

Bibliography

Allan, M. (1995), Measurement of absolute differential cross sections for vibrational excitation of O2 by electron impact, *Journal of Physics B: Atomic, Molecular and Optical Physics*, *28*(23), 5163–5175, doi:10.1088/0953-4075/28/23/021.

Anderson, J. D., G. Schubert, R. A. Jacobson, E. L. Lau, W. B. Moore and W. L. Sjorgen (1998), Distribution of Rock, Metals, and Ices in Callisto, *Science*, *280*, 1573–1576, doi:10.1126/science.280.5369.1573.

Anderson J. D., R. A. Jacobson, T. P. McElrath, W. B. Moore, G. Schubert and P. C. Thomas (2001), Shape, Mean Radius, Gravity Field, and Interior Structure of Callisto, *Icarus*, *153*, 157–161, doi:10.1006/icar.2001.6664.

Anzai, K., H. Kato, M. Hoshino, H. Tanaka, Y. Itikawa, L. Campbell, M. J. Brunger, S. J. Buckman, H. Cho, F. Blanco, G. Garcia, P. Limão-Vieira and O. Ingólfsson (2012), Cross section data sets for electron collisions with H_2, O_2, CO, CO_2, N_2O and H_2O, *The European Physical Journal D: Atomic, Molecular, Optical and Plasma Physics*, *66*(2), 1–8, doi:10.1140/epjd/e2011-20630-1.

Ashihara, O. and K. Takayanagi (1974), Velocity distribution of ionospheric low-energy electrons, *Planetary and Space Science*, *22*(8), 1201–1217, doi:10.1016/0032-0633(74)90005-1.

Banks, P. M. and G. Kockarts (1973), *Aeronomy*, Academic, San Diego, California.

Baumjohann, W. and R. A. Treumann (2012), *Basic Space Plasma Physics, Revised Edition*, Imperial College Press, London, United Kingdom.

Berger, M., and M. S. Seltzer (1970), Energy deposition by auroral electrons in the atmosphere, *Journal of Atmospheric and Terrestrial Physics*, *32*(6), 1015–1045, doi:10.1016/0021-9169(70)90115-7.

Brian, J. and A. Mitchell (1990), The dissociative recombination of molecular ions, *Physics Reports*, *186*(5), 215–248, doi:10.1016/0370-1573(90)90159-Y.

Butler, S. T. and M. J. Buckingham (1962), Energy Loss of a Fast Ion in a Plasma, *Physical Review*, *126*(1), 1–4, doi:10.1103/PhysRev.126.1.

Carlson, R. W. (1999), A tenuous carbon dioxide atmosphere on Jupiter's moon Callisto, *Science*, *283*(5403), 820–821, doi:10.1126/science.283.5403.820.

Cassen, P., S. J. Peale and R. T. Reynolds (1980), On the comparative evolution of Ganymede and Callisto, *Icarus*, *41*, 232–239, doi:10.1016/0019-1035(80)90006-8.

Chen, R. H. and A. F. Nagy (1978), A comprehensive model of the Venus ionosphere, *Journal of Geophysical Research: Space Physics*, *83*(A3), 1133–1140, doi:10.1029/JA083iA03p01133.

COMSOL Multiphysics® (2013), AC/DC Module User's Guide for COMOSOL 4.2a, Stockholm, Sweden: COMOSOL AB.

Copp, N. W., M. Hamdan, J. D. C. Jones, K. Birkinshaw and N. D. Twiddy (1982), A selected ion flow tube study of the reactions of the gaseous ion CO_2^+ at 298 K, *Chemical Physics Letters*, *88*(5), 508–511, doi:10.1016/0009-2614(82)83164-3.

Cowling, T. G. (1932), Magnetism, Solar: The electrical conductivity of an ionised gas in the presence of a magnetic field, *Monthly Notices of the Royal Astronomical Society*, 93, 90–97, doi:10.1093/mnras/93.1.90.

Cravens, T. E. and A. Korosmezey (1986), Vibrational and Rotational Cooling of Electrons by Water Vapor, *Planetary and Space Science*, *34*(10), 961–970, doi:10.1016/0032-0633(86)90005-X.

Cunningham N. J., J. R. Spencer, P. D. Feldman, D. F. Strobel, K. France and S. N. Osterman (2015), Detection of Callisto's Oxygen Atmosphere with the Hubble Space Telescope, *Icarus*, *254*, 178–189, doi:10.1016/j.icarus.2015.03.021.

Dalgarno, A. (1969), Inelastic collisions at low energies, *Canadian Journal of Chemistry*, *47*(10), 1723–1729, doi:10.1139/v69-284.

Demtröder, W. (2006), *Atoms, Molecules and Photons*, Springer, Berlin, Heidelberg.

Famá, M., J. Shi and R. A. Baragiola (2008), Sputtering of ice by low-energy ions, *Surface Science*, *602*(1), 156–161, doi:10.1016/j.susc.2007.10.002.

Goff, J. A. and S. Gratch (1946), Low-pressure properties of water from -160 to 212 F, *In Transactions of the American society of heating and ventilating engineers*, *52*, 95–122.

Greeley, R., J. E. Klemaszewski and R. Wagner (2000), Galileo views of the geology of Callisto, *Planetary and Space Science*, *48*, 829–853, doi:10.1016/S0032-0633(00)00050-7.

Gurnett, D. A., A. M. Persoon, W. S. Kurth, A. Roux and S. J. Bolton (2000), Plasma densities in the vicinity of Callisto from Galileo plasma wave observations, *Geophysical Research Letters*, *27*(13), 1867–1870, doi:10.1029/2000GL003751.

Hall, D. T., D. F. Strobel, P. D. Feldman, M. A. McGrath and H. A. Weaver (1995), Detection of an oxygen atmosphere on Jupiter's moon Europa, *Nature*, *373*, 677–679, doi:10.1038/373677a0.

Hanel, R., B. Conrath, M. Flasar, L. Herath, V. Kunde, P. Lowman, W. Maguire, J. Pearl, J. Pirraglia, R. Samuelson, D. Gautier, P. Gierasch, L. Horn, S. Kumar and C. Ponnamperuma (1979), Infrared observations of the Jovian system from Voyager 2, *Science*, *206*(4421), 952–956, doi:10.1126/science.206.4421.952.

Hartkorn, O., J. Saur, and D. F. Strobel (2017), Structure and density of Callisto's atmosphere from a fluid-kinetic model of its ionosphere: Comparison with Hubble Space Telescope and Galileo observations, *Icarus*, 282, 237–259, doi:10.1016/j.icarus.2016.09.020.

Hartkorn, O. and Saur, J. (2017), Induction signals from Callisto's ionosphere and their implications on a possible subsurface ocean, *Submitted to Journal of Geophysical Research: Space Physics* in April 2017

Hill. T. W., A. J. Dessler, and C. K. Goertz (1983), Magnetospheric models, in *Physics of the Jovian Magnetosphere*, edited by A. J. Dessler, pp. 353–394, Cambridge University Press, Cambridge.

Hoegy, W. R. (1984), Thermal electron heating rate: A derivation, *Journal of Geophysical Research: Space Physics*, *89*(A2), 977–985, doi:10.1029/JA089iA02p00977.

Huntress, W. T. and R. F. Pinizzotto (1973), Product distributions and rate constants for ion-molecule reactions in water, hydrogen sulfide, ammonia, and methane, *The Journal of Chemical Physics*, *59*(9), 4742–4756, doi:10.1063/1.1680687.

Hwang, W., Y. K. Kim and M. Eugene Rudd (1996), New model for electron-impact ionization cross sections of molecules, *The Journal of Chemical Physics*, *104*(8), 2956–2966, doi:10.1063/1.471116.

Itikawa, Y. (2002), Cross Sections for Electron Collisions with Carbon Dioxide, *Journal of Physical and Chemical Reference Data*, *31*(3), 749–768, doi:10.1063/1.1481879.

Itikawa, Y. (2005), Cross Sections for Electron Collisions with Water Molecules, *Journal of Physical and Chemical Reference Data*, *34*(1), 1–22, doi:10.1063/1.1799251.

Itikawa, Y. (2009), Cross Sections for Electron Collisions with Oxygen Molecules, *Journal of Physical and Chemical Reference Data*, *38*(1), 1–20, doi:10.1063/1.3025886.

Jasperse, J. R. (1976), Boltzmann-Fokker-Planck model for the electron distribution function in the Earth's ionosphere, *Planetary and Space Science*, *24*(1), 33–40, doi:10.1016/0032-0633(76)90058-1.

Jasperse, J. R. (1977), Electron distribution function and ion concentrations in the earth's lower ionosphere from Boltzmann-Fokker-Planck theory, *Planetary and Space Science*, *25*(8), 743–756, doi:10.1016/0032-0633(77)90126-X.

Johnson, R. E. (1990), *Energetic charged-particle interactions with atmospheres and surfaces (Vol. 19)*, Springer, Berlin, Heidelberg.

Johnson, R. E., R. W. Carlson, J. F. Cooper, C. Paranicas, M. H. Moore, M. C. Wong (2004), Radiation Effects on the Surfaces of the Galilean Satellites in *Jupiter: The Planet, Satellites and Magnetosphere*, edited by F. Bagenal, T. E. Dowling and W. B. McKinnon, pp. 457–484, Cambridge University Press, Cambridge.

Kanik, I., C. Noren, O. P. Makarov, P. Vattipalle and J. M. Ajello (2003), Electron impact dissociative excitation of O_2: 2. Absolute emission cross sections of the OI(130.4 nm) and OI(135.6 nm) lines, *Journal of Geophysical Research*, *108*(E11), 5126, doi:10.1029/2000JE001423

Khurana, K. K., M. G. Kivelson and C. T. Russell (1997), Interaction of Io with its torus: Does Io have an internal magnetic field?, *Geophysical Research Letters*, 24, 2391–2394, doi:10.1029/97GL02507.

Khurana, K. K., M. G. Kivelson, D. J. Stevenson, G. Schubert, C. T. Russel, R. J. Walker and C. Polanskey (1998), Induced magnetic fields as evidence for subsurface oceans in Europa and Callisto, *Nature*, *395*, 777–780, doi:10.1038/27394.

Khurana, K. K., M. G. Kivelson, V. M. Vasyliunas, N. Krupp, J. Woch, A. Lagg, B. H. Mauk and W. S. Kurth (2004), The configuration of Jupiter's magnetosphere in *Jupiter: The planet, satellites and magnetosphere*, edited by F. Bagenal, T. E. Dowling and W. B. McKinnon, pp. 593–616, Cambridge University Press, Cambridge.

Khurana, K. K., X. Jia, M. G. Kivelson, F. Nimmo, G. Schubert and C. T. Russell (2011), Evidence of a Global Magma Ocean in Io's Interior, *Science*, *332*, 1186–1189, doi:10.1126/science.1201425.

Kivelson, M. G, K. K. Khurana, F. V. Coroniti, S. Joy, C. T. Russell, R. J. Walker, J. Warnecke, L. Bennett and C. Polanskey (1997), The magnetic field and magnetosphere of Ganymede, *Geophysical Research Letters*, *24*(17), 1944–8007, doi:10.1029/97GL02201.

Kivelson, M. G., Khurana, K. K., Stevenson, D. J., Bennett, L., Joy, S., Russel, C. T., Walker, R. J., Zimmer, C. and Polanskey, C. (1999), Europa and Callisto: Induced or intrinsic fields in a periodically varying plasma environment, *Journal of Geophysical Research*, *104*(A3), 4609–4625, doi:10.1029/1998JA900095.

Kivelson, M. G., F. Bagenal, W. S. Kurth, F. M. Neubauer, C. Paranicas and J. Saur (2004), Magnetospheric Interactions with Satellites in *Jupiter: The Planet, Satellites and Magnetosphere*, edited by F. Bagenal, T. E. Dowling and W. B. McKinnon, pp. 457–484, Cambridge University Press, Cambridge.

133

Kliore, A. J., A. Anabtawi, R. G. Herrera, S. W. Asmar, A. F. Nagy, D. P. Hinson and F. M. Flasar (2002), Ionosphere of Callisto from Galileo radio occultation observations, *Journal of Geophysical Research: Space Physics*, *107*(A11), SIA 19-1–SIA 19-7, doi:10.1029/2002JA009365.

Kuskov, O. L. and V. A. Kronrod (2005), Internal structure of Europa and Callisto, *Icarus*, *177*, 550–569, doi:10.1016/j.icarus.2005.04.014.

Liang, M. C., B. F. Lane, R. T. Pappalardo, M. Allen and Y. L. Yung (2005), Atmosphere of Callisto, *Journal of Geophysical Research: Planets*, *110*(E2), 1–9, doi:10.1029/2004JE002322.

Lindkvist, J., M. Holmström, K. K. Khurana, S. Fatemi and S. Barabash (2015), Callisto plasma interactions: Hybrid modeling including induction by a subsurface ocean, *Journal of Geophysical Research: Space Physics*, *120*(6), 4877–4889, doi:10.1002/2015JA021212.

Liuzzo, L., M. Feyerabend, S. Simon and U. Motschmanmn (2015), The impact of Callisto's atmosphere on its plasma interaction with the Jovian magnetosphere, *Journal of Geophysical Research: Space Physics*, *120*(11), 9401–9427, doi:10.1002/2015JA021792.

Liuzzo, L., S. Simon, M. Feyerabend, and U. Motschmann (2016), Disentangling plasma interaction and induction signatures at Callisto: The Galileo C10 flyby, *Journal of Geophysical Research: Space Physics*, *121*, 8677–8694, doi:10.1002/2016JA023236.

Makarov, O. P., J. M. Ajello, P. Vattipalle, I. Kanik, M. C. Festou and A. Bhardwaj (2004), Kinetic energy distributions and line profile measurements of dissociation products of water upon electron impact, *Journal of Geophysical Research: Space Physics*, *109*(A9), 1–15, doi:10.1029/2002JA009353.

McGrath, M. A., E. Lellouch, D. F. Strobel, P. D. Feldmann, R. E. Johnson (2004), Satellites Atmospheres, in *Jupiter: The planet, satellites and magnetosphere*, edited by F. Bagenal, T. E. Dowling and W. B. McKinnon, pp. 457–484, Cambridge University Press, Cambridge.

Milillo, A., C. Plainaki, E. De Angelis, V. Mangano, S. Massetti, A. Mura, S. Orsini, and R. Rispoli (2016), Analytical model of Europa's O2 exosphere, *Planetary and Space Science*, *130*, 3–13, doi:10.1016/j.pss.2015.10.011.

Moore, J. M., E. Asphaug, D. Morrison, J. R. Spencer, C. R. Chapman, B. Bierhaus, R. J. Sullivan, F. C. Chuang, J. E. Klemaszewski, R. Greeley, K. C. Bender, P. E. Geissler, P. Helfenstein, C. B. Pilcher (1999), Mass Movement and Landform Degradation on the Icy Galilean Satellites: Results of the Galileo Nominal Mission, *Icarus*, *140*(2), 294–312,doi: 10.1006/icar.1999.6132.

Murphy, D. M. and T. Koop (2005), Review of the vapour pressures of ice and supercooled water for atmospheric applications, *Quarterly Journal of the Royal Meteorological Society*, *131*(608), 1539–1565, doi:10.1256/qj.04.94.

Nagy, A. F. and P. M. Banks (1970), Photoelectron fluxes in the ionosphere, *Journal of Geophysical Research: Space Physics*, *75*(31), 6260–6270, doi:10.1029/JA075i031p06260.

Neubauer, F. M. (1998), The sub-Alfénic interaction of the Galilean satellites with the Jovian magnetosphere, *Journal of Geophysical Research*, *103*(E9), 19,843–19,866, doi:10.1029/97JE03370.

Neubauer, F. M. (1999), Alfvén wings and electromagnetic induction in the interiors: Europa and Callisto, *Journal of Geophysical Research* 104(A12), 28671–28684, doi:10.1029/1999JA900217.

Nir, S., S. Adams and R. Rein (1973), Polarizability calculations on water, hydrogen, oxygen, and carbon dioxide, *The Journal of Chemical Physics*, *59*(6), 3341–3355, doi:10.1063/1.1680478.

Opal, C. B., W. K. Peterson and E. C. Beaty (1971), Measurements of Secondary-Electron Spectra Produced by Electron Impact Ionization of a Number of Simple Gases, *Journal of Chemical Physics*, *55*(8), 4100–4106, doi:10.1063/1.1676707.

Peverall, R., S. Rosén, J. R. Peterson, M. Larsson, A. Al-Khalili, L. Vikor, J. Semaniak, R. Bobbenkamp, A. Le Padellec, A. N. Maurellis and W. J. van der Zande (2001), Dissociative recombination and excitation of $O2^+$: Cross sections,

product yields and implications for studies of ionospheric airglows. *Journal of Chemical Physics*, *114*(15), 6679–6689, doi:10.1063/1.1349079.

Plainaki, C., A. Milillo, A. Mura, S. Orsini, S. Massetti and T. Cassidy (2012), The role of sputtering and radiolysis in the generation of Europa's exosphere, *Icarus*, *218*(2), 956–966, doi:10.1016/j.icarus.2012.01.023.

Plainaki, C., A. Milillo, A. Mura, J. Saur, S. Orsini and S. Massetti (2013), Exospheric O_2 densities at Europa during different orbital phases, *Planetary and Space Science*, *88*, 42–45, doi:10.1016/j.pss.2013.08.011.

Rakshit, A. B. and P. Warneck (1980), Reactions of CO_2^+, $CO_2CO_2^+$ and H_2O^+ ions with various neutral molecules, *Journal of the Chemical Society, Faraday Transactions 2: Molecular and Chemical Physics*, *76*, 1084–1092, doi:10.1039/F29807601084.

Rees, M. H. (1989), *Physics and chemistry of the upper atmosphere*, Cambridge University Press, Cambridge.

Retherford, K. D., H. W. Moos, D. F. Strobel, B. C. Wolven and F. L. Roesler (2000), Io's equatorial spots: Morphology of neutral UV emissions, *Journal of Geophysical Research: Space Physics*, *105*(A12), 27157–27165, doi:10.1029/2000JA002500.

Richards, P. G., J. A. Fennelly and D. G. Torr (1994), EUVAC: A solar EUV Flux Model for aeronomic calculations, *Journal of Geophysical Research: Space Physics*, *99*(A5), 8981–8992, doi:10.1029/94JA00518.

Rosén, S., A. Derkatch, J. Semaniak, A. Neau, A. Al-Khalili, A. Le Padellec, L. Viktor, R. Thomas, H. Danared, M. af Ugglas and M. Larsson (2000), Recombination of simple molecular ions studied in storage ring: dissociative recombination of H_2O^+, *Faraday discussions*, *115*, 295–302, doi:10.1039/A909314A.

Roth, L., J. Saur, D. F. Strobel, P. D. Feldman, M. A. McGrath and F. Nimmo (2014), Transient Water Vapor at Europa's South Pole, *Science*, *343*(6167), 171–175, doi:10.1126/science.1247051.

Roth, L., J. Saur, K. D. Retherford, A. Blöcker, D. F. Strobel, and P. D. Feldman (2017), Constraints on Io's interior from auroral spot oscillations, *Journal of Geophysical Research: Space Physics*, *122*, doi:10.1002/2016JA023701.

Ruiz, J. (2001), The stability against freezing of an internal liquid-water ocean in Callisto, *Nature*, *412*, 409–411, doi:10.1038/35086506.

Saur, J., D. F. Strobel and F. M. Neubauer (1998), Interaction of the Jovian magnetosphere with Europa: Constraints on the neutral atmosphere, *Journal of Geophysical Research: Planets*, *103*(E9), 19947–19967, doi:10.1029/97JE03556.

Saur, J., F. M. Neubauer, D. F Strobel and M. E. Summers (1999), Three-dimensional plasma simulation of Io's interaction with the Io plasma torus: Asymmetric plasma flow, *Journal of Geophysical Research*, *104*(A11), 25105–25126, doi:10.1029/1999JA900304.

Saur, J., F. M. Neubauer, D. F. Strobel and M. E. Summers (2000), Io's ultraviolet aurora: Remote sensing of Io's interaction, *Geophysical Research Letters*, *27*(18), 2893–2896, doi:10.1029/2000GL003824.

Saur, J., F. M. Neubauer, D. F. Strobel and M. E. Summers (2002), Interpretation of Galileo's Io plasma and field observations: I0, I24, and I27 flybys and close polar passes, *Journal of Geophysical Research: Space Physics*, *107*(A12), SMP 5-1–SMP 5-18, doi:10.1029/2001JA005067.

Saur, J. (2004), A model of Io's local electric field for a combined Alfvénic and unipolar inductor far-field coupling, *Journal of Geophysical Research*, *109*, A01210, doi:10.1029/2002JA009354.

Saur, J., F. M. Neubauer, J. E. P Connerney, P. Zarka and M. G. Kivelson (2004), Plasma Interaction of Io with its Plasma Torus in *Jupiter: The Planet, Satellites and Magnetosphere*, edited by F. Bagenal, T. E. Dowling and W. B. McKinnon, pp. 457–484, Cambridge University Press, Cambridge.

Saur, J., S. Duling, L. Roth, X. Jia, D. F. Strobel, P. D. Feldman, Ulrich R. Christensen, K. D. Retherford, M. A. McGrath, F. Musacchio, A. Wennmacher, F. M. Neubauer, S. Simon and O. Hartkorn (2015), The search for a subsurface ocean in Ganymede with Hubble Space Telescope observations of its auroral

ovals, *Journal of Geophysical Research: Space Physics*, *120*(3), 1715–1737, doi:10.1002/2014JA020778.

Schilling, N., F. M Neubauer and J. Saur (2007), Time-varying interaction of Europa with the Jovian magnetosphere: Constraints on the conductivity of Europa's subsurface ocean, *Icarus*, *192*, 41–55, doi:10.1016/j.icarus.2007.06.024.

Schunk, R. W. and A. F. Nagy (1978), Electron temperatures in the F region of the ionosphere: Theory and observations, *Reviews of Geophysics*, *16*(3), 355–399.

Schunk, R. and A. F. Nagy (2009) *Ionospheres: Physics, Plasma Physics, and Chemistry*, Cambridge University Press, Cambridge.

Seufert, M., J. Saur and F. M. Neubauer (2011), Multi-frequency electromagnetic sounding of the Galilean moons, *Icarus*, *214*, 477–494, doi:10.1016/j.icarus.2011.03.017.

Seufert, M. (2012), *Callisto: Induction Signals, Atmosphere and Plasma Interaction*, dissertation, University of Cologne.

Sheehan, C. H. and J.-P. St Maurice (2004), Dissociative recombination of N2+, O2+, and NO+: Rate coefficients for ground state and vibrationally excited ions, *Journal of Geophysical Research: Space Physics*, *109*(A3), A03302, doi:10.1029/2003JA010132.

Simon, S., H. Kriegel, J. Saur, A. Wennmacher, F. M. Neubauer, E. Roussos, U. Motschmann and M. K. Dougherty (2012), Analysis of Cassini magnetic field observations over the poles of Rhea, *Journal of Geophysical Research* 117, A07211, doi:10.1029/2012JA017747.

Stamnes, K. and M. H. Rees (1983), Inelastic Scattering Effects on Photoelectron Spectra and Ionospheric Electron Temperature, *Journal of Geophysical Research*, *88*(A8), 6301–6309, doi:10.1029/JA088iA08p06301.

Strickland, D. J., D. L. Book, T. P. Coffey, and J. A. Fedder (1976), Transport Equation Techniques for the Deposition of Auroral Electrons, *Journal of Geophysical Research*, *81*(16), 2755–2764, doi:10.1029/JA081i016p02755.

Strickland, D. J., J. Bishop, J. S. Evans, T. Majeed, P. M. Shen, R. J. Cox, R. Link and R. E. Huffman (1999), Atmospheric Ultraviolet Radiance Integrated Code (AURIC): theory, software architecture, inputs, and selected results, *Journal of Quantitative Spectroscopy and Radiative Transfer*, *62*(6), 689–742, doi:10.1016/S0022-4073(98)00098-3.

Strobel, D. F., J. Saur, P. D. Feldman and M. A. McGrath (2002), Hubble Space Telescope space telescope imaging spectrograph search for an atmosphere on Callisto: A Jovian unipolar inductor, *Astrophysical Journal*, *581*(1), L51–L54, doi:10.1086/345803.

Swartz, W. E., J. S. Nisbet and A. E. S. Green (1971), Analytic expression for the energy-transfer rate from photoelectrons to thermal-electrons, *Journal of Geophysical Research*, *76*(34), 8425–8426, doi:10.1029/JA076i034p08425.

Swartz, W. E. (1985), Optimization of Energetic Electron Energy Degradation Calculations, *Journal of Geophysical Research*, *90*(A7), 6587–6593, doi:10.1029/JA090iA07p06587.

Takayanagi, K. and Y. Itikawa (1970), The Rotational Excitation of Molecules by Slow Electrons, *Advances in Atomic and Molecular Physics*, *6*, 105–153, doi:10.1016/S0065-2199(08)60204-3

Vorburger, A., P. Wurz, H. Lammer, S. Barabash and O. Mousis (2015), Monte-Carlo simulations of Callisto's exosphere, *Icarus*, *262*, 14–29, doi:10.1016/j.icarus.2015.07.035.

Wedlund, C. S., G. Gronoff, J. Lilensten, H. Ménager and M. Barthélemy (2011), Comprehensive calculation of the energy per ion pair or W values for five major planetary upper atmospheres, *Annales Geophysicae*, *29*(1), 187–195, doi:10.5194/angeo-29-187-2011.

White, O. L., O. M. Umurhan, J. M. Moore, and A. D. Howard (2016), Modeling of ice pinnacle formation on Callisto, *Journal of Geophysical Research: Planets*, *121*, 21–45, doi:10.1002/2015JE004846.

Yung, Y. L. and M. B. McElroy (1977), Stability of an Oxygen Atmosphere on Ganymede, *Icarus*, *30*(1), 97–103, doi:10.1016/0019-1035(77)90124-5.

Zienkiewicz, 0. C., C. Emson and P. Bettess (1983), A novel boundary infinite element, *International Journal for Numerical Methods in Engineering*, *19*, 393–404, doi:10.1002/nme.1620190307.

Zimmer, C., K. K. Khurana and M. G. Kivelson (2000), Subsurface Oceans on Europa and Callisto: Constraints from Galileo Magnetometer Observations, *Icarus*, *147*, 329–347, doi:10.1006/icar.2000.6456.

Acknowledgement

Versicherung

Ich versichere, dass ich die von mir vorgelegte Dissertation selbständig angefertigt, die benutzten Quellen und Hilfsmittel vollständig angegeben und die Stellen der Arbeit - einschließlich Tabellen, Karten und Abbildungen -, die anderen Werken im Wortlaut oder dem Sinn nach entnommen sind, in jedem Einzelfall als Entlehnung kenntlich gemacht habe; dass diese Dissertation noch keiner anderen Fakultät oder Universität zur Prüfung vorgelegen hat; dass sie - abgesehen von unten angegebenen Teilpublikationen - noch nicht veröffentlicht worden ist, sowie, dass ich eine solche Veröffentlichung vor Abschluss des Promotionsverfahrens nicht vornehmen werde. Die Bestimmungen der Promotionsordnung sind mir bekannt. Die von mir vorgelegte Dissertation ist von Prof. Dr. Joachim Saur betreut worden.

Köln, 11. Juli 2017

Oliver Hartkorn

Teilpublikationen

Hartkorn, O., J. Saur, and D. F. Strobel (2017), Structure and density of Callisto's atmosphere from a fluid-kinetic model of its ionosphere: Comparison with Hubble Space Telescope and Galileo observations, *Icarus*, *282*, 237–259, doi:10.1016/j.icarus.2016.09.020.

Hartkorn, O. and J. Saur (2017), Induction signals from Callisto's ionosphere and their implications on a possible subsurface ocean, *Submitted to Journal of Geophysical Research: Space Physics in April 2017*.

Curriculum Vitae

Persönliche Daten

Name	Oliver Andreas Hartkorn
Geburtsdatum	19.11.1987
Geburtsort	Dernbach
Nationalität	deutsch

Schulbildung und Studienverlauf

2014 - 2017	Promotion Geophysik, Arbeitsgruppe Weltraumgeophysik
	Universität zu Köln
2008 - 2013	Studium Physik, Abschluss: Diplom-Physiker
	Johannes Gutenberg-Universität Mainz
1998 - 2007	Schulbildung, Abschluss: Allgemeine Hochschulreife
	Marion Dönhoff Gymnasium Lahnstein

Arbeitserfahrung

2014 - 2017	Wissenschaftlicher Mitarbeiter
	Universität zu Köln